

~~DTIC FILE COPY~~

2

DTIC FILE COPY

AFGL-TR-88-0151

**ESTIMATES OF SEISMIC DETECTION CAPABILITY
IN THE SOVIET UNION BASED ON NORESS OBSERVATIONS**

AD-A203 620

Thomas J. Sereno, Jr.
Steven R. Bratt

Science Applications International Corp.
10260 Campus Point Drive
San Diego, CA 92121

1 July 1988

Final Report
1 February 1986 - 31 January 1988

DTIC
ELECTE
OCT 28 1988
S D
RE

~~Distribution~~ Distribution ~~is limited to~~ U.S. Government agencies and their contractors.
Administrative/Operational Use: 28 July 1988. Other requests for
this document shall be referred to AFGL/IWR, Hanscom AFB, MA 01911-5000.

**AIR FORCE GEOPHYSICS LABORATORY
AIR FORCE SYSTEMS COMMAND
UNITED STATES AIR FORCE
HANSCOM AIR FORCE BASE, MASSACHUSETTS 01731-5000**

This document has been approved
for public release and may be
distributed unlimitedly.

WARNING - This document contains technical data whose
export is restricted by the Arms Export Control Act (Title
28, U.S.C. Sec. 1751 et seq.) or The Export Administration
Act of 1979, as amended (Title 50, U.S.C. App. 2401 et seq.).
Violations of these export laws are subject to severe criminal
penalties. Disseminate in accordance with the provisions of
AFR 80-17.

88 1028 006

DESTRUCTION NOTICE: For classified documents, follow the procedures
in DoD 5200.22-N, Industrial Security Manual, Section II-19 or
DoD 5200.1-R, Information Security Program Regulation, Chapter IX.
For unclassified, limited documents, destroy by any method that
will prevent disclosure of contents or reconstruction of the document.

Sponsored by: Defense Advanced Research Projects Agency
Nuclear Monitoring Research Office
DARPA Order No. 5307

Monitored by: Air Force Geophysics Laboratory

Contract No. F19628-86-C-0051

The views and conclusions contained in this document are those of the authors and should not be interpreted as representing the official policies, either expressed or implied, of the Defense Advanced Research Projects Agency or the U.S. Government.

"This technical report has been reviewed and is approved for publication"


JAMES F. LEWNOWICZ
Contract Manager


HENRY A. OSSING
Branch Chief

FOR THE COMMANDER


DONALD H. ECKHARDT
Division Director

Qualified requestors may obtain additional copies from the Defense Technical Information Center.

If your address has changed, or if you wish to be removed from the mailing list, or if the addressee is no longer employed by your organization, please notify AFGL/DAA, Hanscom AFB, MA 01731. This will assist us in maintaining a current mailing list.

Do not return copies of this report unless contractual obligations or notices on a specific document requires that it be returned.



DEPARTMENT OF THE AIR FORCE
AIR FORCE GEOPHYSICS LABORATORY (AFGL)
HANSCOM AIR FORCE BASE, MASSACHUSETTS 01731-5000

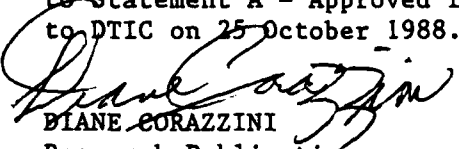
REPLY TO: AFGL/SULLP (Diane Corazzini, 4553)
ATTN OF:

20 December 1988

SUBJECT: AFGL-TR-88-0151 - Estimates of Seismic Detection Capability in the Soviet Union Based on Noress Observations

TO: Defense Technical Information Center
Attn: Madeline Crumbacker
Cameron Station
Alexandria, VA 22304

Attached is letter dated 20 December 1988 approving subject report for downgrading to Statement A - Approved for public release; distribution unlimited. Report sent to DTIC on 25 October 1988.


DIANE CORAZZINI
Research Publications

1 Atch
Ltr dtd 20 Dec 1988

cc: AFGL/SULL
AFGL/LWH



DEPARTMENT OF THE AIR FORCE
HEADQUARTERS ELECTRONIC SYSTEMS DIVISION (AFSC)
HANSCOM AIR FORCE BASE, MASSACHUSETTS 01731-5000

REPLY TO
ATTN OF:

ESD/PAM (4065)

20 December 1988

SUBJECT:

AFGL-TR-88-0151

TO:

AFGL/SULLP (Diane Corazzini)

ESD/PAM has no objection to release of the above-referenced Technical Report, "Estimates of Seismic Detection Capability in the Soviet Union Based on Noress Observations" to the National Technical Information Service.

A handwritten signature in cursive script, reading "Kevin F. Gilmartin", is positioned above the typed name.

KEVIN F. GILMARTIN
Chief, Media Relations
Directorate of Public Affairs
and Communication Services

UNCLASSIFIED

SECURITY CLASSIFICATION OF THIS PAGE

~~SECRET~~

REPORT DOCUMENTATION PAGE

1a. REPORT SECURITY CLASSIFICATION Unclassified			1b. RESTRICTIVE MARKINGS <div style="border: 1px solid black; padding: 5px; display: inline-block;">This document has been approved for public release and sale in distribution is unlimited.</div>			
3a. SECURITY CLASSIFICATION AUTHORITY			AFGL-TR-88-0151			
2b. DECLASSIFICATION / DOWNGRADING SCHEDULE						
4. PERFORMING ORGANIZATION REPORT NUMBER(S) SAIC-88/1753			7a. NAME OF MONITORING ORGANIZATION Air Force Geophysics Laboratory (LWH)			
6a. NAME OF PERFORMING ORGANIZATION Science Applications International Corporation		6b. OFFICE SYMBOL (if applicable)	7b. ADDRESS (City, State, and ZIP Code) Hanscom Air Force Base, MA 01731-5000			
6c. ADDRESS (City, State, and ZIP Code) 10260 Campus Point Drive San Diego, CA 92121			9. PROCUREMENT INSTRUMENT IDENTIFICATION NUMBER F-19628- 86-C-0051			
8a. NAME OF FUNDING / SPONSORING ORGANIZATION DARPA		8b. OFFICE SYMBOL (if applicable) GSD	10. SOURCE OF FUNDING NUMBERS			
8c. ADDRESS (City, State, and ZIP Code) 1400 Wilson Blvd. Arlington, VA 22209			PROGRAM ELEMENT NO. 62714E	PROJECT NO. 6A10	TASK NO. DA	WORK UNIT ACCESSION NO. BB
11. TITLE (Include Security Classification) Estimates of Seismic Detection Capability in the Soviet Union Based on NORESS Observations						
12. PERSONAL AUTHOR(S) Thomas J. Sereno, Jr., and Steven R. Bratt						
13a. TYPE OF REPORT Final Technical		13b. TIME COVERED FROM 2/1/86 TO 1/31/88		14. DATE OF REPORT (Year, Month, Day) 1988 July 1		15. PAGE COUNT 80
16. SUPPLEMENTARY NOTATION						
17. COSATI CODES			18. SUBJECT TERMS (Continue on reverse if necessary and identify by block number)			
FIELD	GROUP	SUB-GROUP	Regional Seismology, Attenuation, Seismic Moment, Detection Capability, NORESS, Inversion, Soviet Union			
19. ABSTRACT (Continue on reverse if necessary, and identify by block number)			<p>→ The detection capability of the NORESS^{SEISMIC} array is estimated, and the results are used to estimate the detection threshold of a network including NORESS-type stations in the Soviet Union. First, the frequency-dependent attenuation of P_n and L_g at NORESS is estimated by inverting single-channel spectra from 186 events at ranges between 200-1400 km with magnitudes between 1.1 and 4.8. The P_n spectra are inverted between 1-15 Hz and the L_g spectra between 1-7 Hz for both seismic moment and apparent attenuation. The result is a simple parameterization of the source and range dependence of regional P_n and L_g spectra. However, signal detection at NORESS is determined from time domain filtered beams, so a parameterization of single-channel spectra is not sufficient to determine detection capability. Therefore, we determine the relationship between the spectral amplitudes used in the inversion and the time</p>			
20. DISTRIBUTION / AVAILABILITY OF ABSTRACT <input type="checkbox"/> UNCLASSIFIED/UNLIMITED <input checked="" type="checkbox"/> SAME AS RPT. <input type="checkbox"/> DTIC USERS			21. ABSTRACT SECURITY CLASSIFICATION UNCLASSIFIED			
22a. NAME OF RESPONSIBLE INDIVIDUAL James F. Lewkowicz			22b. TELEPHONE (Include Area Code) (617) 377-3028		22c. OFFICE SYMBOL AFGL/LWH	

DD FORM 1473, 84 MAR

83 APR edition may be used until exhausted.
All other editions are obsolete.

SECURITY CLASSIFICATION OF THIS PAGE

UNCLASSIFIED

UNCLASSIFIED

(201)

domain amplitudes used in signal detection. We find that the temporal signal-to-noise ratio (SNR) for P_n on a filtered beam can be expressed as a product of the single-channel spectral SNR and terms specific to the NORESS array configuration and beamforming. This factorization allows us to determine NORESS detection capability from our spectral parameterization, and to predict the P_n detection capability for other regions and other station configurations. A comparable relationship cannot be determined for L_g due to dispersion and the non-stationarity of the pre- L_g noise. Instead, we simply determine an empirical relationship for L_g detectability based on observed temporal amplitudes, noting that the results cannot be easily extrapolated to other areas with different attenuation. To demonstrate the validity of our results for NORESS, we compare predictions based on our model to observed detection statistics and to results obtained by Ringdal [1986] who compared detections at NORESS to bulletins produced by local seismic networks. Finally, we use the NORESS results to normalize simulations of the detection capability of a network of NORESS-type arrays; 13 external to the Soviet Union and 20 internal. If the frequency-dependent attenuation and noise in the USSR are like those observed at NORESS, we estimate the 90% M_L threshold for detecting 3 P_n phases for events in the Soviet Union to be between 2.4 and 2.7. For 3 P_n or L_g detections the threshold is reduced by about 0.2 to 0.3. If Q_{P_n} is 50% greater throughout the Soviet Union than estimated for Scandinavia, the 90% M_L threshold is between 2.3 and 2.6. If Q_{P_n} is 50% lower than estimated for Scandinavia, the threshold is between 2.7 and 2.9. These simulations are carefully normalized by the actual detection capability of a prototype for stations that might be installed. However, estimates of attenuation and noise inside the Soviet Union are needed to determine how they actually differ from those at NORESS. Also, the NORESS detection capability estimates (and therefore the simulations) are for average conditions, and there are regular variations that must be taken into account when estimating treaty monitoring capability.

(e die)
A

34

Accession For	
NTIS GRA&I	<input checked="" type="checkbox"/>
DTIC TAB	<input type="checkbox"/>
Unannounced	<input type="checkbox"/>
Justification	
By	
Distribution/	
Availability Codes	
Dist	Avail and/or Special
A-1	

NOV 1986

DDIC
DDPV
INSPECTED
6

ii

UNCLASSIFIED

Table of Contents

1. SUMMARY	1
1.1 Objectives	1
1.2 Reports	1
1.3 Summary of "Estimates of Seismic Detection Capability in the Soviet Union Based on NORESS Observations"	3
<i>1.3.1 Introduction</i>	3
<i>1.3.2 Approach</i>	3
<i>1.3.3 Results</i>	4
<i>1.3.4 Outline of report</i>	8
2. SPECTRAL INVERSION	10
2.1 Method	10
2.2 Data	12
2.3 Results	15
<i>2.3.1 Seismic moment and Q</i>	15
<i>2.3.2 Simulation of NORESS spectra</i>	19
3. TEMPORAL AMPLITUDES AND DETECTABILITY	21
3.1 Detection statistics	21
3.2 Relationship between spectral and temporal amplitudes	25
<i>3.2.1 Noise</i>	25
<i>3.2.2 Signal</i>	29
<i>3.2.3 Signal-to-Noise</i>	31
3.3 Regional wave detectability	33
<i>3.3.1 Pn detectability</i>	34
<i>3.3.2 Lg detectability</i>	37
3.4 Detection capability of the NORESS array	37
4. DETECTION CAPABILITY SIMULATION	41
4.1 Extrapolation of NORESS capability	41
4.2 Detection Capability in the Soviet Union	48
5. CONCLUSIONS	58
ACKNOWLEDGEMENTS	62
REFERENCES	63

1. SUMMARY

1.1 Objectives

This two-year project was directed toward three major objectives:

- An assessment of the event detection and identification capabilities of the NORESS array.
- An estimate of the degree to which these capabilities depend on the specific characteristics of this site.
- An evaluation of the CTBT monitoring capabilities using networks including stations like RSTN and NORESS.

The first two objectives were addressed in the semi-annual technical reports of this contract (reports 1, 3, and 5 in the following section). This final report summarizes these previous results, and presents extensive new work toward the third objective.

1.2 Reports

The following reports and papers were completed under support by this contract:

1. Suteau-Henson, A. and T. Bache, Spectra of regional phases at NORESS, *Semi-Annu. Tech. Rep. SAIC 86/1967*, Sci. Appl. Int. Corp., San Diego, Calif., 1986.

This is the first semi-annual report of this contract. The key issues addressed are the signal characteristics of *Pn* and *Lg* phases recorded at NORESS (in particular, the repeatability of spectra from blasts in specific mines), an estimate of the average ambient noise spectrum at NORESS, and an assessment of event identification capability using the ratio of high and low frequency signal energy.

2. Suteau-Henson, A., T. Sereno, and T. Bache, Spectral characteristics and attenuation of regional phases recorded at NORESS, *Proceedings of the DARPA/AFGL Seismic Research Symposium, Nantucket, MA, 185-190, 15-18 June 1987.*

This short paper reviews the results of two studies. In one *Pn* spectra are compared for various events to evaluate their potential for event characterization. The second study presents preliminary results from an inversion of NORESS spectra for *Q* and seismic moment.

3. Sereno, T., S. Bratt, and T. Bache, Regional wave attenuation and seismic moment from the inversion of NORESS spectra, *Semi-Annu. Tech. Rep. SAIC 87/1736*, Sci. Appl. Int. Corp., San Diego, Calif., *AFGL-TR-87-0237*, ADA187399, 1987.

This is a comprehensive investigation of the attenuation of P_n and L_g spectra recorded at NORESS. A method is presented for inverting spectra for both seismic moment and apparent attenuation. The method is applied to spectra from 190 regional events recorded at NORESS. The result is an accurate parameterization of the distance and magnitude dependence of these spectra. This report is the second semi-annual technical report of this contract.

4. Sereno, T., S. Bratt, and T. Bache, Simultaneous inversion of regional wave spectra for attenuation and seismic moment in Scandinavia, *J. Geophys. Res.*, 93, 2019-2035, 1988.

This paper parallels our second semi-annual technical report (report 3 above) with the exception that the L_g spectra are computed for a fixed group velocity window rather than for a fixed time length. Our results for NORESS are compared to attenuation estimates used by *Evernden et al.* [1986] to simulate detection capability in the Soviet Union.

5. Sereno, T., and S. Bratt, Attenuation and detection capability of regional phases recorded at NORESS, *Semi-Annu. Tech. Rep. SAIC 88/1598*, Sci. Appl. Int. Corp., San Diego, Calif., *AFGL-TR-88-0095*, 1988.

The main objective of this report is to determine the relationship between the spectral amplitudes used in our attenuation study and the temporal amplitudes used in signal detection. This relationship is used to express the detection capability at NORESS in terms of the spectral inversion parameters (e.g., Q and moment) and to determine the sensitivity of our results to the specific characteristics of this site. We compare our model to observed detection statistics and to the results of previous investigations. This is the third semi-annual technical report of this contract.

6. Suteau-Henson, A. and T. Bache, Spectral characteristics of regional phases recorded at NORESS, *Bull. Seism. Soc. Am.*, 78, 708-725, 1988.

This paper parallels the first semi-annual report of this contract (report 1 above).

7. Sereno, T., S. Bratt, and T. Bache, Regional wave detection capability at NORESS, *Proceedings of the DARPA/AFGL Seismic Research Symposium, Fallbrook, CA, 61-66, 3-5 May 1988.*

This short paper is a summary of many of the results presented in this final report.

1.3 Summary of "Estimates of Seismic Detection Capability in the Soviet Union Based on NORESS Observations"

1.3.1 Introduction

In this report we examine the detection capability of the NORESS array and its implications for estimating the detection threshold of a network of seismic stations in and around the Soviet Union. NORESS was designed as a prototype array for regional monitoring, and it is located within regional distance to portions of the western USSR. Therefore, the NORESS detection capability provides a reasonable basis for normalizing simulations of the detection capability of hypothetical networks in the vicinity of the Soviet Union. However, NORESS may not represent the actual attenuation and noise for the stations in our hypothetical network, so we also determine the sensitivity of the results to changes in the frequency-dependent signal and noise characteristics. The primary issues involved in seismic monitoring are detection, location, and event identification, and these are discussed below.

- *Detection Capability.* The primary focus of this report is on the detection capability of hypothetical networks in the Soviet Union.
- *Location.* Signal detection is only meaningful if there is adequate information to locate the source. Therefore, our simulations of detection capability require detection of at least three phases (arrival times and azimuths) by the hypothetical network (constraining latitude, longitude, and depth). *Bratt et al.* [1987] show that for a network including 20 NORESS-type arrays internal to the Soviet Union and 13 external, the 3-phase location uncertainty for events near the detection threshold is about 10-15 km. This uncertainty can be reduced with more accurate travel-time tables and/or master-event location techniques, as discussed in that report. Also, *Bratt et al.* [1987] analyzed the sensitivity of the location uncertainty to network configuration. We present no further work on these issues here.
- *Event Identification.* Numerous techniques have been proposed to discriminate between explosions and earthquakes at regional distances [for review, see *Pomeroy et al.*, 1982]. It appears that regional event identification requires the ability to distinguish relatively subtle source effects within a cloud of complex propagation effects. For this reason, it is important to accurately calibrate propagation effects for specific regions of interest.

In this report we concentrate on detection capability because it is the most fundamental aspect of monitoring capability. Lowering the detection threshold gives roughly proportional improvements to the location and identification capabilities.

1.3.2 Approach

Our approach to estimating the detection capability of a hypothetical network in the Soviet Union involves the following steps:

1. We determine an accurate parameterization of regional Pn and Lg spectra recorded at NORESS in terms of event magnitude and apparent attenuation. This is done by inverting spectra from 186 regional events for seismic moment and apparent attenuation. With this parameterization, we can predict the spectra for a chosen source and range and be confident that our results are correct within the well-defined uncertainty of our parameters.
2. We determine the relationship between the spectral amplitudes and the temporal amplitudes used in signal detection. This allows us to use our spectral parameterization to estimate (temporal) detection capability.
3. We estimate NORESS detection capability with the spectral parameterization. Since this detection capability is a function of the attenuation observed at NORESS and other terms specific to the NORESS array configuration and processing, we can estimate the extent to which our results depend on characteristics specific to NORESS. Our NORESS detection capability model is validated with observed detection statistics.
4. We simulate the detection capability of a hypothetical network of NORESS-capability arrays in the Soviet Union. Of course, this assumes that NORESS capability represents the signal and noise environment in the Soviet Union. Therefore, we estimate the sensitivity of these simulations to changes in the assumptions about the attenuation and noise in the Soviet Union.

1.3.3 Results

We have determined a simple and accurate parameterization of the magnitude and distance dependence of regional Pn and Lg spectra recorded at NORESS. This parameterization is based on the inversion of spectra from 186 events with magnitudes between 1.1 and 4.8 and epicentral distances between 200 and 1400 km. Figure 1.1 displays the predicted Pn and Lg spectra at 500, 800, and 1000 km for a magnitude 3.0 event, based on this parameterization. The bottom curve is the average ambient noise spectrum at NORESS [Sutau-Henson and Bache, 1988]. The predicted Pn spectrum is nearly parallel to the noise curve at a range of about 500 km, a result that is consistent with a NORSAR study that examined data from the high-frequency element of the NORESS array [Ringdal et al., 1986]. At longer ranges, the predicted frequency of the maximum signal-to-noise ratio is considerably less than 15 Hz. Evernden et al. [1986] propose that detection capability would be enhanced at high frequency (> 20 Hz). Our results for Scandinavia do not support this contention except at ranges less than about 400-500 km.

Figure 1.1 is an accurate representation of Lg spectra, but cannot be used to estimate signal-to-noise (the ambient noise curve is plotted with the Lg spectra in Figure 1.1b). The "noise" prior to the Lg arrival is actually the ambient noise plus P and Sn coda, and is a complicated function of range and source. However, we can note that the Lg spectrum reaches the ambient noise level at a much lower frequency than the Pn spectrum, while at long periods the

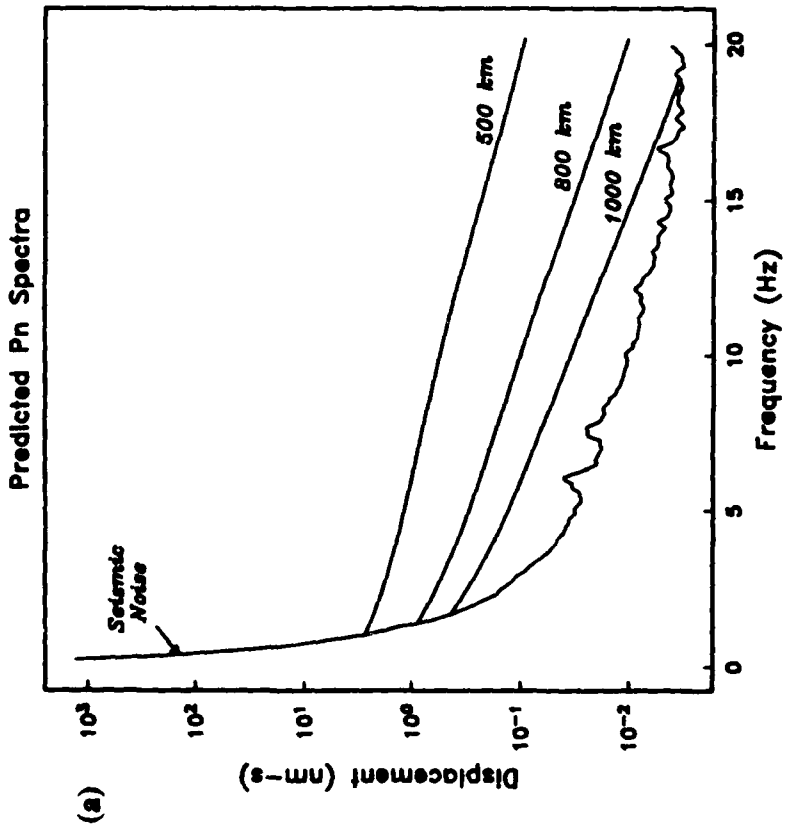
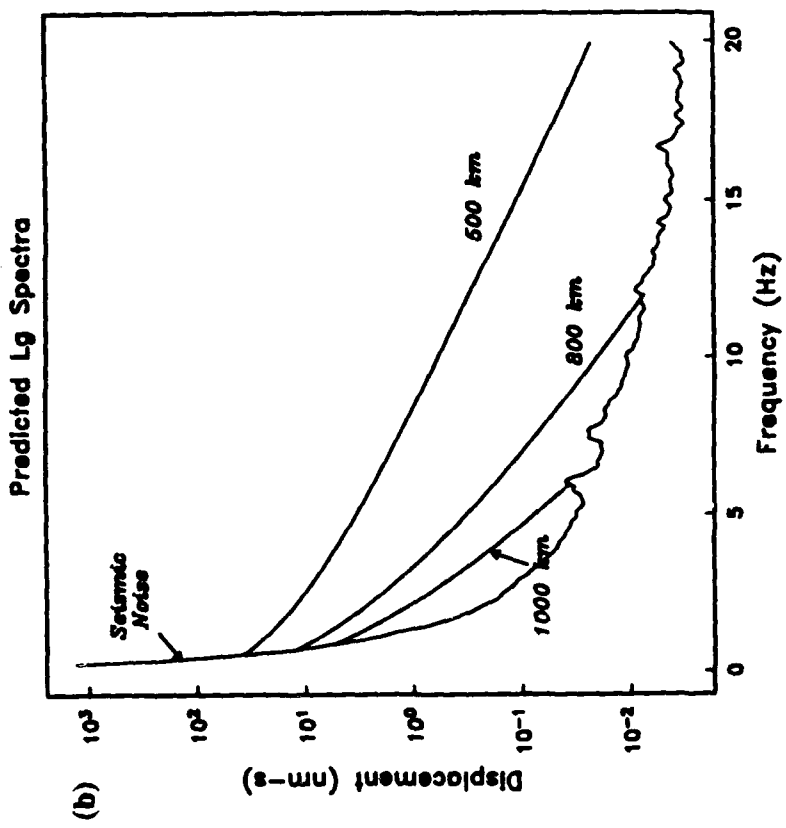


Figure 1.1. Predicted NORESS (a) P_n and (b) L_g displacement spectra at three epicentral distances for a magnitude 3.0 explosion, based on the inversion results. The average NORESS noise was estimated from 43 5-s samples taken prior to P_n [Sutau-Henson and Bache, 1988].

Lg amplitude exceeds that of Pn by as much as a factor of 10. This is consistent with the observation that regional seismograms are characterized by Lg being the largest-amplitude phase and Pn having a higher dominant frequency.

To estimate detection capability from these spectral results, it is necessary to determine the relationship between temporal and spectral amplitudes. Signal detection at NORESS is achieved when the short term average (STA) divided by the long term average (LTA) exceeds a predetermined threshold. These amplitudes are measured on filtered beams. Therefore, it is necessary to determine the relationship between single-channel spectral amplitudes and these time-domain amplitudes on filtered beams. For Pn we find that the temporal STA/LTA can be expressed as a product of the single channel spectral SNR (for which we have parameterization in terms of Q and magnitude) and terms specific to the array configuration and beamforming. This factorization allows us to determine the extent to which our NORESS Pn detection capability estimates depend upon the specific characteristics of this site.

The Lg spectrum depends on window length and the pre- Lg noise includes the coda of previously arriving phases. Therefore, a similar relationship can not be found for Lg . We simply note that the Lg spectral amplitudes computed for 5-s windows starting just prior to the detection time are proportional to the STA on the beam with the maximum SNR. However, Lg Q estimates based on fixed 5-s windows are not available for other regions, so our results for Lg are not easily extrapolated. The pre- Lg LTA is more complex. We parameterized it as a function of frequency, distance, beam type (coherent or incoherent), and magnitude, and the latter is most important. We find that the log LTA increases proportional to $0.8 M_L$. Since both Lg STA and LTA increase with M_L , the detectability of Lg is much less dependent on magnitude than the detectability of Pn .

We estimate NORESS detection capability using our spectral inversion results together with an empirical parameterization of the temporal SNR. The latter is called the "detectability," and it gives the probability of detection of a given magnitude event as a function of epicentral distance. The detectability is computed directly from detector parameters (e.g., the STA, LTA, and pre-set detector thresholds). For extrapolating these results to other areas (with estimates for the attenuation) we use our spectral inversion results and the relationship between temporal and spectral amplitudes. To validate this procedure, we compare "predicted" (based on our inversion results) and "observed" Pn detectability at NORESS. The dashed curves in Figure 1.2 plot our estimates of the 90% NORESS M_L thresholds for detecting Pn and for detecting Pn or Lg , based on the "detectability." The solid curve is the 90% M_L threshold for detecting Pn based on the inversion results. Also indicated in Figure 1.2 are the results of Ringdal [1986] who estimated the 90% M_L threshold for detecting P phases between 700 and 1400 km to be 2.7 and for detecting P or secondary phases in the same distance range to be 2.5. The average distance of the events used in that study is about 960 km. The three independent studies produce consistent estimates of the regional wave detection capability of the NORESS array, which lends considerable support to our spectral parameterization.

Our confidence in predictions of detection capability for other regions depends on how well we know the regional attenuation and noise. Simulating the detection capability of hypothetical networks within the Soviet Union is difficult because accurate attenuation estimates and noise spectra are not available for that region. Therefore, we use a range of models

90% M_L Detection Threshold

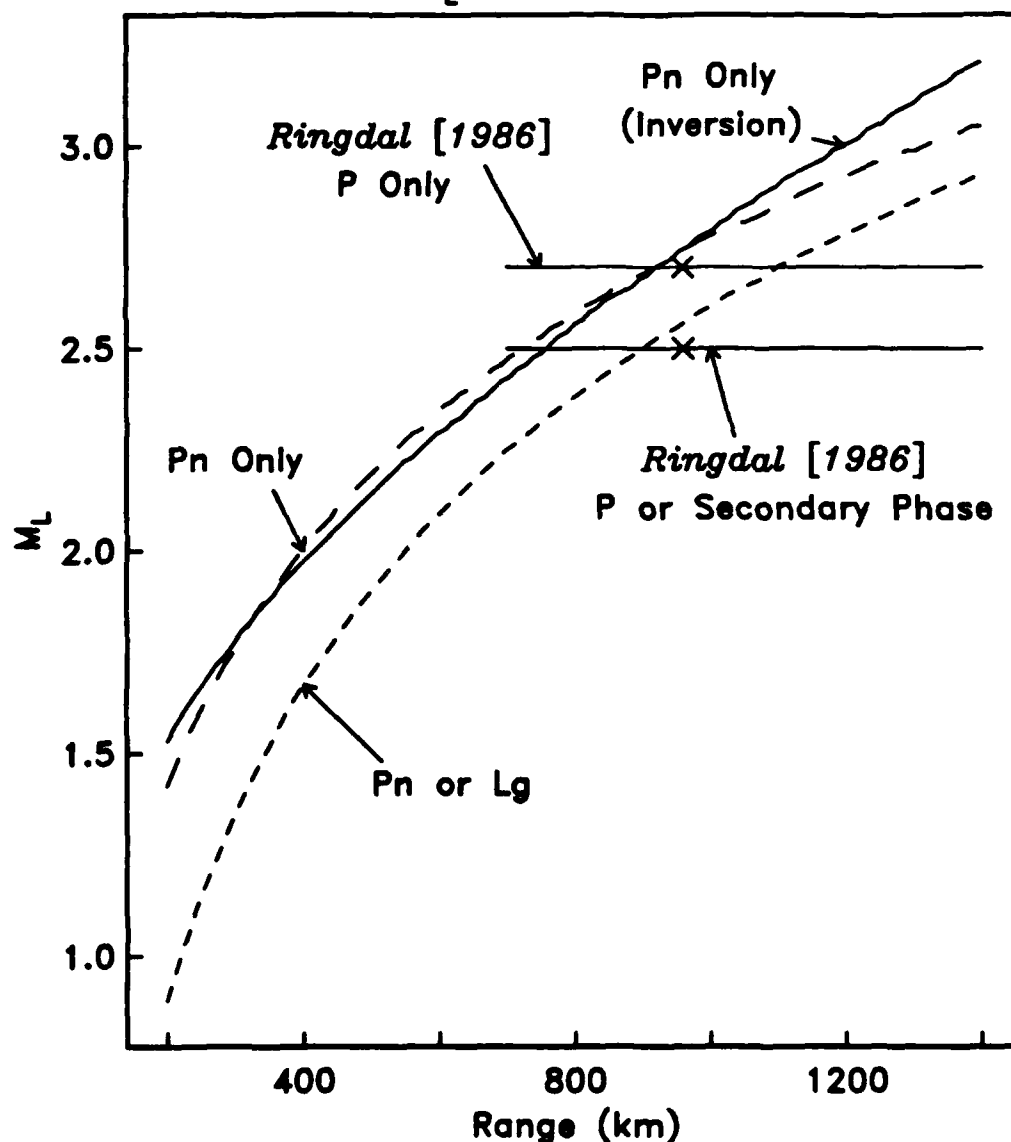


Figure 1.2. Estimates of 90% M_L detection thresholds at NORESS as a function of epicentral distance. The dashed curves are based on a parameterization of observed temporal amplitudes. Curves for detecting Pn and for detecting either Pn or Lg are plotted. The solid curve is based on the results of our inversion of Pn spectra. The horizontal bars are detection thresholds at NORESS as determined by comparing NORESS detections to bulletins produced by local seismic networks [Ringdal, 1986]. Events for this study were at ranges between 700 and 1400 and the average distance was about 960 km (X).

in our network capability simulations to determine the sensitivity of our results to attenuation and noise characteristics. As an example, Figure 1.3 shows a SNAP/DX simulation [Bratt *et al.*, 1987] of the 90% M_L threshold for detecting three Pn phases from a network composed of NORESS-quality stations; 13 outside and 20 inside the USSR. In this case the NORESS detectability, including both attenuation and noise, was used to represent Pn propagation and detection at all stations. That is, Figure 1.3 represents the detection capability if signal and noise are identical to that observed at NORESS throughout the Soviet Union. In terms of NORESS M_L , the threshold is between 2.4 and 2.7 in the Soviet Union. A 50% increase in Pn Q reduces the M_L threshold to between 2.3 and 2.6, and a 50% decrease in Q increases the M_L threshold to between 2.7 and 2.9. Including Lg reduces the M_L threshold by about 0.2 to 0.3. To improve confidence in these simulations of network capability, it will be necessary to obtain accurate estimates of the frequency-dependence of attenuation and noise in the Soviet Union.

1.3.4 Outline of report

This report includes five technical sections. Section 2 reviews the method and results of our generalized inversion of regional wave spectra. This is a summary of material in previous reports [Sereno *et al.*, 1987; Sereno and Bratt, 1988]. Section 3 describes the relationship between temporal and spectral amplitudes and presents our estimates of the detection capability at NORESS. This is a summary of the material presented in our last semi-annual report [Sereno and Bratt, 1988].

Section 4 is new work presented for the first time on detection capability in the Soviet Union. Section 4.1 discusses the procedures and uncertainties involved in extrapolating the NORESS results to simulate the detection capability of a network of seismic stations in the Soviet Union. Section 4.2 presents detection capability simulations for a variety of assumptions about the attenuation and noise in the Soviet Union. Section 5 summarizes our major conclusions developed during the course of this contract, with emphasis on the new results in Section 4.

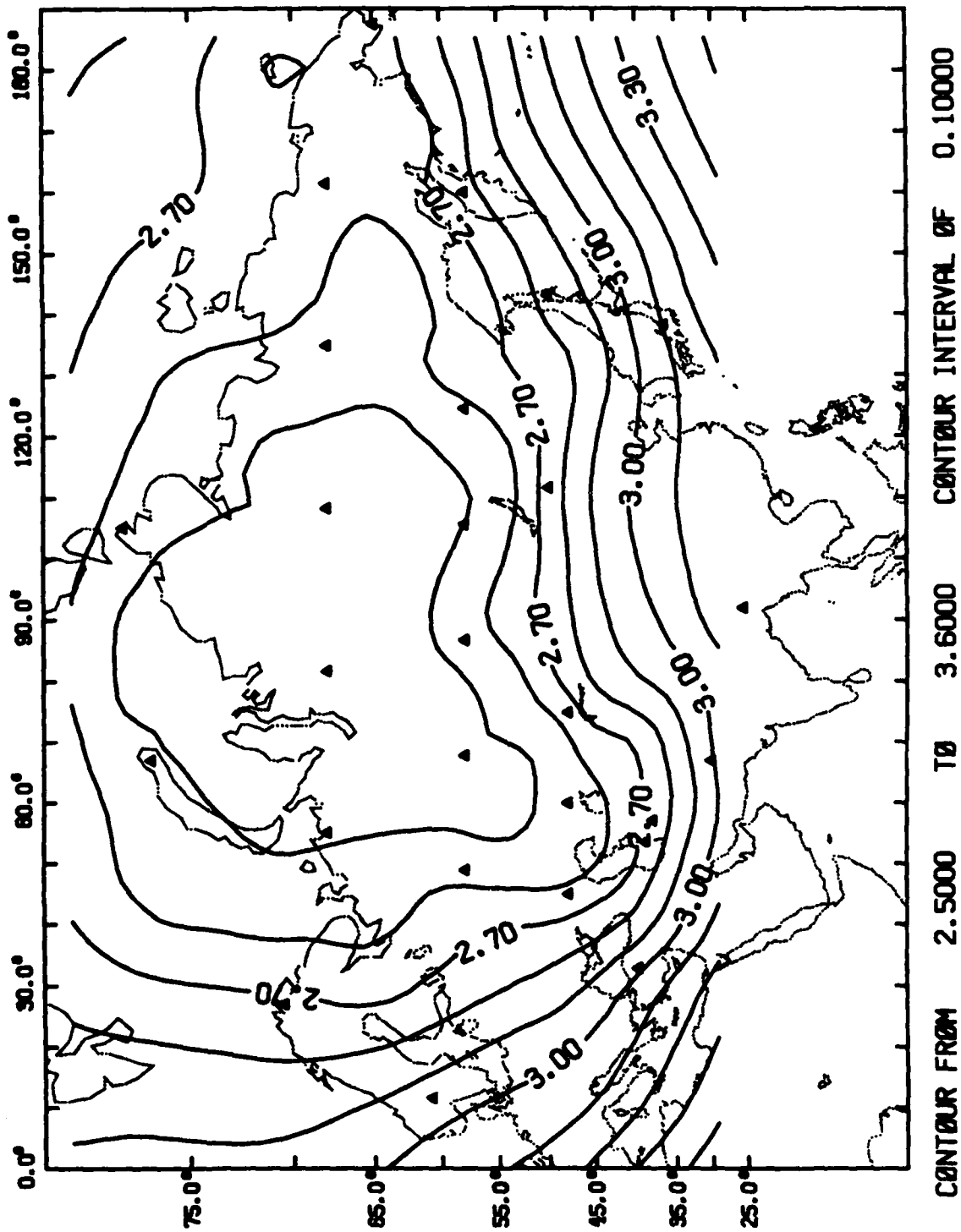


Figure 1.3. Contours of the 90% M_L threshold for detecting 3 P_n phases for a network of NORESS-type arrays; 13 external to the Soviet Union and 20 internal. It is assumed that attenuation and noise are identical to that observed at NORESS.

2. SPECTRAL INVERSION

An important consideration in designing a seismic network intended to monitor compliance with a nuclear test ban treaty is the spectral content of regional wave signals. For example, *Evernden et al.* [1986] argue that efficient high-frequency (> 20 Hz) Pn propagation can be exploited to reduce detection thresholds in the Soviet Union and to aid in event identification. Of course, this implies that high-frequency sensors should be an integral part of the seismic network. However, their argument was based primarily on 1-3 Hz amplitude data from paths in the eastern United States, and the only high-frequency data they use to corroborate their result is a single Pn spectrum recorded at a range of only 190 km. In this section we address this issue with a large data set. This is a summary of the method and results of our previous study of frequency-dependent regional wave propagation for paths to NORESS [*Sereno et al.*, 1987, *Sereno et al.*, 1988]. In these studies, we inverted spectra from 186 regional events covering distances from 200 to 1400 km and magnitudes between 1.1 and 4.8 for both seismic moment and apparent attenuation. Pn spectra were inverted between 1-15 Hz and Lg spectra between 1-7 Hz. The final result is an accurate parameterization of the range and magnitude dependence of these spectra. We note that our results for NORESS are inconsistent with the attenuation model used by *Evernden et al.* [1986], and they do not support their contention of enhanced detection capability at high frequency, except at ranges less than 400-500 km.

2.1 Method

This section is a brief summary of the method we used to estimate attenuation and source parameters. A detailed description is given by *Sereno et al.* [1988]. The analysis assumes a simple source scaling model and that all observed spectra can be fit by a single frequency-dependent Q model. We parameterize the instrument-corrected amplitude spectrum of a seismic signal as

$$A(f,r) = S(f) G(r,r_0) \exp\left[\frac{-\pi f t}{Q(f)}\right] \quad (2.1)$$

where $A(f,r)$ is the observed displacement spectrum at range r and frequency f , $S(f)$ is the source spectrum, $G(r,r_0)$ is geometric spreading, and the last term is the effective attenuation for travel time t . The effective attenuation includes contributions from both anelasticity and scattering.

Source spectra. We adopt a simplified *Mueller and Murphy* [1971] explosion source function characterized by f^{-2} decay beyond a corner frequency that scales inversely with the cube root of the long-period level. While source assumptions have had a controlling influence in some studies of attenuation, they are not crucial for our analysis since most of the events had magnitudes less than 3.0 and apparent corner frequencies beyond the frequency band inverted. The source parameters estimated by the inversion are the long-period level, S_0 , for each event and the corner frequency scaling parameter. The explosion moments are estimated from the long-period levels derived from Pn [*Stevens and Day*, 1985]. Since our observations

are from a single station and the focal mechanisms for the small earthquakes in our data set are unknown, we do not know the radiation pattern and are therefore unable to estimate seismic moment from the earthquake source level derived from Pn . However, since Lg samples a large fraction of the focal sphere, the earthquake moments can be estimated from the long-period source levels derived from Lg [Street *et al.*, 1975]. The relationships we use to estimate seismic moment are

$$M_0^{exp} = 4\pi\rho_s\alpha_s^3 S_0^{exp}(Pn) \quad (2.2)$$

$$M_0^{eq} = 4\pi\rho_c\beta_c^3 S_0^{eq}(Lg) \quad (2.3)$$

where ρ_s and α_s are near-surface density and compressional velocity, ρ_c and β_c are the average crustal density and shear wave velocity, and exp and eq denote explosions and earthquakes, respectively.

The amount of Lg energy excited by an explosion is depth-dependent and complicated by near-source wave conversions [Bennett *et al.*, 1987]. Explosions generate Lg energy primarily through P - SV mode conversions and scattering, while earthquakes produce much more direct shear wave energy. Therefore, for a given source moment and focal depth, earthquakes are expected to generate larger Lg amplitudes than explosions. We will express the long-period Lg source level for an explosion as an unknown fraction of the long-period level for an earthquake of equal moment and depth. That is,

$$S_0^{exp}(Lg) = \kappa S_0^{eq}(Lg) \quad (2.4)$$

where κ is an unknown constant, presumably less than one. We estimate this constant using (2.2), (2.3), and (2.4), together with the observed ratio of $S_0^{exp}(Lg)$ to $S_0^{exp}(Pn)$.

Geometric spreading. The inversion also requires that we assume the geometric spreading function. Following Herrmann and Kijko [1983], we express the spreading function in the frequency domain as

$$\begin{aligned} G(r,r_0) &= (1/r) && \text{for } r \leq r_0 \\ G(r,r_0) &= r_0^{-1} (r_0/r)^m && \text{for } r \geq r_0 \end{aligned} \quad (2.5)$$

where r_0 is a transition distance from spherical spreading to spreading rate m . The Lg phase consists of higher-mode surface waves which are accurately described at long ranges by cylindrical spreading ($m = 1/2$), provided the window length is sufficient to encompass the entire dispersed wave train. By comparing the long-period amplitude spectrum of Lg to moments calculated from long-period surface waves, Street *et al.* [1975] empirically determined $r_0 = 100$ km, or roughly twice the crustal thickness. Measuring the decay rate of synthetic Lg phases computed for an elastic medium, Herrmann and Kijko [1983] verified that Lg frequency domain spreading was accurately described as cylindrical and substantiated the empirical result of Street *et al.* [1975] for r_0 . Therefore, we adopt (2.5) with $r_0 = 100$ km and $m = 1/2$ to approximate Lg geometric spreading.

Less work has been done on the spreading rate of Pn . Because its energy density is more localized about a single ray path, Pn geometric spreading is more sensitive to velocity gradients in the upper mantle. Numerical studies of Pn indicate that for typical upper mantle structures the spreading rate lies between r^{-1} and r^{-2} [Langston, 1982; T. C. Wallace, personal communication, 1987]. We find that an important constraint on Pn spreading is the consistency of the derived source parameters from the separate Lg and Pn inversions. This criterion supports a choice of $r^{-1.3}$ for the Pn spreading rate. Therefore we use (2.5) with $r_0 = 1$ km and $m = 1.3$ to describe Pn spreading. We experimented with other spreading rates and found only minor differences in Q . A change in the assumed spreading rate simply trades-off with derived moment since the observations are from a single station.

Effective attenuation. We characterize the range-dependent decay of the seismic spectrum in terms of a power law frequency dependence of Q . That is,

$$Q(f) = Q_0 f^\eta \quad (2.6)$$

where Q_0 and η are parameters of the inversion. No attempt is made to distinguish intrinsic absorption from scattering. In this form, our results are easily compared to those for other geographic regions. We have not accounted for any azimuthal variations in Q , but have combined data from all azimuths into an inversion for a single, average Q model. Examination of the fit of the model to the data demonstrates the validity of this procedure.

Inversion. The input data for the inversion are the logarithms of the observed displacement spectra corrected for the assumed geometric spreading. These data are inverted for apparent attenuation, source moment, and the constant relating corner frequency and moment. Adopting standard methods for solving non-linear inverse problems, we linearize the system of equations governing the relationship between the data and model parameters. We assume a starting model, compute theoretical data, subtract it from the observed data, and solve iteratively for the model perturbations that minimize the data residual in the least squares sense. In practice, we have found it necessary to include damping to stabilize the solution. That is, we minimize a weighted sum of the data residuals and the model perturbation norm. The explicit problem formulation, matrices, and partial derivatives are given by Sereno *et al.* [1987].

2.2 Data

The data used in this study consist of stable, array-averaged spectra for 186 regional events recorded by the small aperture NORESS seismic array in Norway. Event magnitudes range between 1.1 and 4.8 and epicentral distances are between 200 and 1400 km. The array includes 25 short-period instruments in concentric rings with a maximum diameter of 3 km. The data are digitally recorded at 40 samples per second. The NORESS short-period instrument response is approximately flat to velocity between 1 and 10 Hz.

Signal processing. The Pn spectra were calculated as part of an automated seismic array processing program (SAIAP) developed as an extension of the RONAPP program used at NOR-SAR [Mykkeltveit and Bungum, 1984]. The program computes spectra for each automatically detected signal. The spectral estimation technique is that proposed by Bache *et al.* [1985]. A 10% cosine-squared taper is applied to a 5-s window starting 0.3 s before the onset time of the

arrival on the vertical component. The time series is padded with zeros to 512 samples and fast Fourier transformed. The same procedure is applied to a noise sample taken prior to the first P detection. The squared noise amplitude spectrum (power) is subtracted from the squared signal spectrum (energy density). The resulting noise-corrected signal spectra are averaged across the array and corrected for the instrument response. *Bache et al.* [1985] show that if the noise is random, stationary, and uncorrelated with the signal, the signal spectrum estimate obtained with this method converges to the true signal spectrum as the number of elements increases. Array averaging also has the desirable effect of suppressing uncorrelated local site effects. We experimented with P_n window lengths of 5, 10, and 15 s and found that the spectra are insensitive to that parameter.

The inversion results presented here were obtained using L_g spectra computed for a fixed group velocity window of 3.6-3.0 km/s. The spectra were computed for each array element, corrected for the ambient (pre- P_n) noise, and array-averaged using the method of *Bache et al.* [1985]. Our low group velocity cutoff was chosen as 3.0 km/s because our events typically produced L_g phases with low signal-to-noise for group velocities less than this. Fixed group velocity windows ensure that the same modes contribute to the L_g spectrum at all epicentral distances. The Q estimated from these spectra is a measure of the average absorption of shear waves in the crust [e.g., *Campillo et al.*, 1985]. However, the energy distributed over such a long time window (56 s at 1000 km) is not an appropriate measure for detection capability assessment. We find the spectra computed for short fixed time lengths are more appropriate for that application. *Sereno and Bratt* [1988] compare the inversion results using L_g spectra computed with fixed group velocity and fixed time length windows.

Events. Figure 2.1 plots the epicenters of all of the events used in the inversion. A complete list of locations, origin times, and magnitudes are given by *Sereno and Bratt* [1988]. The location and origin times are from a local bulletin published by the University of Bergen or the University of Helsinki, when available, or from the Preliminary Determination of Epicenters (PDE) bulletin. Events for which an independent network solution is not available are assigned SAIAP locations. The M_L are based on the L_g amplitude computed by RONAPP. They differ slightly from the RONAPP M_L in the NORESS bulletin by being distance-corrected to the event location computed by one of the independent networks.

Mining explosions are reported in the Helsinki bulletin and by the University of Bergen. Events that are not reported explosions, but have locations within 50 km of a known mine are considered of unknown source type. Other events are presumed to be earthquakes. The 186 events include 107 explosions, 63 presumed earthquakes, and 16 events of unknown source type. In some cases only one phase was included because the other was not detected or because it had a low signal-to-noise ratio over the frequency band used in the inversion. The P_n inversion included 152 events, with 83 explosions, 56 presumed earthquakes, and 13 events of unknown source type. The L_g inversion used 160 events, including 92 explosions, 53 presumed earthquakes, and 15 unknown. Of the 186 events, 126 were used for both the P_n and the L_g analyses.

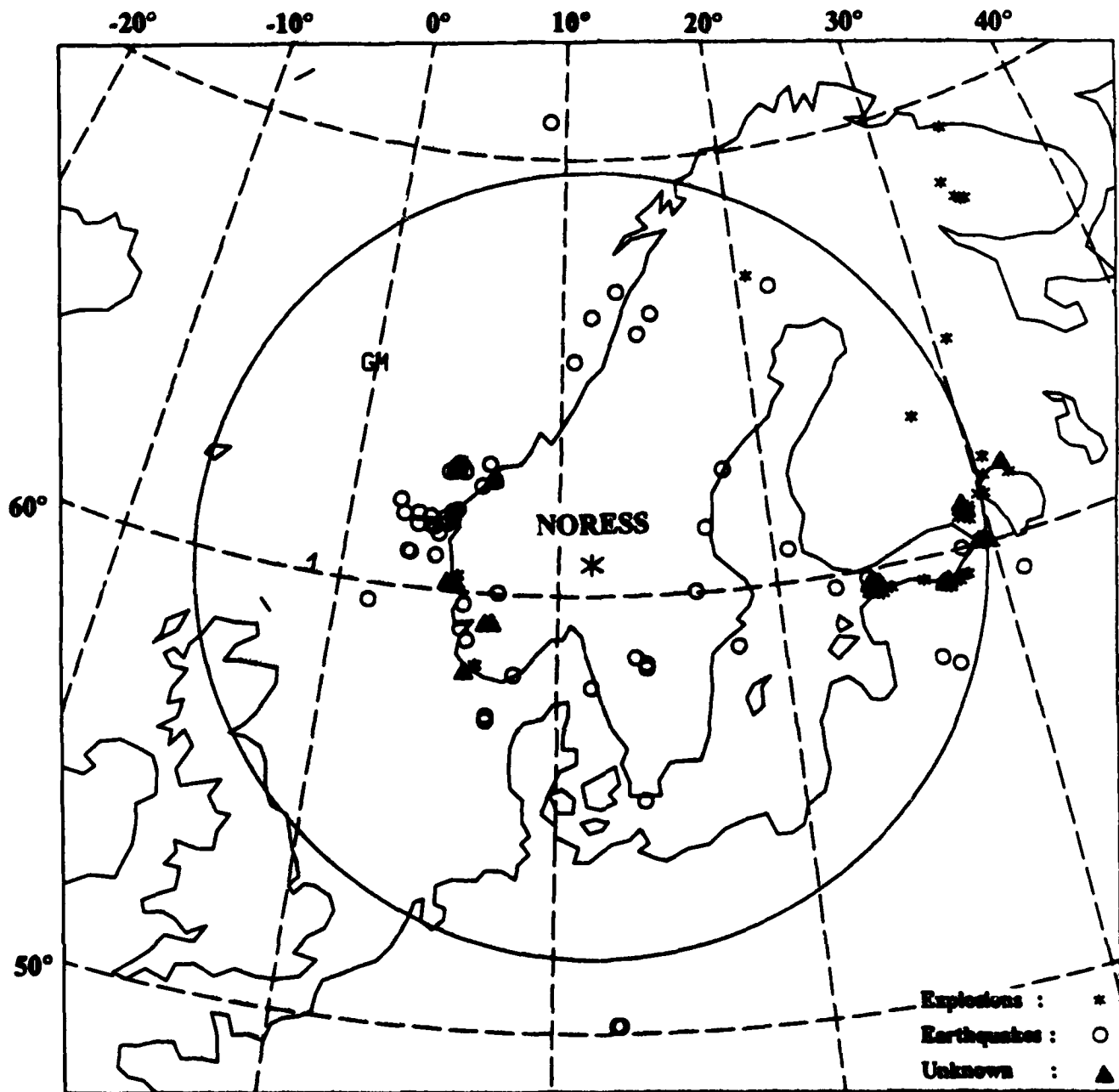


Figure 2.1. Map of the epicenters of events used in the inversion. Earthquakes, explosions, and sources of unknown type are plotted with different symbols. The total number of events is 186. Of these, 152 were used in the P_n inversion and 160 were used in the L_g inversion.

2.3 Results

2.3.1 Seismic moment and Q

For a fixed set of source and spreading assumptions, the separate Pn and Lg inversions each define a range of models consistent with the observations. For example, the Pn inversion produced models with Q between $200 f^{0.60}$ and $500 f^{0.40}$ that differed in data variance by less than 5%. Similarly, Lg Q models between $420 f^{0.36}$ and $570 f^{0.26}$ produce data variances that differ by less than 2%. To resolve these parameter trade-offs, we impose the constraint that the separate Pn and Lg inversions give an internally consistent set of source parameters. In particular, we require that the ratio of the Lg and Pn source levels be independent of epicentral distance. This reduces the range of acceptable models to a set of model pairs consistent with both sets of observations. Table 2.1 lists examples of these model pairs. Note that none of Lg models are consistent with Pn Q_0 greater than 350.

Table 2.1. Q Models With Internally Consistent Source Parameters

Q_{Lg}	Q_{Pn}
$420 f^{0.36}$	$225 f^{0.57}$
$500 f^{0.30}$	$280 f^{0.52}$
$560 f^{0.26}$	$325 f^{0.48}$

There is no obvious basis for choosing among these model pairs. However, *Sereno et al.* [1988] note that a trade-off exists between data variance and variance in the moment-magnitude relationship. Based on this trade-off, they selected $Q_{Lg}(f) = 560 f^{0.26}$ as their "preferred" model. Applying the source consistency constraint, this supports a Pn Q model with $Q_0 = 325$ and $\eta = 0.48$. Although this trade-off analysis is subjective, it is only used to choose among a relatively small range of Q_{Lg} models.

The earthquake moments are estimated from the source levels derived from Lg using (2.3) with $\rho_c = 2.7 \text{ gm/cm}^3$ and $\beta_c = 3.5 \text{ km/s}$. The explosion moments are derived from $S_0^{\text{exp}}(Pn)$ using (2.2) with $\rho_s = 2.5 \text{ gm/cm}^3$ and $\alpha_s = 5.0 \text{ km/s}$. Figure 2.2 displays the derived source moments as a function of NORESS M_L . The solid lines indicate the least squares linear fits given by

$$\log M_0^{\text{exp}} = 1.08 M_L + 17.6 \quad (2.7)$$

$$\log M_0^{\text{eq}} = 1.03 M_L + 17.1 \quad (2.8)$$

However, because of an uneven distribution of magnitudes in our explosion data set, the least squares fit does not adequately represent the observed M_L dependence of $\log M_0$. The fit

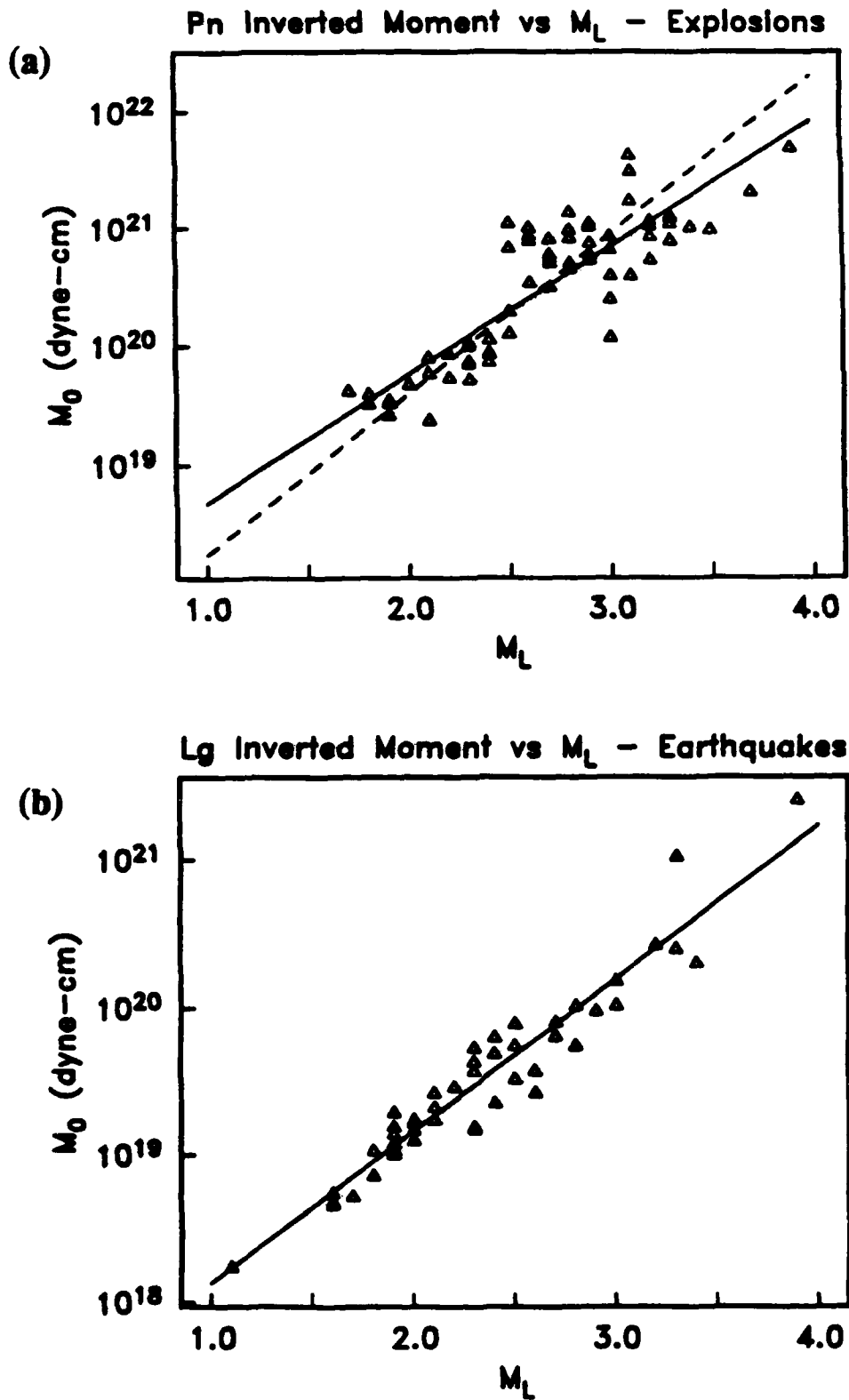


Figure 2.2. Inverted moment versus NORESS local magnitude for (a) explosions and (b) earthquakes. The explosion moments were derived from Pn and the earthquake moments were derived from Lg . The least-squares linear fit of $\log M_0$ to M_L is plotted as the solid line in each figure. The dashed line in Figure 2.2a plots the linear trend for explosions fitted by eye.

underestimates the moments of large events and overestimates the moments of small events. Therefore, we simply fit the linear trend by eye. The result is the dashed line in Figure 2.2 which is expressed as

$$\log M_0^{\text{exp}} = 1.35 M_L + 16.90 \quad (2.9)$$

The coefficient of M_L is higher than that expected if M_L is approximately equal to m_b . The explosion moments derived from Lg spectra display a similar rate of increase with M_L , while the earthquake log moments display much less scatter and increase at a rate close to $1.0 M_L$ (Figure 2.2b). Therefore, it is not likely that inaccurate attenuation parameters are responsible for the high M_L coefficient observed for explosions. Since M_L is based on Lg amplitude, it is possible that the high M_L coefficient is due to complexity in Lg excitation by explosions.

Sereno et al. [1988] determine the sensitivity of the inversion results to assumptions about the Pn geometric spreading rate. Spreading rates of r^{-1} , $r^{-1.3}$ and $r^{-1.5}$ were explicitly investigated, and for each there is a Q model that can adequately reproduce the Pn spectra. However, since our parameterization of geometric spreading is frequency-independent and our data is from a single station, changes in the assumed spreading rate trade-off directly with the source moment, and have very little effect on the range of Q models produced by the Pn inversion. However, an important constraint on the Pn spreading rate is the relative excitation of Lg for explosions and earthquakes of equal moment. That is, since κ in (2.4) is estimated using the explosion moments derived from Pn , the most dramatic effect of changing the Pn spreading rate is the implied change in the relative Lg excitation of explosions and earthquakes. We find that for earthquakes and explosions of equal moment, $\kappa = 0.27$ for our "preferred" attenuation model. This means that the average Lg earthquake excitation is approximately four times the average Lg explosion excitation for sources of equal moment. This is consistent with results of previous studies that compared Lg amplitudes from approximately collocated earthquakes and explosions [e.g., Willis, 1963; Pomeroy, 1977; Nutli, 1981]. Assumed Pn spreading rates much different from $r^{-1.3}$ give earthquake to explosion Lg excitation ratios which are inconsistent with these empirical observations [see *Sereno et al.*, 1988].

Table 2.2 summarizes the inversion results for our "preferred" model. The only parameter not listed is corner frequency. Corner frequency was assumed to scale inversely with the cube-root of the moment. Our results indicate that an $M_L = 3.0$ event has an approximate corner frequency of 10 Hz, although our data do not accurately resolve that parameter. However, we note that our results are within a few hertz of those from near-field estimates for events with the same local magnitude [*Bungum et al.*, 1982; *Mueller and Cranswick*, 1985]. Figure 2.3 shows some examples of the fit of our model to the observed spectra. The spectra are plotted over the bandwidth inverted; 1-15 Hz for Pn and 1-7 Hz for Lg . These examples are typical of the quality of the fits that were obtained for most of the events. A complete catalog comparing observed and predicted spectra is given by *Sereno and Bratt* [1988].

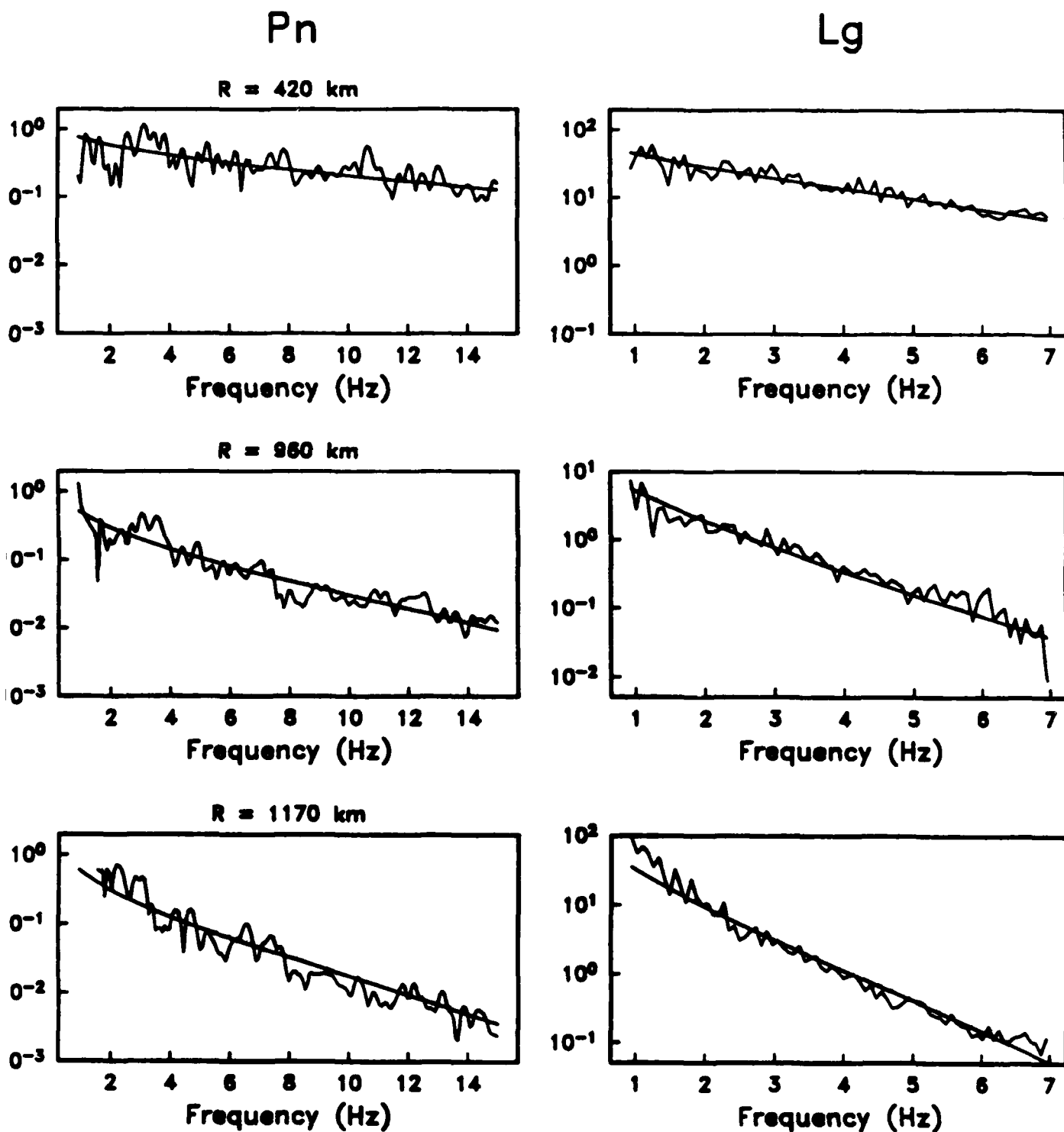


Figure 2.3. Selected examples of the fit of P_n and L_g spectra based on the inversion results to observed spectra. The P_n spectra are plotted on the left and the L_g spectra on the right. The spectra are plotted over the frequency band used in the inversion. The spectra on the top are from an earthquake 420 km from NORESS, the spectra in the middle are from a mining explosion at 960 km, and the spectra on the bottom are from an earthquake at 1170 km. The spectral amplitudes are in nanometer-seconds.

Table 2.2. Inversion Results

	$Q(f)$		Geometric Spreading		Source Terms		
	Q_0	η	r_0	m	$\log M_0^{\text{exp}}$	κ	$\log M_0^{\text{eq}}$
<i>Pn</i> :	325	0.48	1.0	1.3	$1.35M_L + 16.9\dagger$	---	---
<i>Lg</i> :	560	0.26	100.0	0.5	$1.35M_L + 16.9\dagger$	0.27	$1.03M_L + 17.1$

† Fit by eye.

2.3.2 Simulation of NORESS spectra

Based on the inversion parameters in Table 2.2, it is possible to simulate spectra at NORESS for a chosen source and epicentral distance. For example, Figure 2.4 displays predicted *Pn* and *Lg* spectra at distances of 500, 800, and 1000 km for an $M_L = 3.0$ explosion. The lower curve is the average ambient noise spectrum at NORESS [Suteau-Henson and Bache, 1988]. The *Pn* spectrum is nearly parallel to the noise curve at range of about 500 km. This is consistent with a NORSAR study that examined data from the high-frequency element of the NORESS array [Ringdal *et al.*, 1986]. At longer ranges the frequency of the maximum signal-to-noise ratio (SNR) is considerably less than 15 Hz. For example, for distances greater than 1000 km the predicted frequency of the maximum SNR is between 4-5 Hz. Thus our results for NORESS do not support the main conclusion of Evernden *et al.* [1986], that *Pn* detection capability would be enhanced at frequencies greater than 20 Hz, except at distances less than 400-500 km.

A similar interpretation for *Lg* is not possible since we don't have a parameterization of pre-*Lg* noise (the ambient noise curve is plotted with the *Lg* spectra in Figure 2.4 only for comparative purposes). The pre-*Lg* noise is non-stationary because it includes the coda of previously arriving phases. Here we simply note that the *Lg* spectrum reaches the noise level at a much lower frequency than the *Pn* spectrum, while at long periods the *Lg* amplitude exceeds that of *Pn* by as much as a factor of 10. This is consistent with the observation that regional seismograms are characterized by *Lg* being the largest-amplitude phase and *Pn* having a higher dominant frequency.

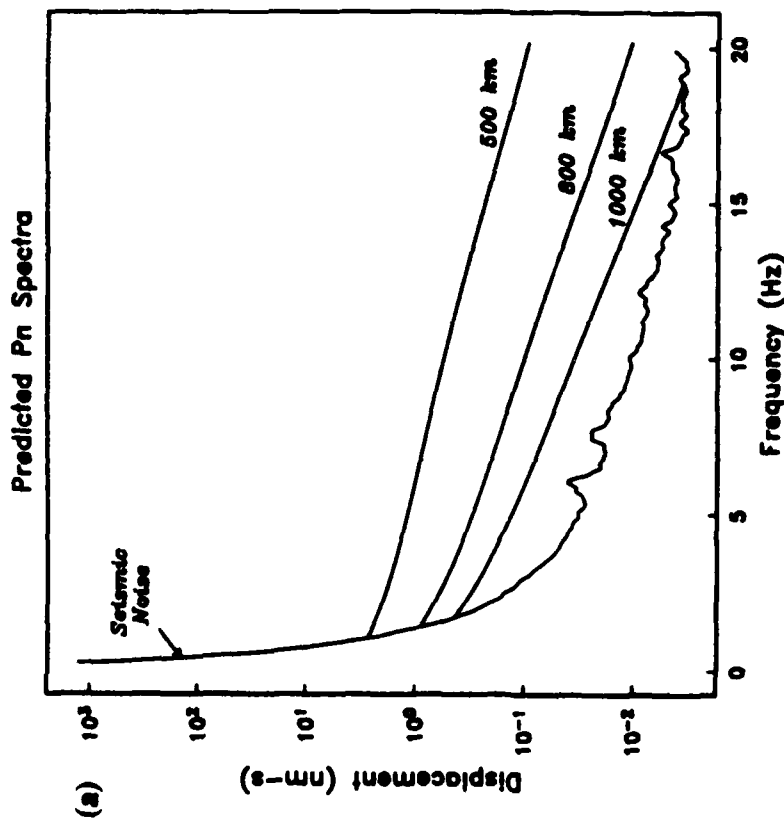
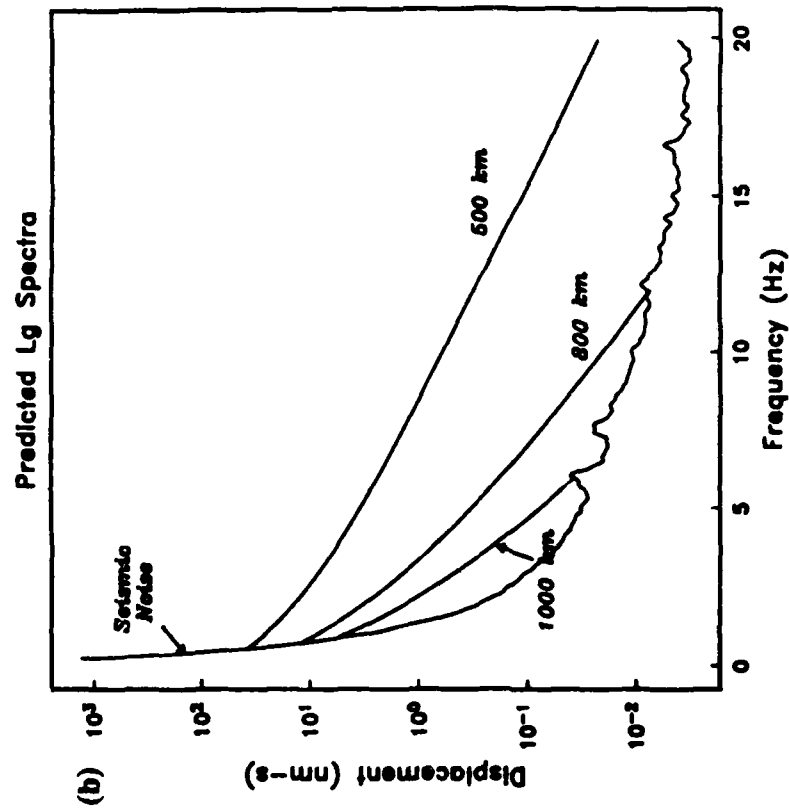


Figure 2.4. Predicted NORESS (a) P_n and (b) L_g displacement spectra at three epicentral distances for a magnitude 3.0 explosion, based on the inversion results. The average NORESS noise was estimated from 43 5-s samples taken prior to P_n [Suwau-Henson and Bache, 1988].

3. TEMPORAL AMPLITUDES AND DETECTABILITY

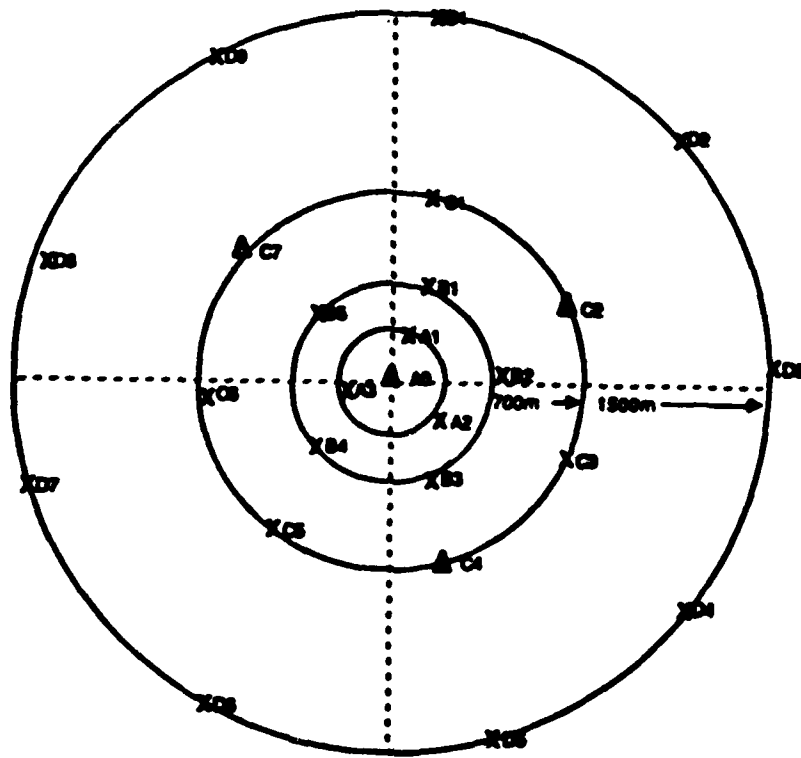
Signal detection at NORESS is declared when the short term average (STA) divided by the long term average (LTA) exceeds a predetermined threshold. These amplitudes are measured on filtered beams. Therefore, to use our spectral parameterization to predict and extrapolate NORESS detection capability, it is necessary to determine the relationship between single-channel spectral amplitudes and the time-domain amplitudes used in signal detection. In this section we determine this relationship and use it to compare predictions based on our inversion results to observed NORESS detection capability.

We start by comparing observed detection statistics at NORESS to predictions based on our spectral parameterization. Next, we determine the relationship between temporal and spectral amplitudes on filtered beams. In Section 3.2.3, we combine this with estimates of the frequency-dependent beam gain to develop an expression for the temporal SNR on a filtered beam in terms of single-channel spectral amplitudes. In Section 3.3, we define a function called the "detectability" that gives simple and accurate estimates of the NORESS detection capability directly from the observed temporal SNR ($=\text{STA}/\text{LTA}$).

3.1 Detection statistics

Detection and post-detection processing of NORESS data is done by the automated array-processing package, *SAIAP*. The detection processing is identical to that in *RONAPP* [Mykkeltveit and Bungum, 1984], and uses a conventional STA/LTA detection algorithm applied to a set of filtered beams. The output of *SAIAP* includes the STA and LTA for each detection measured on the standard beam with greatest signal-to-noise ratio (SNR). The NORESS array configuration is shown in Figure 3.1. Table 3.1 lists the standard beams used by *SAIAP*. Beams 1-7 and 17-20 are infinite-velocity beams, 8-16 are steered beams, and 21-24 are formed from horizontal components. No more than three steering azimuths are used for a given frequency filter. Beams 1-17 are coherent beams and 18-24 are incoherent beams. Coherent beams are formed by delaying each channel by the proper amount determined from the steering azimuth and velocity, summing all channels, and band-pass filtering. Incoherent beams are formed by band-passing each channel, delaying and rectifying, and summing all channels. Incoherent beams are particularly well-suited for detection of signals with low coherency across the array [Ringdal, 1985b]. For example, all but one of the P_n detections used in this study are on coherent beams, whereas 68% of the L_g detections are on incoherent beams.

The most fundamental observation that our spectral parameterization should reproduce is the distance dependence of the frequency of the maximum SNR. This frequency depends primarily on the Q , since most of the events have $M_L \leq 3.0$ and high apparent corner frequencies. Figure 3.2 shows the percentage of P_n and L_g detections for several frequency bands at four ranges. Although a phase may be detected on many beams, it is plotted in Figure 3.2 only for the frequency band for the beam with the maximum SNR. As expected, detections from close events generally occur on a higher-frequency beam than those from events at larger distances. For example, the maximum SNR for P_n typically occurs at a frequency greater than



CENTER: 60.7363N, 11.6414E

X - SINGLE VERTICAL INSTRUMENT
 Δ - THREE COMPONENT INSTRUMENT

Figure 3.1. NORESS array configuration. The array consists of 25 short-period instruments in concentric rings with a maximum diameter of 3 km. The array was designed for the enhancement of frequencies between 1.5 and 5.0 Hz [Mykkeltveit, 1983].

Beam	Azi	Slow	Filter	Type	Weights	Threshold
					AAAAAABBBBBCCCCCCCCCCCCDDDDDDDDDD	
					000123123451222344456777123456789	
					ZENZZZZZZZZZZZENZZENZZENZZZZZZZZZ	
1	0.	0.00	1.0-3.0	C	100000000001100110011100111111111	4.0
2	0.	0.00	1.5-3.5	C	100000000001100110011100111111111	4.0
3	0.	0.00	2.0-4.0	C	100000111111100110011100111111111	4.0
4	0.	0.00	2.5-4.5	C	100000111111100110011100000000000	4.0
5	0.	0.00	3.0-5.0	C	100000111111100110011100000000000	4.0
6	0.	0.00	4.0-8.0	C	1001111111100000000000000000000	5.0
7	0.	0.00	8.0-16.0	C	1001111111100000000000000000000	5.0
8	0.	0.07	2.0-4.0	C	100000111111100110011100111111111	4.0
9	90.	0.07	2.0-4.0	C	100000111111100110011100111111111	4.0
10	180.	0.07	2.0-4.0	C	100000111111100110011100111111111	4.0
11	15.	0.07	2.5-4.5	C	100000111111100110011100111111111	4.0
12	75.	0.07	2.5-4.5	C	100000111111100110011100111111111	4.0
13	135.	0.07	2.5-4.5	C	100000111111100110011100111111111	4.0
14	25.	0.07	3.0-5.0	C	100000111111100110011100111111111	4.0
15	75.	0.07	3.0-5.0	C	100000111111100110011100111111111	4.0
16	125.	0.07	3.0-5.0	C	100000111111100110011100111111111	4.0
17	0.	0.00	2.0-4.0	C	100000111111100110011100000000000	4.0
18	0.	0.00	1.0-2.0	I	100000000001100110011100000000000	2.5
19	0.	0.00	2.0-3.0	I	100000000001100110011100000000000	2.5
20	0.	0.00	2.0-4.0	I	100000000000000000000000011111111	2.1
21	0.	0.00	2.0-4.0	I	010000000000010001000010000000000	6.0
22	0.	0.00	2.0-4.0	I	001000000000000100010000100000000	6.0
23	0.	0.00	4.0-8.0	I	010000000000010001000010000000000	6.0
24	0.	0.00	4.0-8.0	I	001000000000000100010000100000000	6.0

Table 3.1. Standard Beams used by SA/AP. Listed are beam number, steering azimuth (deg) and slowness (s/km), frequency filter (Hz), beam type (coherent or incoherent), sensor weights, and detector thresholds. The individual sensors are identified by ring (A-D), sensor number (0-9), and component (Z, N, or E). The thresholds were determined from false alarm statistics [Kvaerna et al., 1987a].

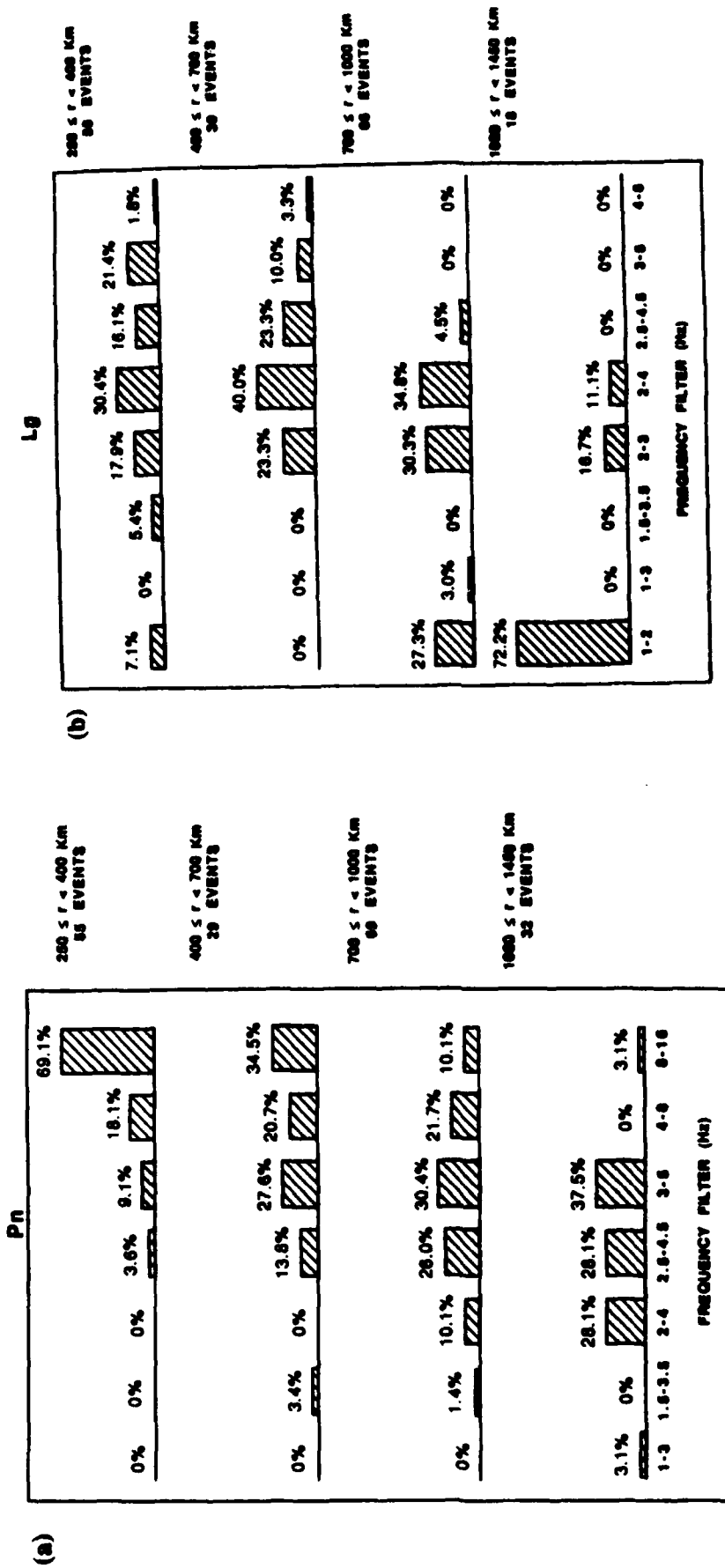


Figure 3.2. Percentage of detections with the maximum SNR for each frequency filter grouped into four distance ranges for (a) Pn and (b) Lg. The distance intervals and the number of events for each interval are indicated on the right.

8 Hz at distances less than 400 km and between 3-5 Hz in the 700-1000 km distance range. This is consistent with the results of Ringdal [1985a] who found that the best SNR for P_n increased from 3-5 Hz at about 1000 km to more than 8 Hz at local distances. Note that the predicted P_n spectra shown in Figure 2.4 are generally consistent with these observations. A similar comparison for L_g is not possible since we don't have a parameterization of the pre- L_g noise spectrum. However there is at least qualitative agreement between the predicted and observed dominant frequency of L_g .

3.2 Relationship between spectral and temporal amplitudes

In this section we determine the relationship between temporal and spectral amplitudes on filtered beams, and combine this with estimates of the frequency-dependent beam gain to determine the relationship between the SNR used in signal detection and the single channel spectral SNR. Since L_g is strongly dispersed and the pre- L_g LTA is non-stationary, we are unable to parameterize the L_g SNR in a form suitable for extrapolation. Therefore, in this section we concentrate on P_n .

3.2.1 Noise

Qualitatively, the LTA is a measure of the RMS amplitude on a filtered beam averaged over about 30 s prior to a detection. The LTA is updated every 0.5 s and is expressed as a weighted sum of past STAs. There is a simple relationship between the RMS amplitude of random noise and its power spectral density [e.g. Aki and Richards, 1980; p. 493]. From Parseval's theorem

$$A_{RMS} \approx (2 PSD \Delta f)^{1/2} \quad (3.1)$$

where Δf is the bandwidth and PSD is the power spectral density. This equation assumes that the PSD is flat over the bandwidth Δf . The LTA for P_n is an approximate measure of the RMS ambient noise amplitude on a filtered beam and should be approximately related to the PSD of the beam by (3.1), where Δf is the filter bandwidth.

To test the applicability of (3.1) to pre- P_n (or ambient) noise, we computed spectra of unfiltered beams over various sub-arrays. Figure 3.3 compares the average noise spectra recorded on unfiltered beams over the four sub-arrays used in the standard beams to the average single-channel noise spectrum [Suteau-Henson and Bache, 1988]. For frequencies less than about 4 Hz the noise level is significantly reduced by including the two outer rings of the array. In particular, the beam including sensors on only the C and D rings gives better noise suppression than can be achieved using the whole array [Kvaerna and Mykkeltveit, 1986]. However, beyond 5-6 Hz only marginal improvement in noise suppression can be achieved by including the outer rings. Superimposed on the spectra are the squared LTAs divided by $2\Delta f$ for the 186 P_n detections. The LTAs are corrected for the instrument response and plotted at the frequency of the mean power in the bandwidth Δf . Note that the LTAs measured on the 8-16 Hz beam are consistent with (3.1) at a frequency of about 9.5 Hz. This is an important distinction for detection capability assessment. This implies that the temporal SNR cannot be

Noise Spectra and LTA

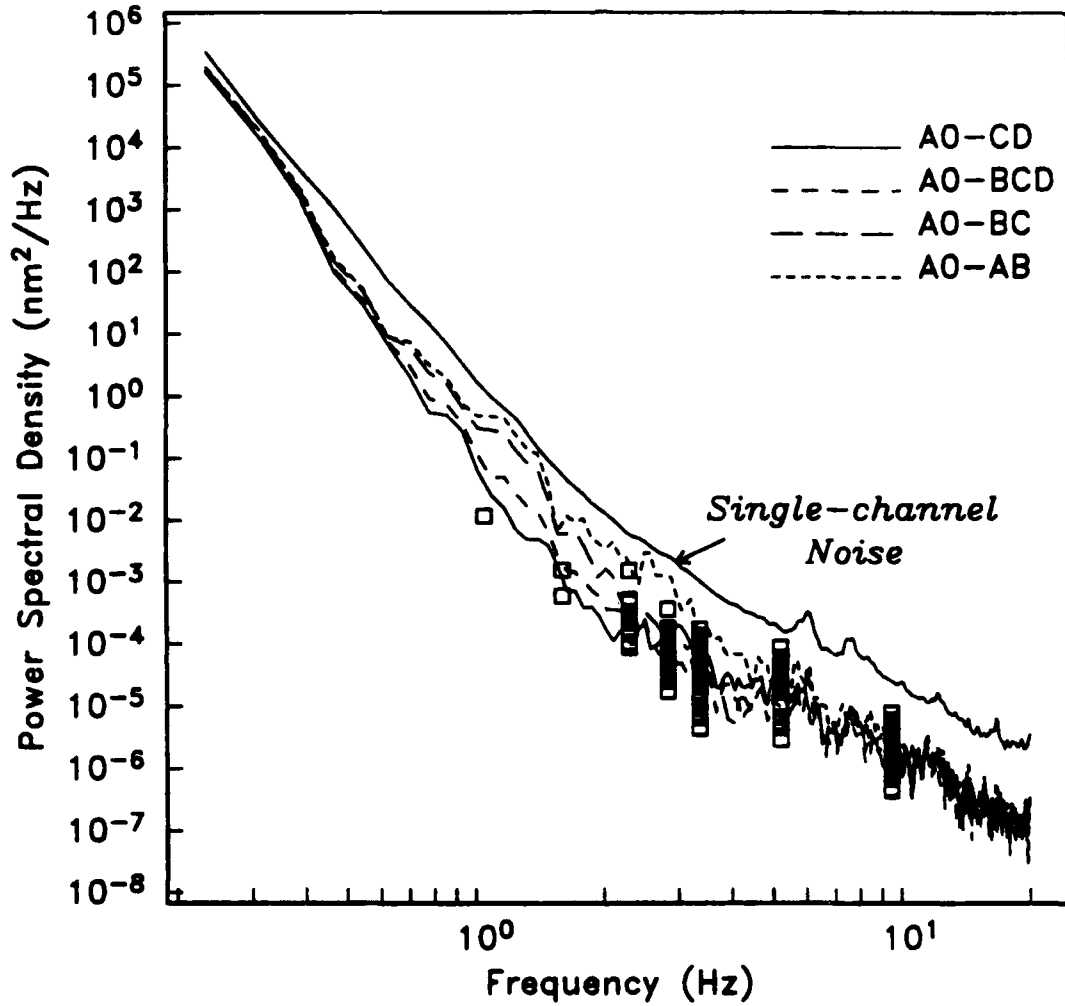


Figure 3.3. Average NORESS ambient noise power spectral density. The array-averaged single-channel spectrum is from *Suteau-Henson and Bache* [1988]. The beam spectra are averages of 10 noise samples calculated for the various sub-arrays. All spectra are corrected for the instrument response. The symbols are P_n -LTAs divided by $2\Delta f$ for 186 events.

predicted based on a spectral parameterization of the signal and the noise at the same frequency, unless narrow band filters are used in beamforming. Otherwise the dominant signal frequency may exceed the dominant noise frequency within the filter bandwidth. This is discussed in more detail in a later section.

The noise suppression is defined as the ratio of the beam power spectrum to the array-averaged single-channel power spectrum [Fyen, 1986]. In general, we find that at least $1/N$ noise suppression (where N is the number of array elements used in beamforming) is achieved over the frequency band used for each of the sub-arrays. However, the signals are also suppressed by beamforming, and this must also be considered in establishing the frequency-dependent beam gain (Section 3.2.3).

The pre- L_g noise consists of ambient noise, P coda, and S_n coda. Therefore, we do not expect a simple relationship between L_g -LTA and the ambient noise spectrum. Furthermore, we don't have a parameterization of the single-channel pre- L_g noise spectrum, so there is no reason to relate temporal and spectral amplitudes as was done for P_n . Therefore, we simply parameterize the L_g -LTA in terms of distance, frequency, magnitude, and beam type [Serenio and Bratt, 1988]. We find that the L_g -LTA decreases with increasing distance and frequency, but that the most important effect for detection capability assessment is that of magnitude. Figure 3.4 plots L_g -LTA versus NORESS local magnitude. The best-fitting straight line to log LTA as a function of magnitude has a slope near 0.8 for both coherent and incoherent beams. Since both L_g signal and "noise" increase with increasing M_L , this implies that the detectability of L_g is much less dependent on magnitude than that of P_n .

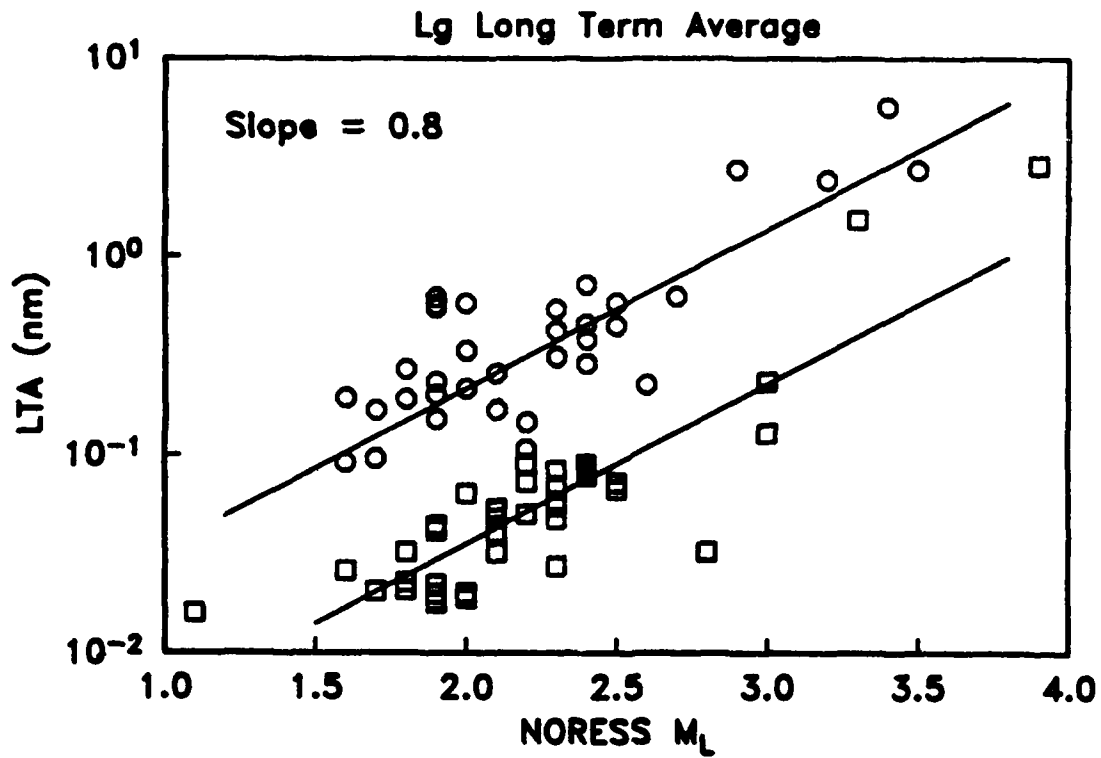


Figure 3.4. Magnitude dependence of pre-*Lg* noise. The log *Lg*-LTA are plotted versus NORESS local magnitude for detections on coherent (squares) and incoherent (circles) beams. The solid lines indicate a slope of 0.8. The LTAs have been corrected for the instrument response.

3.2.2 Signal

The P_n spectra used in this study are those automatically computed by *SAIAP* for each detected phase. They are computed for a 5-s window starting 0.3 s before the detection time on the vertical component and are noise-corrected and averaged across the array. In this section, we examine the relationship between these spectral amplitudes and the time-domain STA amplitude on a filtered beam. However, the L_g energy distributed over the fixed group velocity window used in the inversion is not an appropriate measure for detection capability assessment. We find that the L_g spectral amplitudes computed for 5-s windows are more appropriate for that application. Specifically, we find that the L_g -STA are proportional to these spectral amplitudes, and that the proportionality constant depends only on beam type [*Sereno and Bratt, 1988*]. However, since $L_g Q$ estimates based on these spectra are not available for other regions, our results for L_g are not easily extrapolated. Therefore, the remainder of this section concentrates on the relationship between spectral and temporal P_n amplitudes.

The STA is defined as the average absolute amplitude in a 1-s window measured on the beam with the maximum SNR and is updated every sample. As a rough approximation, the amplitude of a wavelet is the product of the amplitude spectral density and the bandwidth [*Aki and Richards, 1980; p. 492*]. Therefore, we express the STA in terms of the amplitude spectral density of the beam as

$$STA = A_B(f_0) \Delta f \delta(f_0) \quad (3.2)$$

where f_0 is the dominant signal frequency, Δf is the filter bandwidth, A_B is the amplitude spectrum of the beam, and δ is a correction term to account for dispersion and/or scattering. If all of the energy in the bandwidth Δf arrives at the same time then $\delta \approx 1$, otherwise $\delta < 1$. If the signal is purely random, then δ can be found from (3.1). The range

$$\left[\frac{2}{T \Delta f} \right]^{1/2} \leq \delta \leq 1.0 \quad (3.3)$$

where T is the noise window length (in this case, 5 s), corresponds to that between a purely random and perfectly coherent P_n signal. The lower bound on δ is 0.45, 0.31, 0.22, for 2, 4, and 8 Hz bandwidths, respectively. Figure 3.5 plots examples of the STA corrected for the bandwidth and δ , superimposed on the spectra at the frequency of the mean signal energy in the bandwidth Δf . Comparing the STAs to the beam spectra for 10 events, we find that a consistent value of $\delta = 0.7$ relates P_n temporal and spectral amplitudes on beams filtered between 2 and 5 Hz. However, between 8-16 Hz we find $\delta \approx 0.3$. This lower value is probably caused by the rapid decay of the beam spectra in this frequency band, which reduces the "effective" signal bandwidth. Increased scattering at high frequency would also have the effect of lowering δ .

Pn Beam Spectra

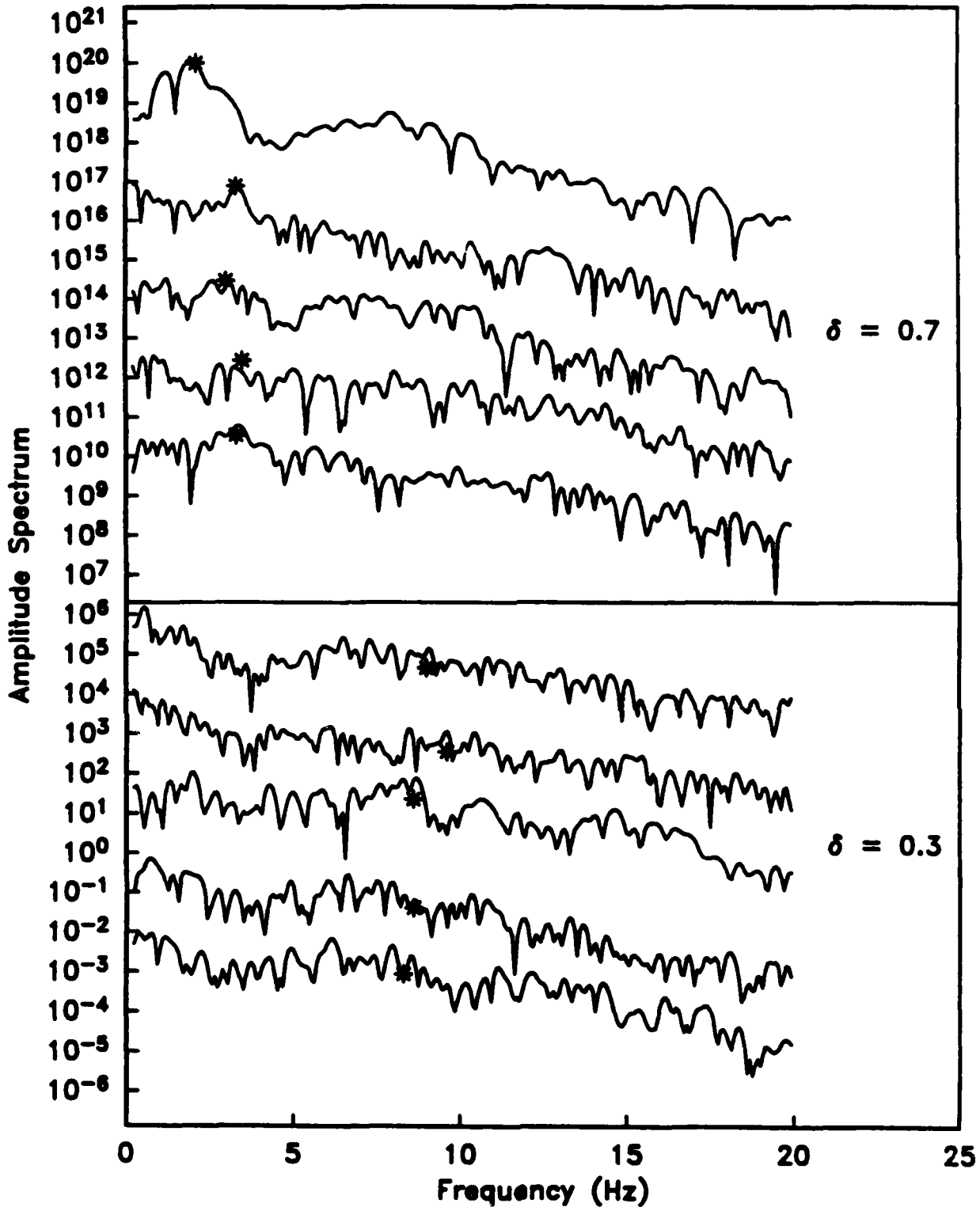


Figure 3.5. *Pn* beam spectra for 10 events recorded at NORESS. The five spectra on top are for beams filtered between approximately 2 and 5 Hz. The lower spectra are for beams filtered between 8 and 16 Hz. The asterisk on each spectrum plots $STA/(\Delta f \delta)$ where $\delta = 0.7$ between 2-5 Hz and $\delta = 0.3$ for the 8-16 Hz beam.

3.2.3 Signal-to-Noise

A major objective of this study is to predict the SNR as a function of distance, magnitude and frequency based on a parameterization of array-averaged spectra. To do this, we must address two separate issues. One is the relation between temporal and spectral amplitudes on filtered beams, and the other is the relation between beam spectra and single-channel spectra. In Sections 3.2.1 and 3.2.2 we addressed the first issue by expressing the P_n LTAs and STAs in terms of the beam spectral amplitudes. In this section we investigate the second issue which involves the determination of the frequency-dependent beam gain.

While beamforming can produce $1/N$ or greater noise suppression, it also suppresses uncorrelated high-frequency signal energy. The beam gain is defined as the ratio of the SNR on the beam and the single-channel SNR. Therefore, using (3.1) and (3.2) we can express the SNR on a filtered beam in terms of the array-averaged single-channel spectra as

$$SNR = \frac{STA}{LTA} = \frac{A(f)}{N(f)} \delta G(f) \left[\frac{T\Delta f}{2} \right]^{1/2} \quad (3.4)$$

where $A(f)$ and $N(f)$ are single-channel signal and noise spectra and $G(f)$ is the frequency-dependent beam gain. The only term in (3.4) that we have not estimated is the beam gain. From the observed SNR and our estimates of δ , we can determine the average $G(f)$ for specific beams using (3.4). Note that the signal and noise are not, in general, evaluated at the same frequency (each is evaluated at the frequency of the mean energy or power over the bandwidth Δf). Figure 3.6 plots $G(f)$ for the four combinations of sub-array and filter bandwidth typical for P_n detections. The mean gain for each beam type is shown as the solid horizontal line. Table 3.2 summarizes the beam gain results.

Table 3.2. Beam gain.

Sub-array	Beam Numbers	Frequency	Δf	Detections	\sqrt{N}	$\langle G \rangle$	σ	δ
A0-BCD	3,8-16	2.0-5.0	2.0	68	4.7	3.0	1.4	0.7
A0-BC	4-5	2.5-5.0	2.0	27	3.6	3.2	2.6	0.7
A0-AB	6	4.0-8.0	4.0	30	3.0	1.11	0.8	0.7
A0-AB	7	8.0-16.0	8.0	56	3.0	1.09	0.6	0.3

For beams with center frequencies below 5 Hz, the beam gain approaches \sqrt{N} , although there is much scatter. The noise suppression is much more consistent about \sqrt{N} . The large scatter in Figure 3.6 is due to variability in signal coherence. However, the gains at higher frequency are near unity. That is, the array offers little or no advantage over single channels. This is consistent with regional beam gain spectra displayed by *Mykkeltveit et al.* [1985]. Since the gains listed in Table 3.2 depend on our value of δ , this consistency provides

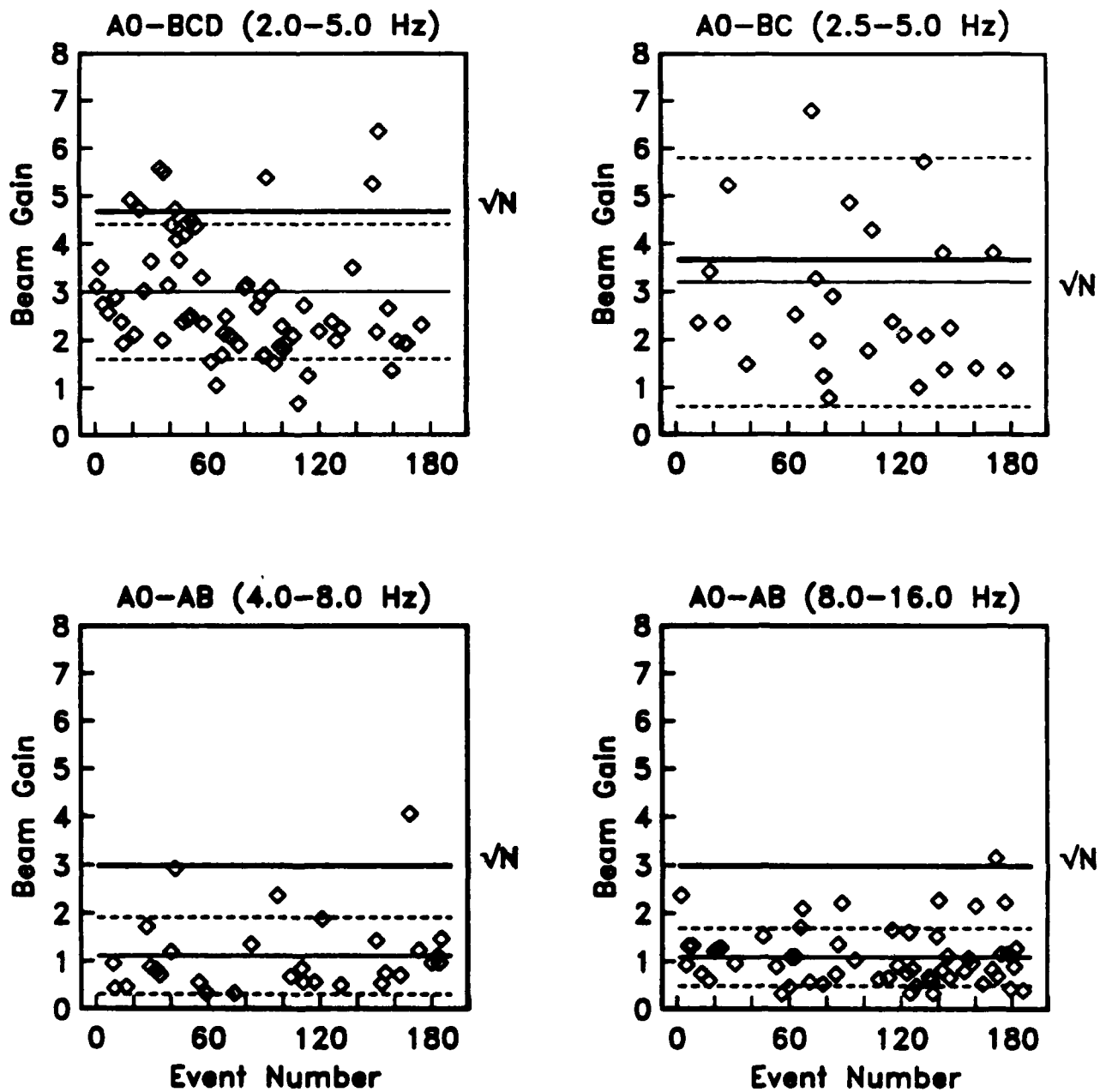


Figure 3.6. Beam gain calculated using (3.4) for the four combinations of sub-array and frequency filter typical for P_n detection. The means are plotted bounded by one standard deviation. A bold line at \sqrt{N} is plotted for reference. Note that the same axes scaling is used for all plots and that not all of the points used to determine the mean and standard deviation are shown.

independent support for our estimate of that parameter. The NORESS array was designed to enhance signal frequencies in the range 1.5-5.0 Hz [Mykkeltveit, 1983]. Thus, it is not surprising that the array does not offer enhanced SNR at higher frequencies. This simply means that the signal and the noise are both uncorrelated over the sub-array used in beamforming. Note, however, that it is likely that the high-frequency beam gain could be improved by adding steered beams and/or by filtering over a narrower frequency band. This is discussed in Section 3.4.

3.3 Regional wave detectability

In this section we introduce an empirical parameterization of the temporal SNR that we call the "detectability," which gives the probability of detection of a given magnitude event as a function of epicentral distance. The detectability is computed directly from parameters that define the way an automatic detector works (e.g., the STA, LTA, and pre-set detector thresholds). Therefore, it is possible to very accurately simulate the detection capability of arrays equipped with automatic array-processing software. However, another question is how to extrapolate these results to areas with different attenuation. For this we use the relationship between the temporal SNR and the spectral inversion parameters derived in the previous section. To validate this procedure, we compare "predicted" (based on our inversion results) and "observed" P_n detectability at NORESS. Since we don't have a similar relationship for L_g , we simply present an empirical parameterization of NORESS L_g detectability and note that the results cannot be extrapolated with confidence to other regions.

The automatic detection of a seismic signal occurs when the STA/LTA exceeds a predetermined threshold. Therefore, dividing by the threshold provides a common basis for comparing the SNR measured on different beams [Kvaerna *et al.*, 1987a]. Since the beam thresholds are determined from false alarm statistics, this means that the probability of a spurious detection is the same on all beams. We define the detectability, $D(\Delta)$, as

$$D(\Delta) = \log \left[\frac{\text{SNR}}{th} \right] - \alpha M_L \quad (3.5)$$

where SNR is the maximum STA/LTA on all detecting beams, th is the beam threshold, and α is chosen such that $D(\Delta)$ does not depend on the source. The value of α is close to one for P_n but much less than one for L_g because both the STA and the LTA depend on M_L . An important aspect of the detectability is that it includes frequency dependence. For example, events within 400-500 km of NORESS typically have the maximum SNR for P_n on a high-frequency beam, while more distant events are usually detected with the maximum SNR on a lower frequency beam (Figure 3.2). The detectability can be interpreted simply in terms of the magnitude detection threshold. For example, when the SNR is equal to the beam threshold, $-D(\Delta)$ is equal to α multiplied by the 50% NORESS M_L detection threshold. Assuming that both signal

and noise are log normally distributed, the probability of detecting wave k from source j is

$$P_{jk} = \Phi \left[\frac{D_k(r_j) + \alpha_k M_{Lj}}{\sigma_k} \right] \quad (3.6)$$

where $\Phi(x)$ is the Gaussian cumulative distribution function [e.g., *Abramowitz and Stegun*, 1964; p. 931] and σ_k is the standard deviation of the detectability function. This relationship is a valid representation of the probability of detection below the source corner frequency.

3.3.1 P_n Detectability

Figure 3.7 plots the temporal P_n detectability defined by (3.5) with $\alpha = 1.0$. Only explosions are used because the earthquake detectability can be biased by the unknown radiation pattern. That is, it is not possible to determine an α for earthquakes that effectively removes the source contribution to the SNR. We also excluded events with $M_L \geq 3.0$ that were detected on one of the two highest-frequency beams because their corner frequencies are expected to be within the filter bandwidth. The logarithmic decay of the P_n detectability is approximated by $D(\Delta) = -0.53 - 1.93 \log \Delta$, where Δ is epicentral distance in degrees and the coefficients were obtained by least-squares. This is plotted in Figure 3.7 bounded by one standard deviation ($\sigma = 0.31$). Based on this parameterization, the 50% NORESS M_L threshold for detecting P_n at 400 km is about 1.6 and at 1000 km is about 2.4.

In order to validate the relationship between the temporal and spectral SNR derived in the previous section, we compare the predicted (based on the spectral inversion results) and observed NORESS P_n detectability. We use our parameterization of the single-channel spectrum $A(f)$, and the average NORESS noise spectrum $N(f)$ (Figure 2.4), to predict the detection capability of specific beams using (3.4). We use \sqrt{N} gain for beams with frequency filters between 2-5 Hz and a gain of 1.0 for the two highest frequency beams. We set $\alpha = 1.35$, which is the slope of the $\log M_0 - M_L$ relation for explosions (Figure 2.2). Note that the difference between the implied 50% NORESS M_L threshold for $\alpha = 1.35$ and $\alpha = 1.0$ is only about 0.1. Figure 3.8 demonstrates the general consistency between the predicted and observed P_n detectability.

Although the frequency of the maximum SNR predicted from the spectral inversion is greater than 10 Hz for distances less than 800 km (Figure 2.4a), the predicted frequency of optimal detectability is much less than this. This is because the single-channel SNR advantage at high frequency is erased by a lower beam gain. As a result, our model predicts greater detection capability on 2.5-5 Hz beams than on the higher-frequency beams for ranges greater than about 200 km. However, the observations show a significant number of P_n detections on the higher-frequency beams at longer ranges, even though their SNRs are consistent with the model. A likely explanation is that spectral modulation caused by ripple-firing with delays between 150-250 ms consistently suppresses amplitudes less than 4-5 Hz for mine blasts [*Baumgardt and Zeigler*, 1987]. In many cases our Q model correctly predicts the high frequency (> 5 Hz) P_n amplitude of these events, but overestimates the spectral level between 2-5 Hz [*Sereno and Bratt*, 1988]. Since the time lags that produce 4-5 Hz spectral modulations are

Pn Detectability ($\alpha = 1.0$)

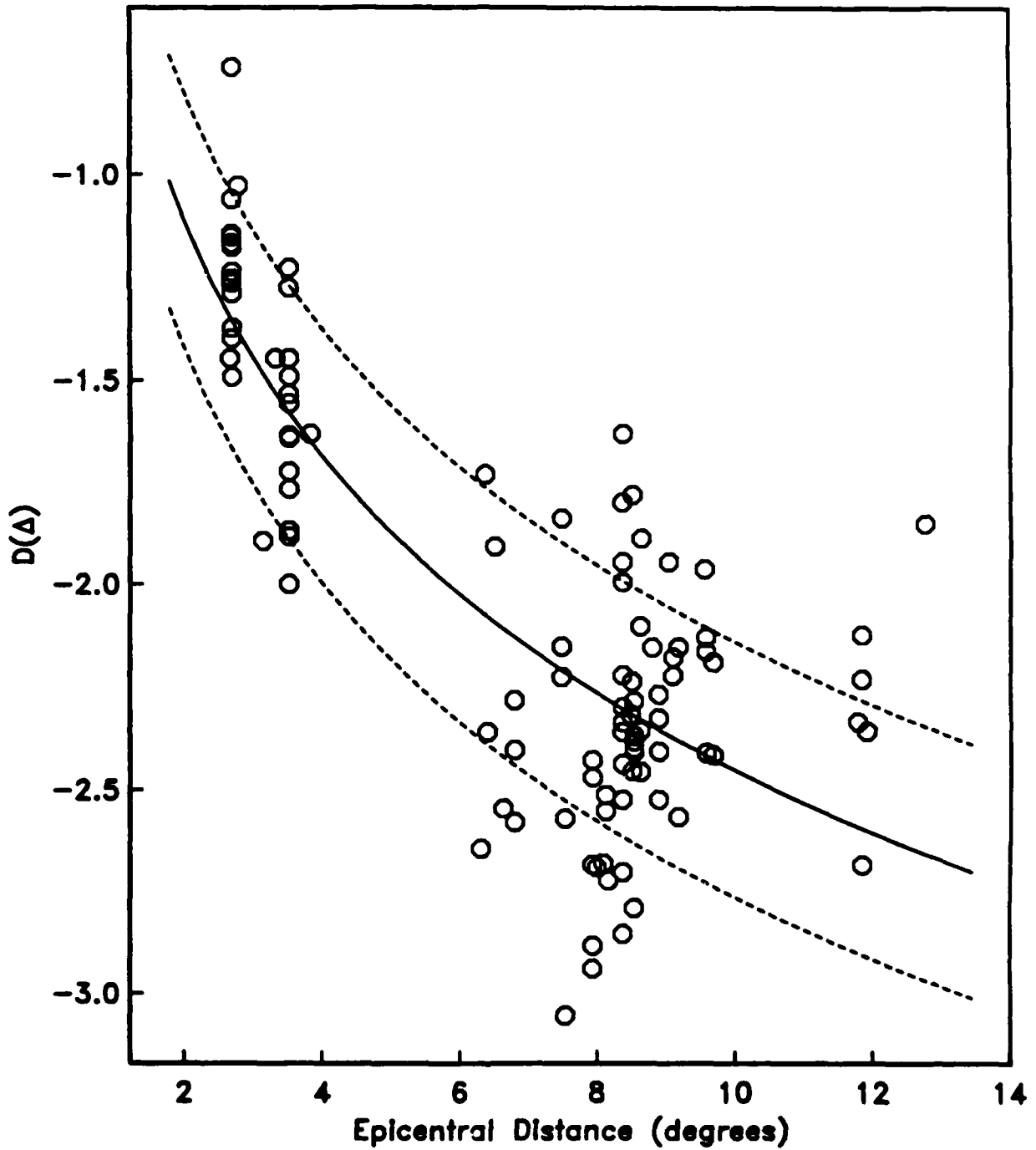


Figure 3.7. *Pn* detectability defined by (3.5) with $\alpha = 1.0$ for 102 explosions. Seven events were excluded with $M_L \geq 3.0$ because their corner frequencies are expected to be within the filter bandwidth. The curve is the logarithmic parameterization of $D(\Delta)$ bounded by one standard deviation.

Pn Detectability ($\alpha = 1.35$)

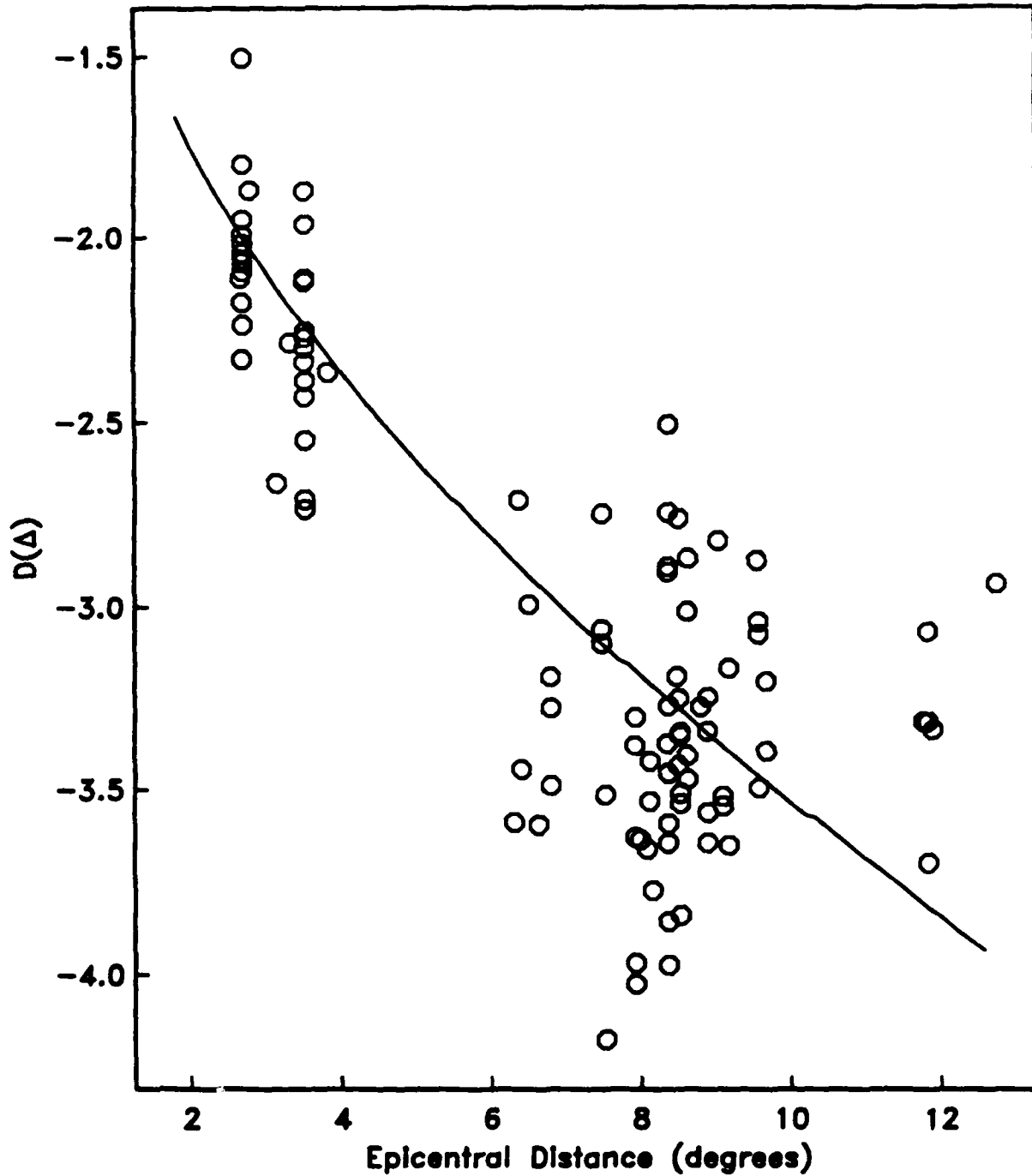


Figure 3.8. Comparison of predicted (based on our spectral inversion) and observed P_n detectability defined by (3.5) with $\alpha = 1.35$. This value of α is based on the observed rate of increase of explosion moment with M_L (see Figure 2.2).

consistent with the destructive interference of multiple explosions, we interpret this as an unmodeled source complexity rather than a path effect.

3.3.2 *Lg* Detectability

In this section we present the results of an empirical parameterization of NORESS *Lg* detectability. However, without a parameterization of the pre-*Lg* noise spectrum (like Figure 3.3 for *Pn*), we cannot predict the *Lg* detectability based on *Q* and moment. Therefore, while our results accurately represent *Lg* detectability at NORESS, they cannot be extrapolated with confidence to other regions. The value of α in (3.5) that effectively removes the source contribution to the detectability is equal to the difference in slopes of the log moment-magnitude (~ 1.0) and log LTA-magnitude relations (~ 0.8). Therefore we expect the appropriate value of α to be close to 0.2. If the source contribution is effectively removed, the detectability should not depend on magnitude, provided the measurements are taken below the corner frequency. We find that subtracting values much greater than $0.2 M_L$ produces an obvious magnitude dependence in the *Lg* detectability, indicating that the source contribution to the SNR was not adequately removed [Serenio and Bratt, 1988]. Figure 3.9 plots the observed *Lg* detectability defined by (3.5) with $\alpha = 0.2$. We include both earthquakes and explosions since *Lg* is relatively insensitive to the source radiation pattern. The logarithmic decay of the *Lg* detectability with $\alpha = 0.2$ is approximated by $D(\Delta) = -0.11 - 0.64 \log \Delta$, where the coefficients were obtained by least-squares. This is plotted in Figure 3.9 bounded by one standard deviation ($\sigma = 0.12$). From this parameterization, the 50% NORESS M_L threshold for detecting *Lg* is about 1.2 at 400 km and about 2.5 at 1000 km.

3.4 Detection capability of the NORESS array

In this section we estimate the detection capability of NORESS using our parameterization. These estimates are compared to the results of a NORSAR study that estimated detection capability by comparing the NORESS detections to bulletins produced by local seismic networks in Fennoscandia.

It is straightforward to use our parameterization of $D(\Delta)$ to estimate the detection capability of the NORESS array. We use (3.6) together with the detectability to calculate the probability of detecting a given magnitude event as a function of epicentral distance. For example, the 90% NORESS M_L detection threshold for *Pn* based on $D(\Delta)$ with $\alpha = 1.0$ is 2.0 at 400 km and 2.8 at 1000 km. For *Lg* the 90% detection threshold with $\alpha = 0.2$ is 2.0 at 400 km and 3.3 at 1000 km. The 90% thresholds for detection of either *Pn* or *Lg* are 1.7 at 400 km and 2.6 at 1000 km. These estimates are generally consistent with those of Ringdal [1986] who estimated the 90% M_L threshold for detecting *P* phases between 700 and 1400 km (average about 960 km) to be 2.7 and for detecting *P* or secondary phases in the same distance range to be 2.5. We have not studied the detectability of *Sn*, so we cannot directly compare our secondary phase results to his. Since the addition of *Sn* can only improve the detectability, our results for *Pn* or *Lg* detection give an upper bound. Table 3.3 compares the results of the two studies.

Lg Detectability ($\alpha = 0.2$)

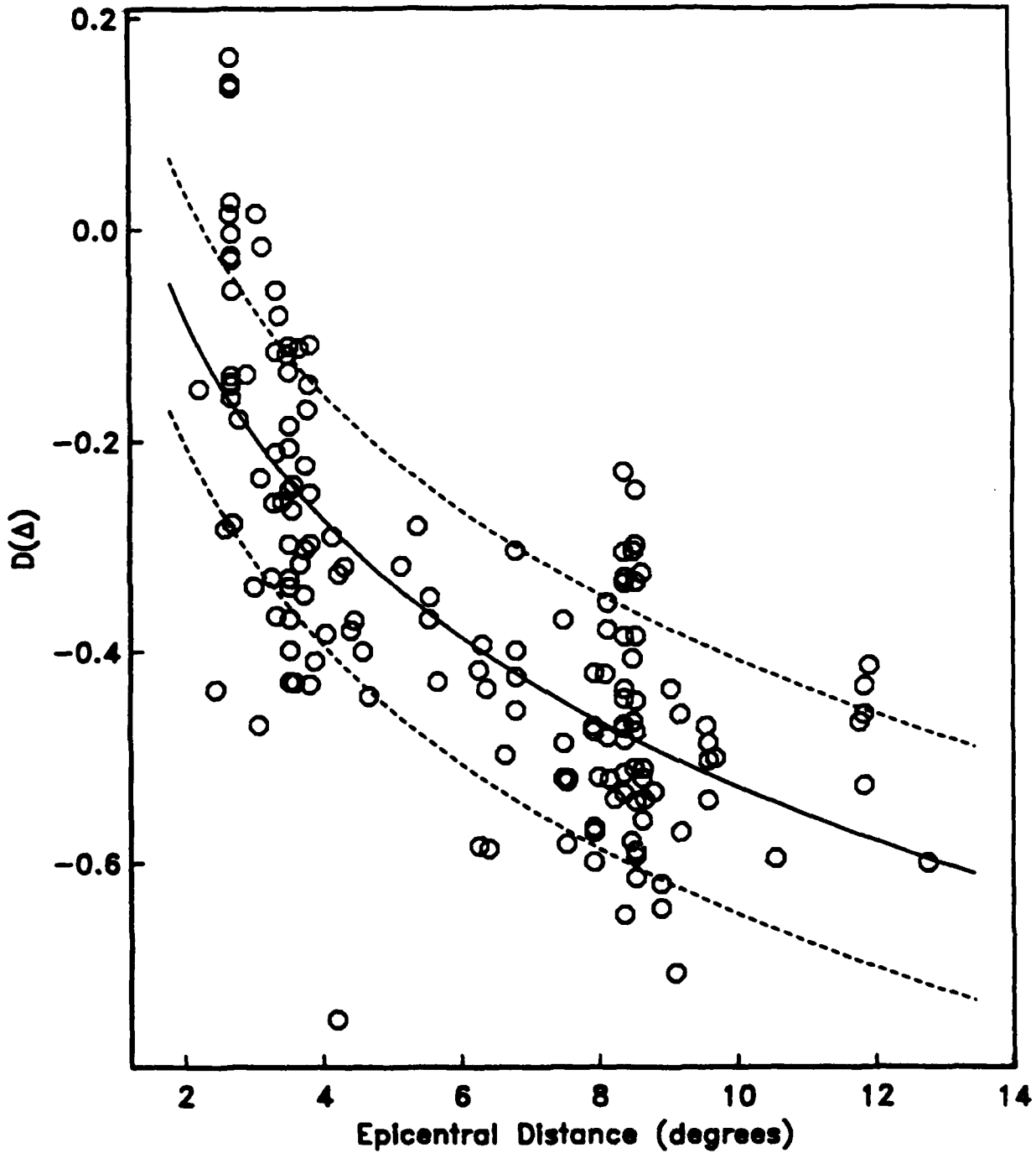


Figure 3.9. L_g detectability defined by (3.5) with $\alpha = 0.2$ for 157 events. Events were excluded only if a NORESS M_L was not available. Both earthquakes and explosions are included. The curve is the logarithmic parameterization of $D(\Delta)$ bounded by one standard deviation.

Table 3.3. Regional wave detection capability at NORESS.

Phase	50% Threshold		90% Threshold	
	this study	<i>Ringdal</i> [1986]	this study	<i>Ringdal</i> [1986]
<i>P</i> only	2.4	2.3	2.8	2.7
<i>Lg</i> only	2.5	---	3.3	---
<i>P</i> or Secondary Phases	2.2†	1.9	2.6†	2.5

† This study uses *Lg* as the only secondary phase, *Ringdal* [1986] used *Sn* or *Lg*.

In Figure 3.10 the detection capability estimates based on our temporal parameterization are compared to those based on the spectral inversion. The dashed curves are our estimates of the 90% NORESS M_L thresholds for detecting *Pn* and for detecting *Pn* or *Lg*, based on the temporal detectability curves in Figures 3.7 and 3.9. The solid curve is the 90% M_L threshold for detecting *Pn* based on the detectability predicted by the spectral inversion results (Figure 3.8). Also indicated in Figure 3.10 are the results of *Ringdal* [1986]. In general, these three independent studies produce consistent estimates of the regional wave detection capability of the NORESS array.

Note that our estimates of the detection capability of the NORESS array are based on the standard beam set listed in Table 3.1. However, it is possible that NORESS capability could be enhanced by including more steered beams [T. Kvaerna, personal communication, 1988], or by modifying the frequency filters [*Kvaerna et al.*, 1987b; *Sereno and Bratt*, 1988]. For example, the predicted *Pn* spectrum at ranges less than 500 km decays less rapidly than the noise spectrum beyond 8 Hz (Figure 2.4). This suggests that the *Pn* detection capability of the 8-16 Hz beam (beam 7, Table 3.1) could be improved by filtering at higher frequency. This is confirmed by *Kvaerna et al.* [1987b] who compiled detection statistics for events in western Norway. Most of their events were at ranges less than 450 km. They found that 60% of their *Pn* detections occurred with the maximum SNR on a 10-16 Hz beam while only 4% occurred on the 8-16 Hz beam. Therefore, our results may underestimate the detection capability of a NORESS-type array with an improved beam deployment.

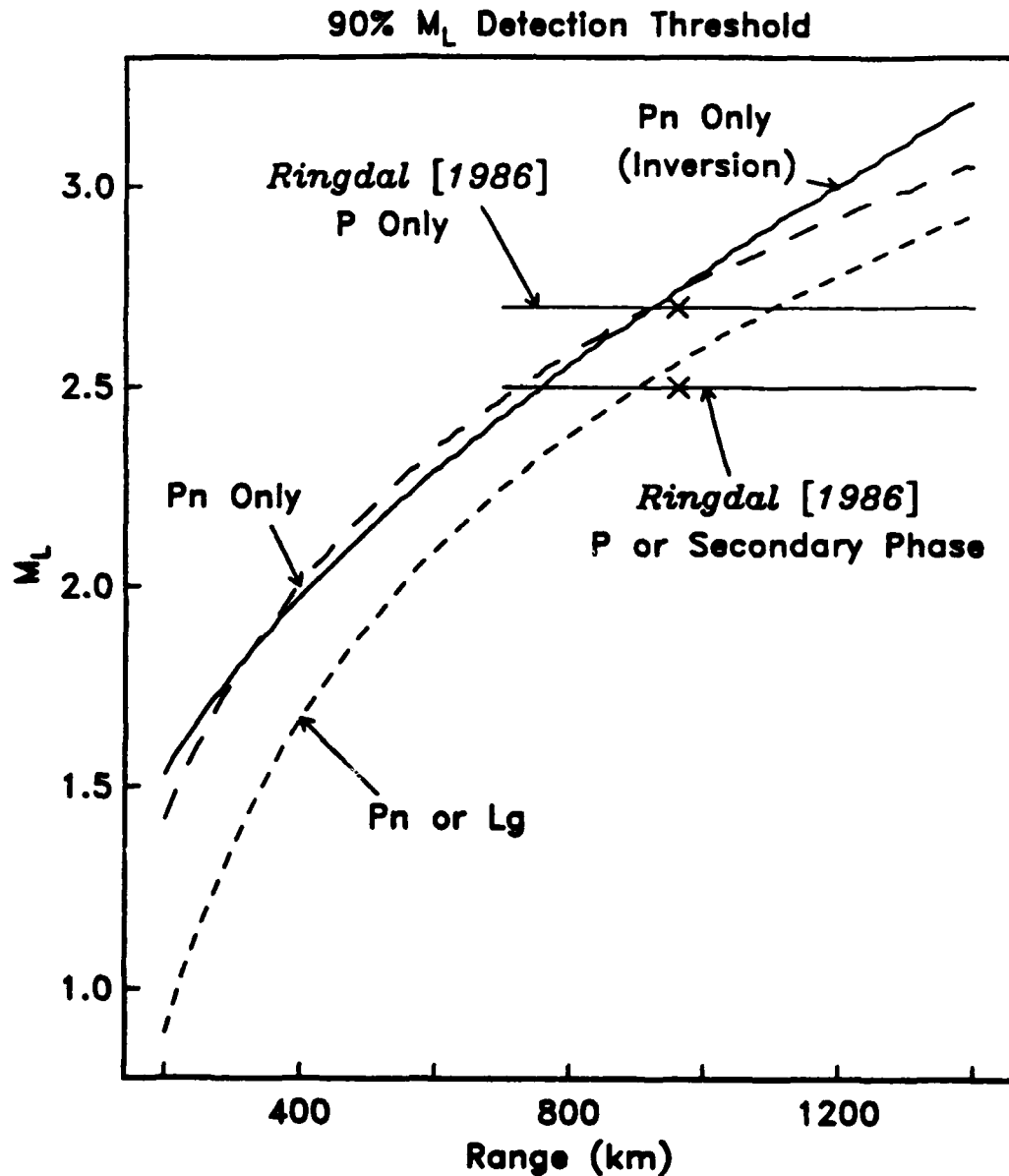


Figure 3.10. Estimates of 90% M_L detection thresholds at NORESS as a function of epicentral distance. The dashed curves are based on a parameterization of observed temporal amplitudes. Curves for detecting Pn and for detecting either Pn or Lg are plotted. The solid curve is based on the results of our inversion of Pn spectra. The horizontal bars are detection thresholds at NORESS as determined by comparing NORESS detections to bulletins produced by local seismic networks [Ringdal, 1986]. Events for this study were at ranges between 700 and 1400 and the average distance was about 960 km (X).

4. DETECTION CAPABILITY SIMULATION

In this section we present simulations of the detection capability of hypothetical networks in the Soviet Union. These simulations are normalized by the NORESS results presented in previous sections. Our parameterization of NORESS detection capability in terms of the noise, attenuation, and signal processing characteristics allows us to predict detection capability of a NORESS-type array for other regions with different conditions. Of course, the validity of these predictions depends on the accuracy of the attenuation and noise estimates for areas of interest. Since these are not available for the Soviet Union, we assume a range of conditions and determine the sensitivity of our results to these assumptions.

The network detection capability simulations presented in this section were computed using an extended version of *Seismic Network Assessment Program for Detection* [SNAP/D, Ciervo et al., 1985] called SNAP/DX [Bratt et al., 1987]. The program first calculates the probability that a seismic phase will be detected at a single station using (3.6). Next, the network detection thresholds are determined from the detection probabilities of individual stations. The threshold for each epicenter in the grid is determined by varying the magnitude until the detection probability equals the desired confidence level.

4.1 Extrapolation of NORESS capability

Simulations of the detection capability of a hypothetical network of seismic stations in the Soviet Union, require assumptions about the signal and noise characteristics in that region. The simplest assumption is to use our results from NORESS for all stations. That is, we assume that all aspects of regional wave propagation (signal and noise) at all stations are identical to what we observe at NORESS. Even here we require some extrapolation since our NORESS results are strictly valid only to about 12° . To estimate detectability at longer ranges, we compared the Preliminary Determination of Epicenters (PDE) bulletin to detections at NORESS. Based on observed arrival time, azimuth and phase velocity; *P*-wave detections at NORESS were found for nine events listed in the PDE bulletin at distances greater than 12° . Table 4.1 lists the PDE locations and magnitudes of these events. Also listed are the predominant signal frequencies determined by SAIAP. Figure 4.1 displays the $D(\Delta)$ calculated for these events using (3.5) with $\alpha = 1.0$. These events are considerably larger than those used in our regional study, and it is possible that the source corner frequency could bias the detectability estimate. Therefore, we assume corner frequency scales inversely with the cube root of the moment, and that it equals 10 Hz for a magnitude 3.0 event (based on our inversion results), to get a rough estimate of the source corner frequencies. An ω -square source model was used to correct the amplitudes for the predicted source corner frequency effect. The results are indicated by vertical bars on $D(\Delta)$ in Figure 4.1. The source-corrected $D(\Delta)$ were parameterized by a logarithmic decay and the coefficients were determined by least-squares. The resulting teleseismic *P*-wave detectability, $D(\Delta) = -0.69 - 1.82 \log \Delta$, is plotted as a solid line in Figure 4.1. Shown for comparison is the 1-Hz amplitude-distance curve derived by Veith and Clawson [1972], normalized by the average 1-Hz NORESS noise (3.1 nm-s), \sqrt{N} beam gain, and the filter bandwidth and detector threshold used for the NORESS 1-3 Hz beam. Note that since the predominant frequency generally decreases with increasing epicentral distance, the detectability cannot be simulated with the amplitude-distance curve at a single frequency. Our curve

Table 4.1. Events used to estimate teleseismic detectability

Event	Date	Time	Location	Depth	Range	m_b	Frequency
1	7-18-85	21:15	65.97N 40.85E	0.0	14.0	5.0	2.2
2	11-23-85	20:14	42.31N 19.88E	9.0	19.1	3.4	2.5
3	8- 1-86	13:57	73.04N 55.57E	33.0	20.5	4.6	2.5
4	7-25-85	3:11	49.89N 78.15E	0.0	37.6	5.0	2.2
5	2-17-86	12:36	36.66N 71.17E	33.0	44.0	5.0	3.1
6	10-27-86	14:12	7.49N 36.60W	10.0	64.1	5.2	1.1
7	11-15-85	11:56	44.15N 148.29E	33.0	69.4	5.2	3.5
8	10-27-86	12:16	42.74N 145.55E	33.0	70.0	4.9	3.6
9	8-13-86	15:27	7.69N 74.71W	60.0	81.5	5.0	1.5

Teleseismic P-Wave Detectability

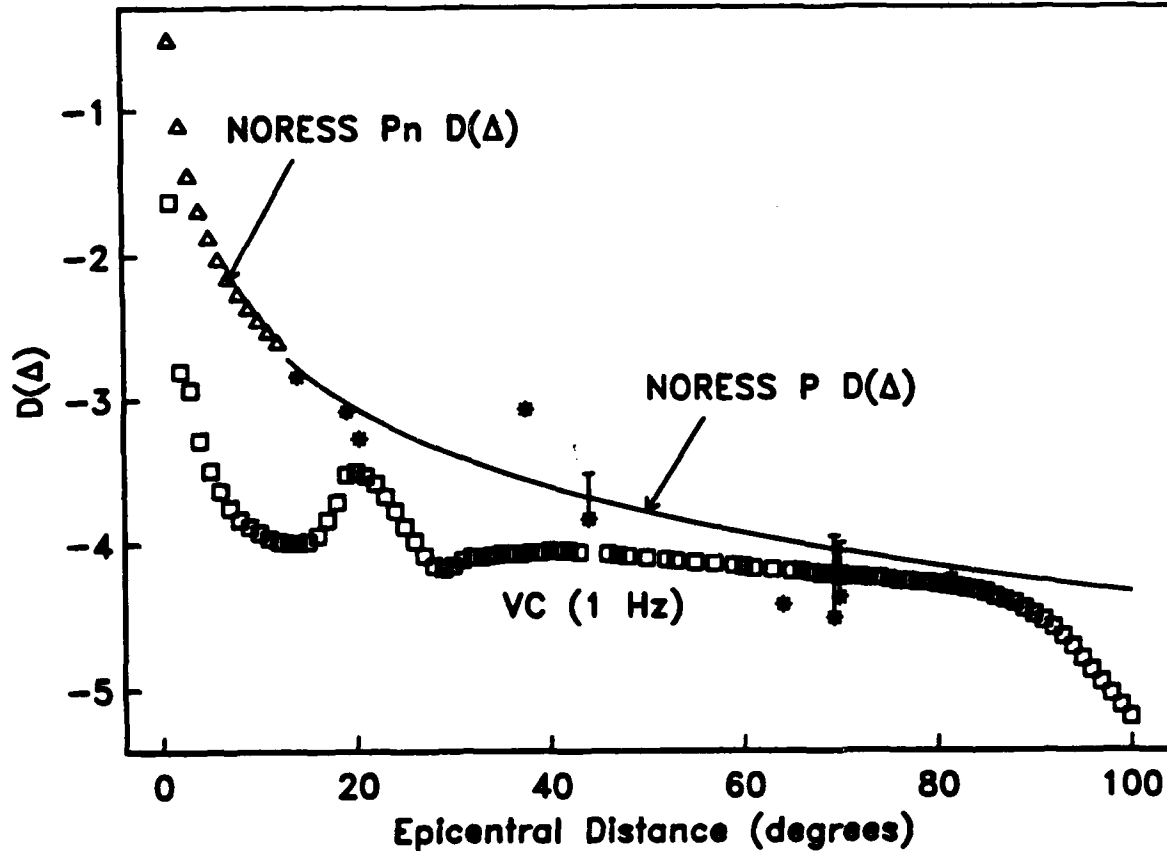


Figure 4.1. Teleseismic P -wave detectability. The asterisks are the $D(\Delta)$ computed using (3.5) with $\alpha = 1.0$ for the nine events listed in Table 4.1. The solid bars indicate the shift in $D(\Delta)$ after correcting for the expected source corner frequency. The solid curve is the logarithmic parameterization of the source-corrected $D(\Delta)$. The triangles indicate our parameterization of the NORESS regional P_n detectability shown in Figure 3.7. The squares indicate 1-Hz detectability, based on the amplitude-distance curve of Veith and Clawson [1972], NORESS 1-Hz noise, a 2 Hz filter bandwidth, and \sqrt{N} beam gain.

indicates larger amplitudes (or greater detection capability) than the *Veith and Clawson* [1972] curve at distances less than about 40° , because at these distances the maximum SNR is at frequencies greater than 1 Hz. We simply plot the *Veith and Clawson* [1972] curve to demonstrate that our *P*-wave detectability estimates are generally consistent with those inferred from the *Veith and Clawson* curve at longer ranges, where the dominant signal frequency is expected to be closer to 1 Hz. We use this parameterization to represent teleseismic *P*-wave detectability for all network capability simulations considered in this report. However, we recognize that this part of the detectability curve is more uncertain than at regional distances, so we do not consider networks for which teleseismic detection capability has a strong influence on the magnitude threshold.

We were not able to parameterize *Lg* detectability in terms of the frequency-dependent attenuation and noise at NORESS, nor have we separated the array performance from the single-channel capability. Thus, our results for *Lg* cannot be extrapolated with confidence. For this reason we only include *Lg* in simulations for networks including stations assumed to be identical to NORESS. That is, we use our logarithmic parameterization (Figure 3.9) to simulate *Lg* detectability throughout the Soviet Union, though we include *Lg* blockage by major structural boundaries.

It is important to determine the sensitivity of our detection capability estimates to our assumptions about *Q*. Very few studies of regional *Pn* attenuation have been conducted, so it is difficult to estimate the amount of variability from region to region. However, numerous studies of *Lg* attenuation have been conducted. Typically the 1-Hz Q_{Lg} is between 800-1100 in the eastern United States and the exponent of a power-law frequency dependence is between 0.2 and 0.4 [e.g., *Singh and Herrmann*, 1983; *Hasegawa*, 1985; *Goncz et al.*, 1987; *Chun et al.*, 1987; *Gupta and McLaughlin*, 1987]. The western United States is characterized by a lower 1-Hz Q_{Lg} (140-200) and a higher frequency exponent (0.3-0.7) [e.g., *Singh and Herrmann*, 1983; *Nutli*, 1986; *Chavez and Priestley*, 1986]. Figure 4.2 plots predicted *Lg* spectra using (2.1) at 500 km for our NORESS $Q = 560f^{0.26}$, and for attenuation models representative of the eastern and western United States. Also plotted are predicted spectra for $Q = 840f^{0.26}$ and $Q = 280f^{0.26}$, which correspond to $\pm 50\%$ of the Q_{Lg} that we determined for NORESS. Note that this range in *Q* approximately corresponds to the difference between spectra recorded in the eastern and western United States. The attenuation we observe at NORESS is closer to attenuation observed in the eastern United States.

Since $\pm 50\%$ of our NORESS *Q* seems to encompass the range of Q_{Lg} , we use the same range of models for Q_{Pn} to determine the sensitivity of our network simulations to that parameter. Figure 4.3 plots predicted *Pn* spectra at 500 km for our NORESS $Q = 325f^{0.48}$, and for *Q* equal to $\pm 50\%$ of that value. While there is no guarantee that this range is representative of the variability of *Pn* attenuation, we note that the spectral shapes are quite dissimilar and imply very different conclusions about the high-frequency detection capability.

We use the NORESS noise spectrum for all network detection capability simulations presented in this report. It is trivial to determine the change in the detection capability that would result from a shift in the absolute level of the noise spectrum. Although noise estimates are not available for most of the Soviet Union, *Berger et al.* [1988] determined average noise levels recorded by three seismic stations in the vicinity of the principal underground nuclear

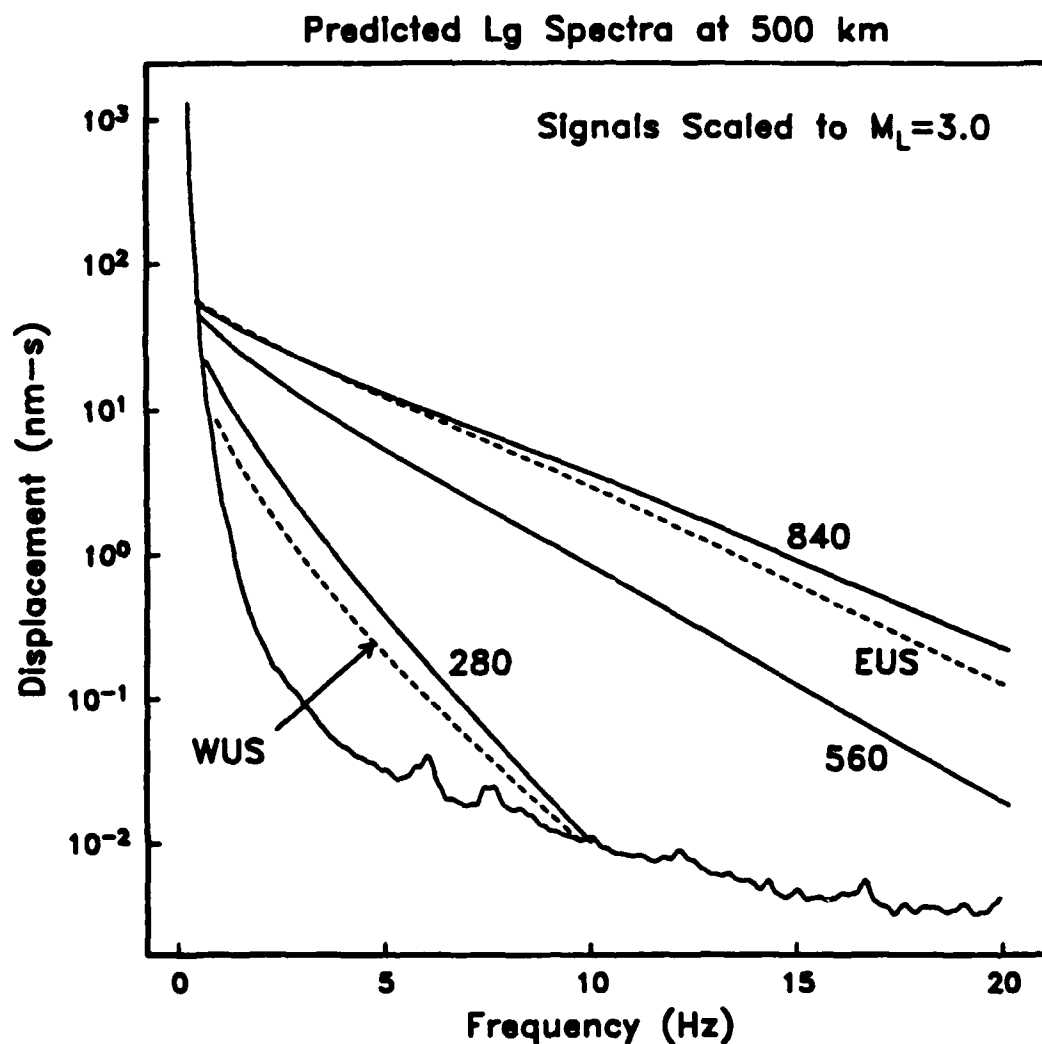


Figure 4.2. Predicted L_g spectra for a magnitude 3.0 event at 500 km for various Q models. The solid curves are for $Q(f) = Q_0 f^{0.26}$ and are labeled by Q_0 . The spectrum for $Q_0 = 560$ is based on our inversion of NORESS data. The other two solid curves indicate the predicted spectra if Q_{Lg} is 50% greater or less than our estimate for Scandinavia. The dashed curves are predicted spectra for Q estimates typical for the eastern United States (EUS) [Hasegawa, 1985] and for the western United States estimates (WUS) [Singh and Herrmann, 1983]. Specifically, we use $Q(f) = 900f^{0.2}$ for the EUS and $Q(f) = 200f^{0.4}$ for the WUS. The bottom curve is the average ambient NORESS noise spectrum.

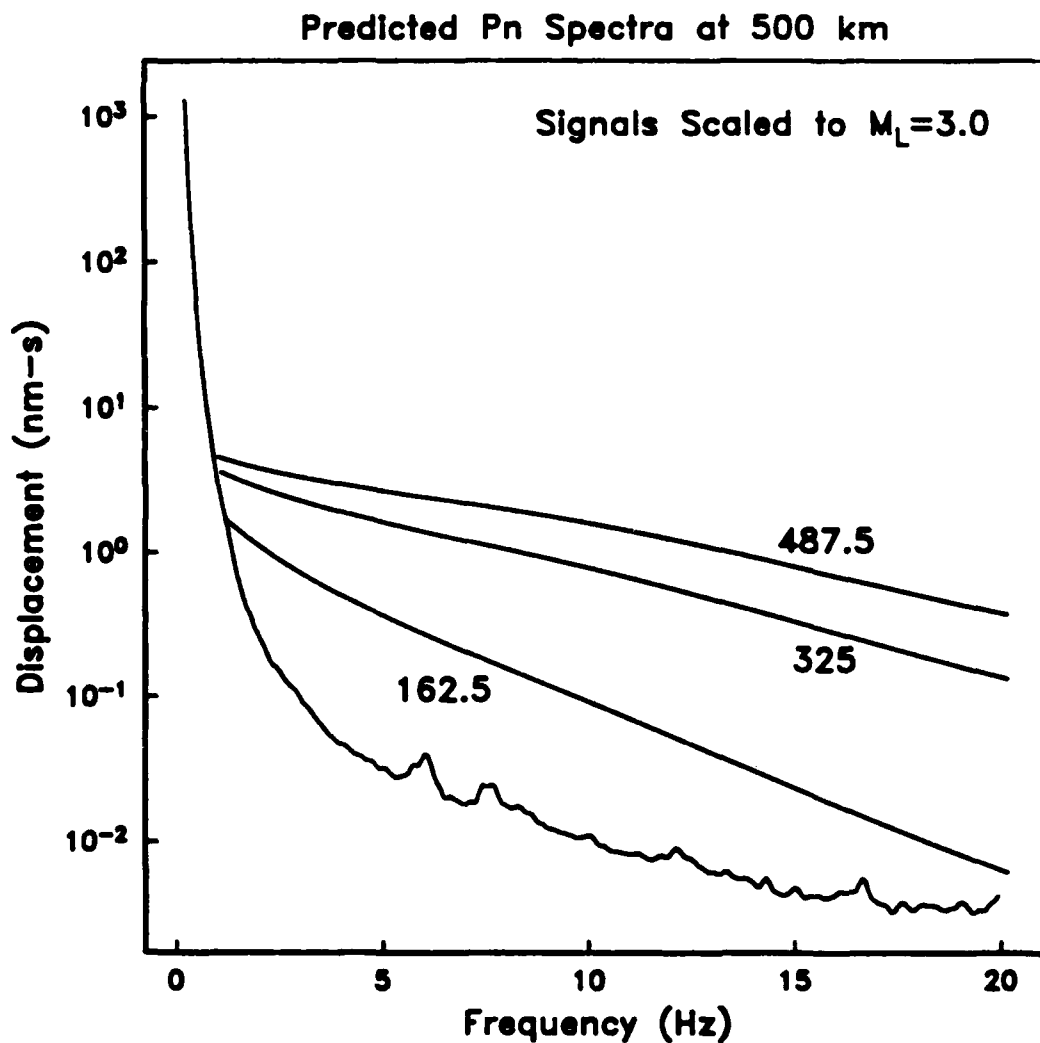


Figure 4.3. Predicted P_n spectra for a magnitude 3.0 event at 500 km for three Q models. The spectra are computed for $Q(f) = Q_0 f^{0.48}$ and are labeled by Q_0 . The spectrum for $Q_0 = 325$ is based on our inversion of NORESS data. The other two curves indicate the predicted spectra if Q_{P_n} is 50% greater or less than our estimate for Scandinavia. The bottom curve is the average ambient NORESS noise spectrum.

test site in East Kazakh. They found that the noise levels at these sites are roughly equivalent to those observed at RSTN (Regional Seismic Test Network) stations between 1 and 20 Hz, and 10 to 20 dB higher than observed at Lajitas, Texas. *Suteau-Henson and Bache* [1988] found that NORESS noise levels between 1 and 20 Hz are about 10-15 dB higher than those at Lajitas. Therefore, the NORESS noise levels in the 1-20 Hz band are similar to those observed in East Kazakh.

It is also of interest to determine the extent to which our simulations depend on the specific characteristics of the NORESS signal processing. For the standard beam set used at NORESS, we find that the array offers little advantage over single stations at high frequency. However, it appears that the NORESS high-frequency beam gain could be improved simply by adding more beams [T. Kvaerna, personal communication, 1988]. Therefore, we simulate the detection capability assuming \sqrt{N} beam gain at all frequencies for all stations, and compare to simulations normalized by the observed frequency-dependent beam gain at NORESS. We also simulate the detection capability of a network composed of only single stations (gain = 1). These two extremes bound the network capability for any combination of arrays and single stations. We also note that some improvement in detection capability may be possible by lowering the beam thresholds, albeit at a cost of increased false alarms to be recognized by the processing system [Kvaerna *et al.*, 1987a].

Finally, the magnitudes (M_L) used in our regional wave detectability study are based on Lg amplitude, and there is no accurate scaling of these M_L to the global m_b scale. That is, we present the results of the simulations in this report in terms of NORESS M_L thresholds, and these may not represent the m_b thresholds.

4.2 Detection capability in the Soviet Union

This section presents simulations of the detection capability of a hypothetical network of seismic stations/arrays in the Soviet Union for various assumptions about the characteristics of regional wave propagation in the USSR. The range of assumed attenuation models and station capability is based on our experience with the NORESS array.

An event detection requires detection of at least the minimum number of phases necessary to locate the event. For regional monitoring using arrays and three component instruments, it is possible to estimate both azimuth and arrival time of detected phases. The determination of epicenter and origin time require arrival time and azimuth information from at least two phases. Depth estimation is poorly constrained by arrival time data for crustal events at regional distances. Well-constrained depth estimates require the detection of depth phases, but this is difficult to represent in the simulations. Thus, in all examples to be presented, we require that at least three phases (arrival times and azimuths) are detected by the hypothetical network.

We use a network consisting of 13 stations external to the Soviet Union (sited at the location of existing stations) and 20 equally spaced stations internal to the Soviet Union for all of our detection capability simulations (Figure 4.4). The inter-station spacing for the internal network is approximately 1000 km. *Bratt et al.* [1987] show that for this network, the location uncertainty for events near the network threshold for 3 detections is about 10-15 km (this uncertainty can often be reduced with master event location techniques).

With this many internal stations, the detection capability is only weakly dependent upon our estimates of teleseismic *P*-wave detectability. For example, simulations that eliminate all detections beyond 12° produce 90% M_L thresholds that differ by less than 0.1 from those obtained when detections are allowed to teleseismic ranges.

Table 4.2 lists the parameters and summarizes the results of the simulations presented in this report. Simulations 1-4 are normalized by our temporal parameterization of detectability (Figures 3.7 and 3.9). These simulations assume that the signal and noise characteristics in the USSR are identical to those at NORESS, and that each station is a NORESS-type array with the standard beam set listed in Table 3.1. Figure 4.5 plots the 50% and 90% M_L thresholds for detecting three *Pn* phases. The 90% M_L threshold is between 2.4 and 2.7 for events in the Soviet Union. The 50% threshold is between 2.2 and 2.5. Figure 4.6 plots the 50% and 90% M_L thresholds for detecting three *P* or *Lg* phases for the same network. The 90% M_L threshold is between 2.1 and 2.6 for events in the Soviet Union. The 50% threshold is between 1.8 and 2.3. Since we cannot extrapolate *Lg* detectability to regions with different attenuation, we do not include *Lg* in the detection criteria for the remaining simulations. We simply note that based on NORESS observations, we expect the M_L threshold to be 0.2 to 0.3 lower for this network if *Lg* is included.

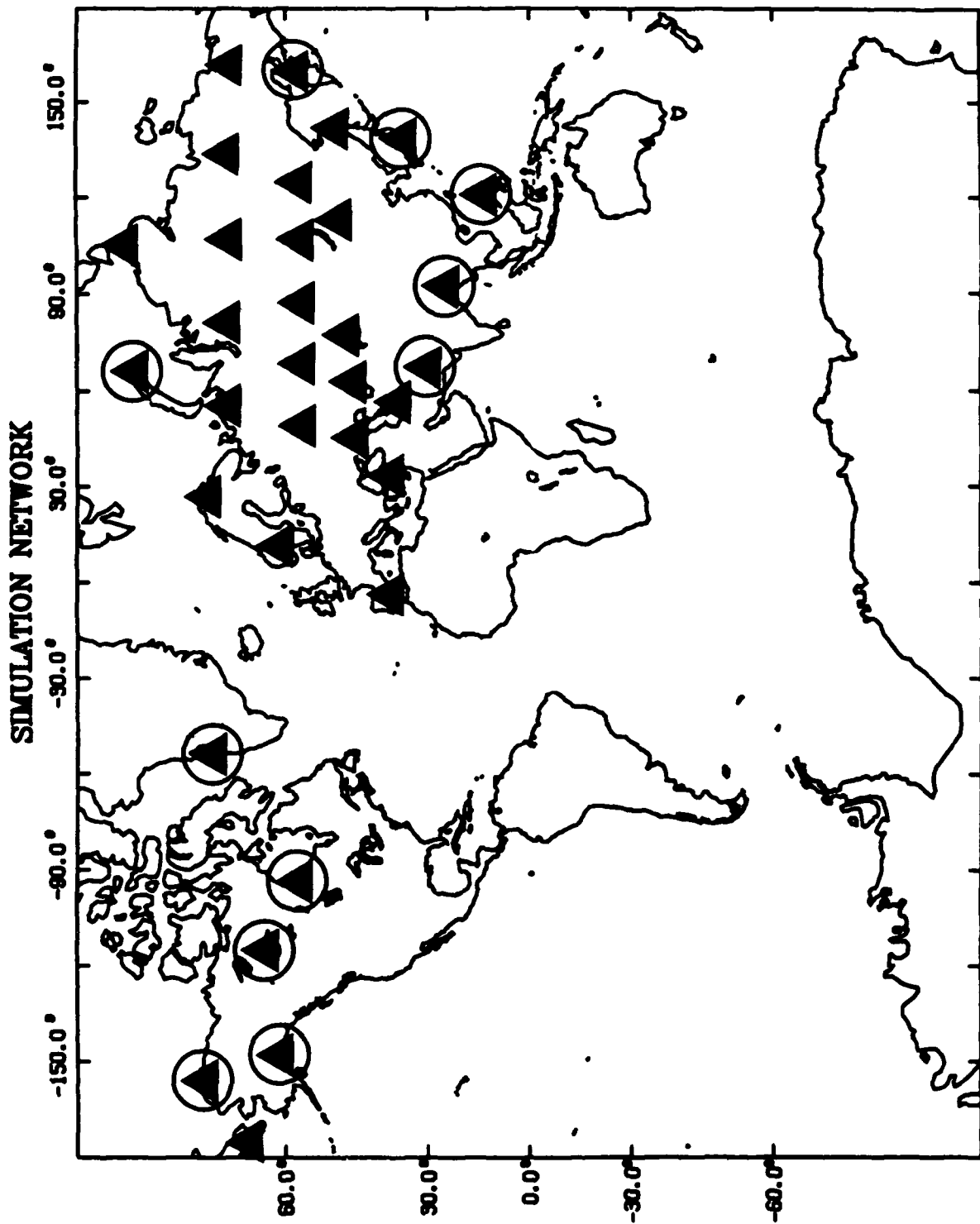


Figure 4.4. Location of seismic stations comprising the hypothetical network used in our detection capability simulations. Open circles denote sites to which L_g propagation from the USSR is prohibited.

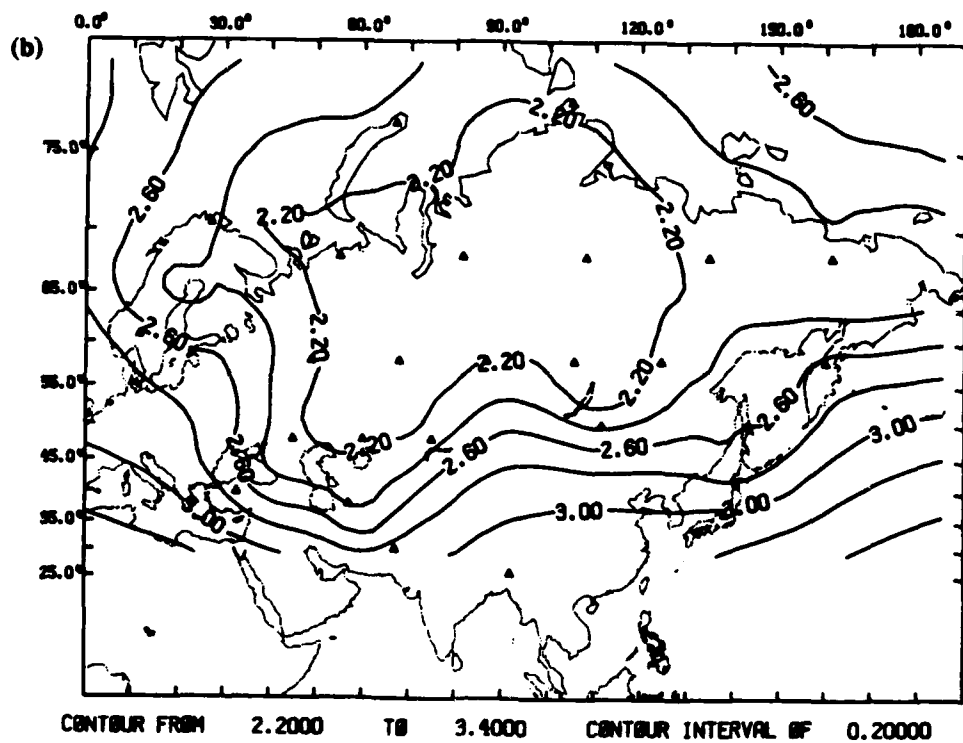
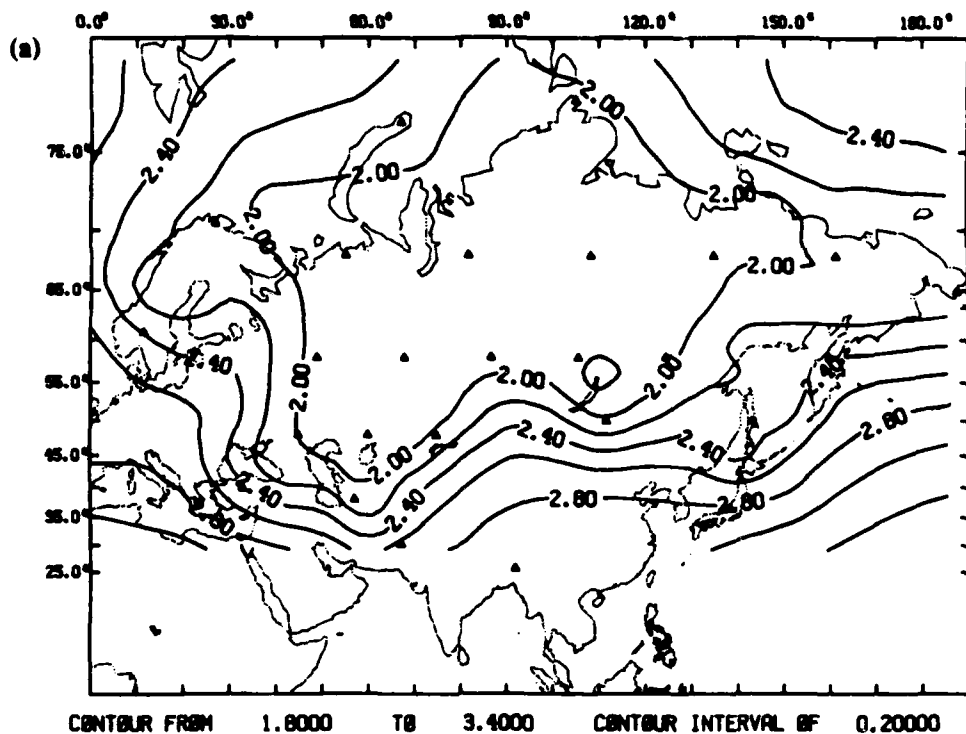


Figure 4.6. Contours of the (a) 50% and (b) 90% M_L threshold for the detection of 3 P_n or L_g phases for a network of NORESS-type arrays; 13 external to the Soviet Union and 20 internal. It is assumed that attenuation, noise, and array performance are all identical to that observed at NORESS. The normalization is based on our temporal parameterization of P_n and L_g detectability.

Table 4.2. Simulations

Simulation Number	Detection Criterion	Gain	Q_{Pn}		Parameterization	M_L Threshold
			Q_0	η		
1	3 P -90%	NORESS	--	--	Temporal	2.4-2.7
2	3 P -50%	NORESS	--	--	Temporal	2.2-2.5
3	3 (P or Lg)-90%	NORESS	--	--	Temporal	2.1-2.6
4	3 (P or Lg)-50%	NORESS	--	--	Temporal	1.8-2.3
5	3 P -90%	NORESS	325	0.48	Spectral	2.4-2.7
6	3 P -90%	\sqrt{N}	325	0.48	Spectral	2.3-2.7
7	3 P -90%	1.0	325	0.48	Spectral	2.7-3.3
8	3 P -90%	NORESS	487.5	0.48	Spectral	2.3-2.6
9	3 P -90%	NORESS	162.5	0.48	Spectral	2.7-2.9

Simulations 5-9 of Table 4.2 use our spectral parameterization of Pn detectability. Figure 4.7 shows the corresponding Pn detectability curves. Note that these curves include an implicit frequency dependence, since at each distance they represent the detectability of the beam with the maximum SNR. This beam is determined by a combination of the single-channel SNR and the frequency-dependent beam gain. For example, our spectral model predicts the frequency of the maximum SNR on a single-channel to be greater than 8 Hz for distances less than 400-500 km. However, the optimal detectability is predicted to be on the 3-5 Hz beam since the standard NORESS beam set gives gains close to one at high frequency.

Simulation 5 uses our NORESS Pn attenuation model and the beam gains observed at NORESS (e.g., \sqrt{N} between 2-5 Hz, and one for the 4-8 Hz and 8-16 Hz beams). The 90% M_L threshold for detecting three P phases is shown in Figure 4.8. We use the attenuation and source parameters derived from the inversion of NORESS spectra, the average ambient NORESS noise spectrum, and the beam gains observed at NORESS. Note that the result is nearly the same as the simulation normalized by our temporal parameterization of NORESS Pn detectability. This demonstrates the internal consistency of our temporal and spectral parameterizations.

Figure 4.9a plots the 90% M_L thresholds for detecting three P phases for a network of arrays with \sqrt{N} beam gain at all frequencies. Attenuation and source parameters derived from NORESS spectra and the average NORESS noise spectrum were used to calculate detectability. For the network of arrays, we assume the same sub-arrays are used in beamforming as those listed for the standard NORESS beams in Table 3.1 (e.g., nine elements are used for the two highest-frequency beams and up to 22 elements are used for the lower frequency beams). We find that the optimal detectability is on the 8-16 Hz beam to a distance of 3° and on the 4-8 Hz beam from 3° to 12°. The 90% M_L threshold is between 2.3 and 2.7 for events in the Soviet Union. Therefore, by optimizing beam gain at high-frequency, it is possible to reduce the M_L

Regional Pn D(Δ)

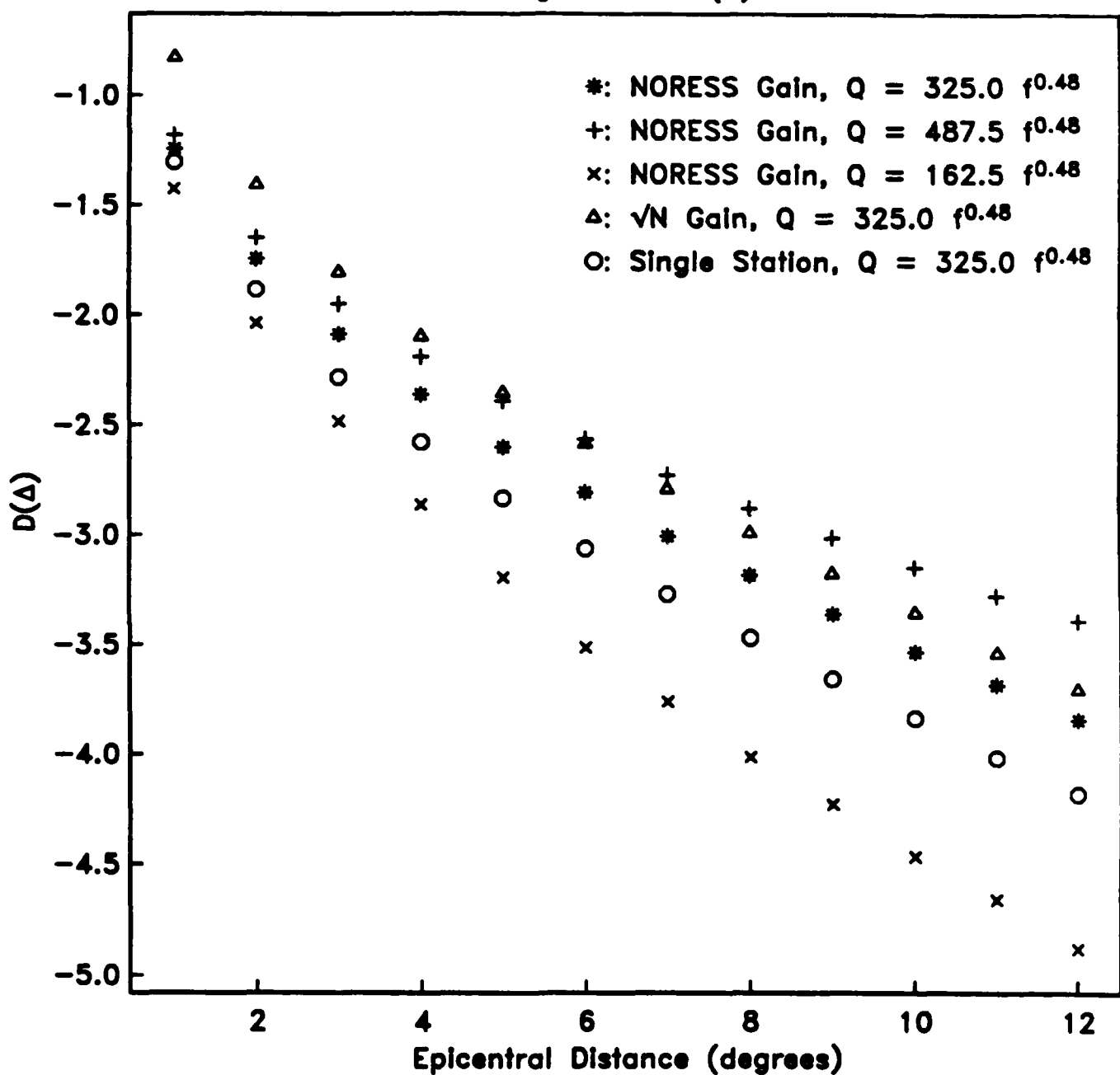
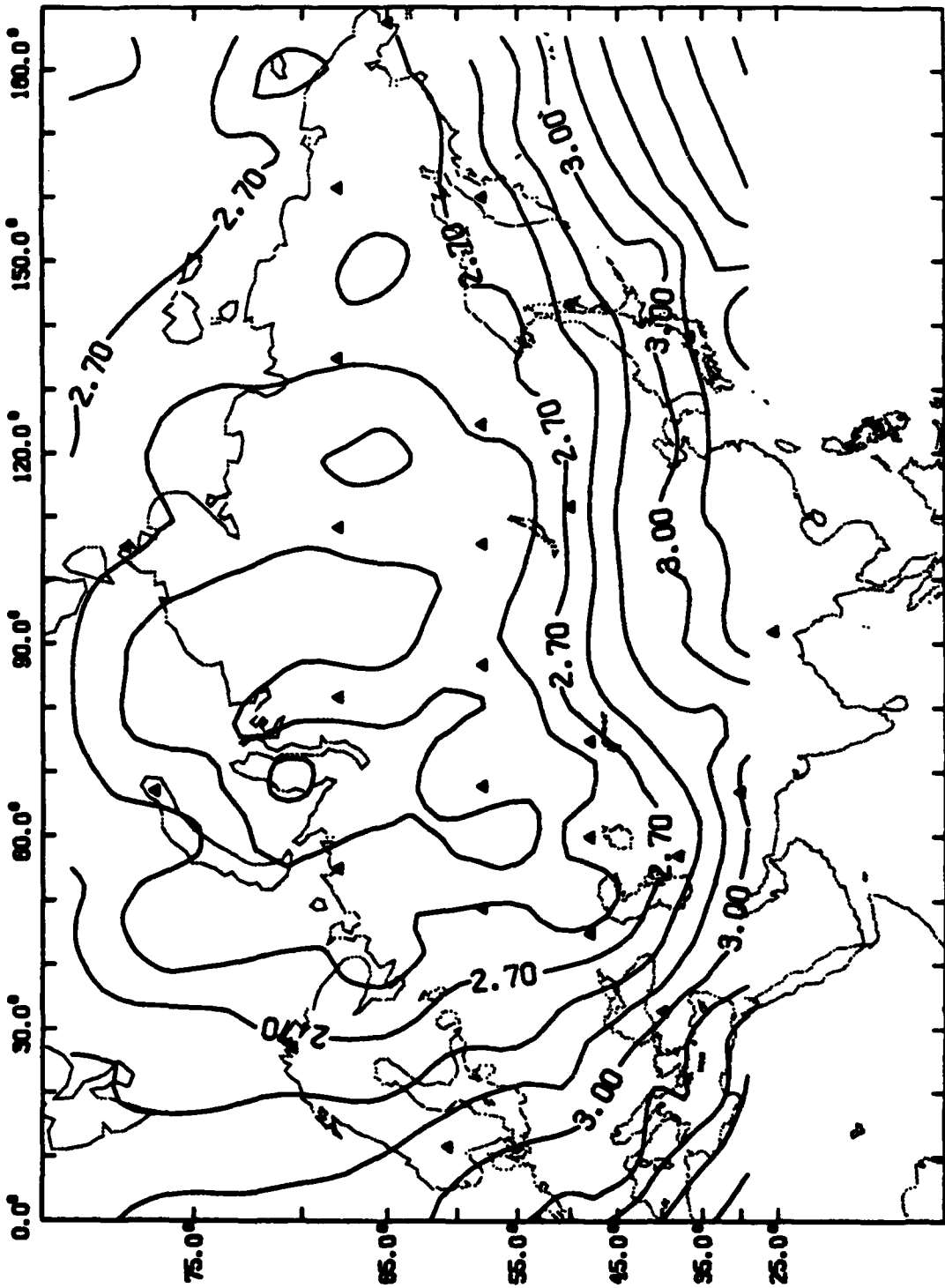


Figure 4.7. Predicted regional P_n detectability curves based on (3.4) and (3.5) with $\alpha = 1.35$ for several assumptions about Q and beam gain. The curves with $Q_{P_n} = 325f^{0.48}$ illustrate the dependence of P_n detectability on beam gain (the beam gain observed at NORESS for the standard beam set is \sqrt{N} between 2-5 Hz and one for the two higher frequency beams). The dependence of P_n detectability on Q is demonstrated by the curves with closed symbols.



CONTOUR FROM 2.4000 TO 3.6000 CONTOUR INTERVAL OF 0.10000

Figure 4.8. Contours of the 90% M_L threshold for detecting 3 P_n phases for a network of NORESS-type arrays; 13 external to the Soviet Union and 20 internal. It is assumed that attenuation, noise, and array performance are all identical to that observed at NORESS. The normalization is based on our spectral parameterization of P_n detectability.

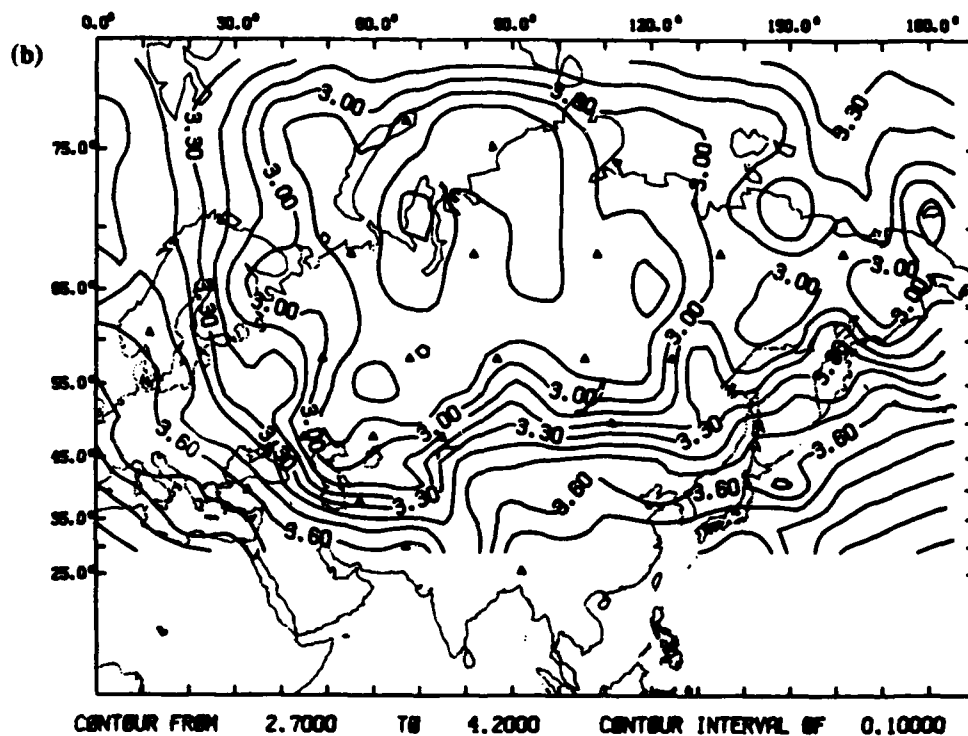
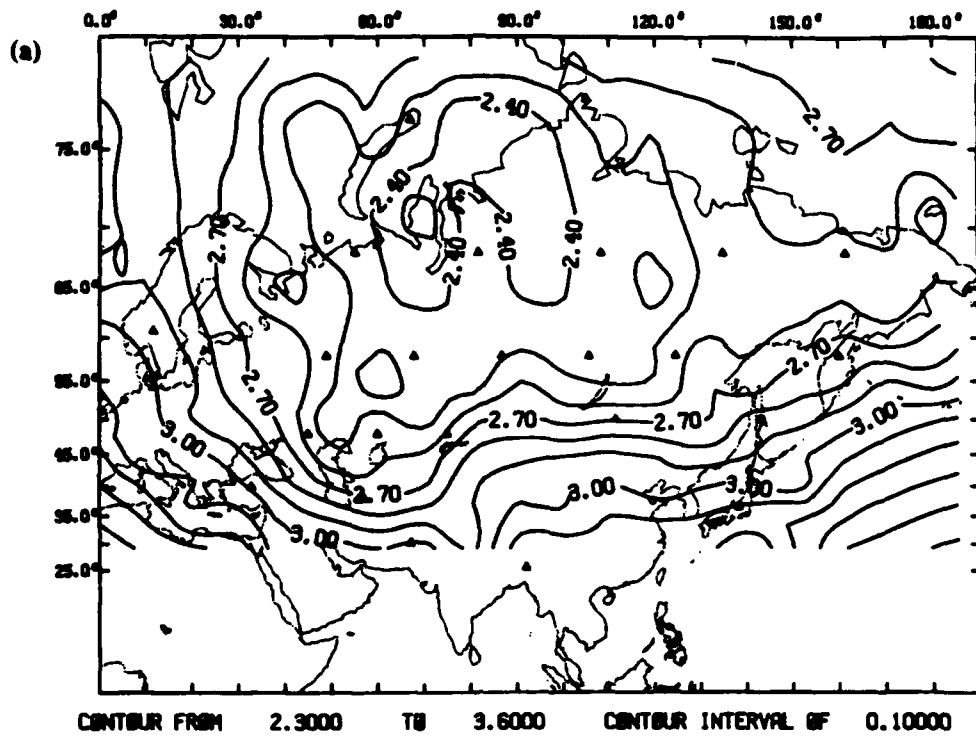


Figure 4.9. Contours of the 90% M_L threshold for detecting 3 P_n phases for a network of (a) NORESS-type arrays with \sqrt{N} beam gain at all frequencies and (b) single-stations. It is assumed that attenuation and noise are identical to that observed at NORESS. The normalization is based on our spectral parameterization of P_n detectability.

detection threshold by about 0.1 throughout most of the Soviet Union. For comparison, Figure 4.9b plots the 90% M_L threshold for a network composed of single stations. To simulate the detection capability of single stations, we simply set the beam gain to one for all frequencies. The P_n detectability is lower than that for the array network by about 0.5 at all distances (Figure 4.7). However, since log moment increases at a rate of $1.35M_L$, the difference in the M_L threshold is slightly less than this. The 90% M_L threshold for the network of single stations is about 2.7 to 3.3 for events in the Soviet Union.

Our final examples are simulations of the detection capability in the Soviet Union of a network of NORESS-type arrays with Q_{P_n} 50% higher and lower than we estimate Scandinavia. The 90% M_L thresholds for detecting three P_n phases are shown in Figure 4.10. We use the average NORESS noise spectrum and the beam gains observed for the standard NORESS beam set. The 90% M_L threshold if Q is 50% higher than at NORESS is between 2.3 to 2.6 for events in the Soviet Union. If Q is 50% lower, the threshold is between 2.7 and 2.9. That is, the threshold changes by about 0.4 over this range of Q .

The accuracy of our simulations of the detection capability of hypothetical networks in the Soviet Union is governed by the accuracy of our estimates of attenuation and noise in that region. We are confident that we have accurately represented the detection capability of the NORESS array, however it is not possible to assess the accuracy of our estimates for the Soviet Union without examining data collected in that region.

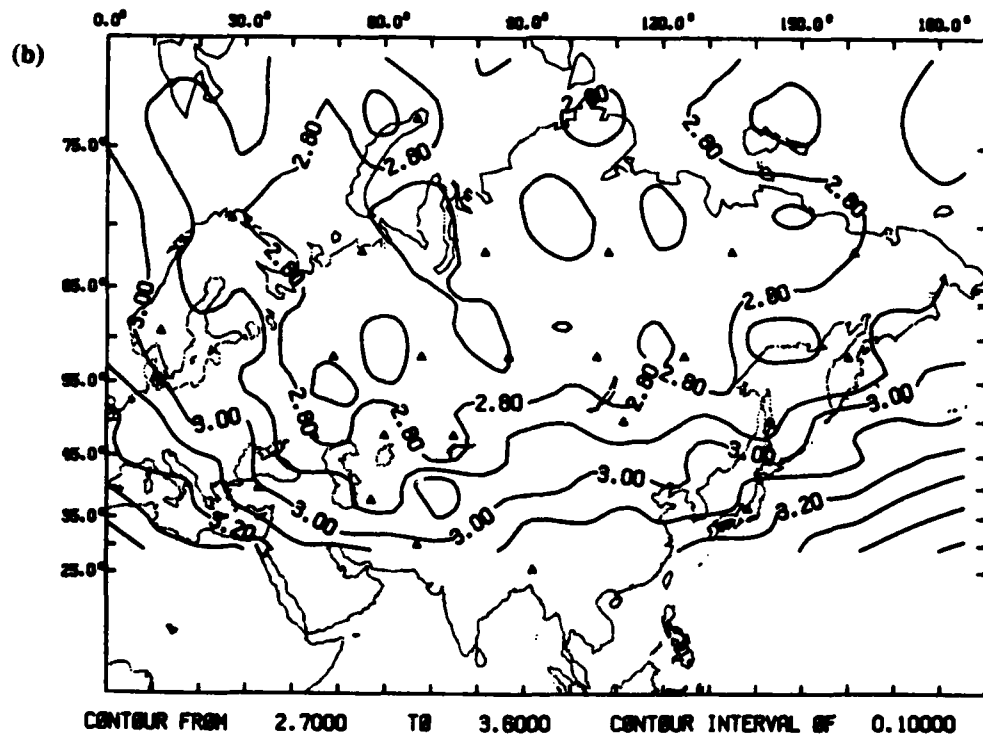
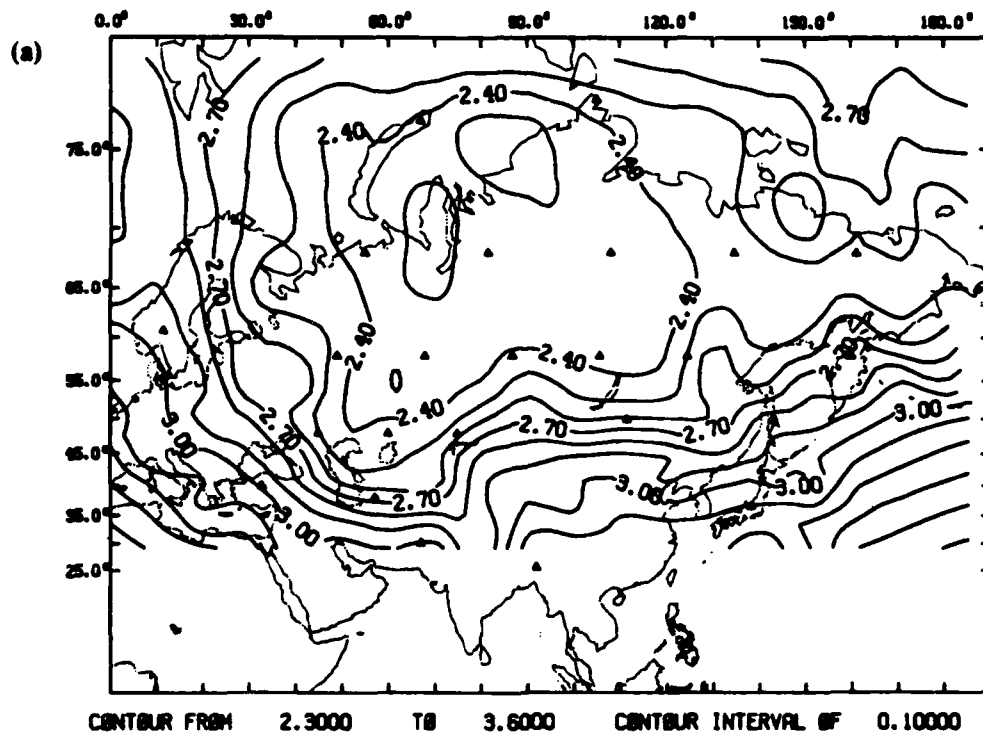


Figure 4.10. Contours of the 90% M_L threshold for detecting 3 P_n phases for a network of NORESS-type arrays assuming that Q_{P_n} is (a) 50% higher and (b) 50% lower than our NORESS estimate. It is assumed that array performance is identical to that observed at NORESS. The normalization is based on our spectral parameterization of P_n detectability.

5. CONCLUSIONS

The main objective of this study is to evaluate detection capability of a hypothetical network of seismic stations/arrays in and around the Soviet Union. We use a parameterization of regional wave spectra recorded at NORESS as a basis for normalizing simulations of network capability. Since accurate attenuation and noise estimates are not available for the Soviet Union, we also determine the sensitivity of our results to our assumptions about the frequency-dependent signal and noise characteristics in the USSR.

Our approach involves four steps. First, we parameterize NORESS spectra in terms of Q and seismic moment. Next, we determine the relationship between the single-channel spectral amplitudes and the temporal amplitudes used in signal detection at NORESS. Third, we predict the detection capability of the NORESS array based on our spectral parameterization and validate our results by comparing to observed detection statistics and to the results of an empirical study of detection capability in this region. Finally, we extrapolate our results for NORESS to simulate the detection capability of a hypothetical network of seismic stations in and around the Soviet Union.

From our parameterization of NORESS spectra, we conclude:

- The attenuation of Pn spectra at NORESS between 1-15 Hz is consistent with $r^{-1.3}$ geometric spreading and $Q(f) = 325f^{0.48}$.
- The attenuation of Lg spectra at NORESS between 1-7 Hz (computed for the fixed group velocity window, 3.6–3.0 km/s) is consistent with cylindrical spreading beyond a transition distance of 100 km, and $Q(f) = 560f^{0.26}$.

These results were obtained by inverting spectra for 186 regional events with M_L between 1.1 and 4.8. The inversion produced a range of attenuation models consistent with the observations. To resolve parameter trade-offs we impose the constraint that the separate Pn and Lg inversions define an internally consistent set of source parameters. This is the basis for selecting our "preferred" model. However, all the models give similar predictions for detection capability for the distance and frequency range of the NORESS data. Our model of Pn attenuation at NORESS implies the following conclusion about network detection capability:

- If the upper mantle structure of the Russian platform is at all similar to Scandinavia, high frequencies (>20 Hz) are expected to contribute very little to network detection capability, except at distances less than about 400-500 km. At these distances, the detection thresholds are quite low in lower frequency bands (about 2.1 for Pn detection and 1.8 for detection of either Pn or Lg at NORESS). Therefore, our results for NORESS are inconsistent with the major conclusion of *Evernden et al.* [1986]; that detection capability for events in the USSR would be enhanced at frequencies greater than 20 Hz.

To use our parameterization of regional P_n spectra to predict and extrapolate NORESS detection capability, we determine the relationship between the single-channel spectral amplitudes and the time domain amplitudes used in signal detection. Our main results are:

- The P_n SNR used in signal detection at NORESS can be expressed as a product of the single-channel spectral SNR and terms specific to the NORESS array configuration and beamforming. This factorization allows us to predict P_n detectability for other regions, or for other station configurations.
- Due to dispersion and the non-stationarity of the pre- L_g noise, a similar relationship could not be found for L_g . Therefore, we simply determine an empirical relationship for the L_g detectability at NORESS and note that our results cannot be extrapolated with confidence to regions with different attenuation.

From our parameterization of P_n spectra, and the relationship between temporal and spectral amplitudes, we estimate the detection capability of the NORESS array. We also estimate P_n and L_g detectability at NORESS based on a simple parameterization of observed temporal amplitudes. We conclude the following for the detection capability at NORESS:

- The 50% and 90% M_L thresholds for detecting P_n , based on our parameterization of NORESS spectra, are 1.6 and 2.0 at 400 km and 2.5 and 2.8 at 1000 km.
- Based on our parameterization of observed temporal amplitudes, the 50% and 90% M_L thresholds for detecting P_n are 1.6 and 2.0 at 400 km and 2.4 and 2.8 at 1000 km. These are consistent with the estimates obtained from our spectral parameterization. Our estimates of the 50% and 90% M_L thresholds for detecting either P_n or L_g at 1000 km are 2.2 and 2.6. Thus, including L_g in the detection criterion reduces the magnitude threshold by about 0.2 at 1000 km.
- Our results for NORESS detection capability are consistent with those of Ringdal [1986], who compared detections at NORESS with bulletins produced by local seismic networks. His estimates of the 50% and 90% M_L thresholds between 700-1400 km are 2.3 and 2.7 for P_n detection and 1.9 and 2.5 for either P_n or secondary phase detection.

We are confident that we have accurately estimated the detection capability of the NORESS array. However, these estimates are based on the standard beam set used to process NORESS data. For this set, we found that close to \sqrt{N} beam gain (where N is the number of elements used in beamforming) is achieved between 2-5 Hz, but that the gain at high frequency (8-16 Hz) is close to one. It is possible that the beam gain could be improved at high frequency by simply adding steered beams [T. Kvaerna, personal communication, 1988]. If this is the case, our results may underestimate the detection capability of the NORESS array with an optimal

beam deployment. Of course, this is only relevant for distances less than about 500 km, since at longer ranges the single-channel SNR is maximum at lower frequency.

The final results of this study are simulations of the detection capability of a hypothetical network in the Soviet Union. The network consists of 13 stations external to the USSR and 20 internal stations. The spacing of the internal stations is about 1000 km. We did not simulate the capability of sparse networks due to greater uncertainty in the normalization at teleseismic distances. We conclude the following:

- First, we assume that the frequency-dependent signal and noise characteristics in the Soviet Union are identical to those we observe at NORESS, and that the monitoring network consists of NORESS-type arrays equipped with the standard beam set used to process NORESS data (beam gain equal to \sqrt{N} between 2-5 Hz, and one at higher frequency). Based on these assumptions, the 90% M_L threshold for detecting 3 P_n phases for events in the Soviet Union is between 2.4 and 2.7. Including L_g in the detection criterion reduces the M_L threshold by 0.2–0.3.
- To determine the extent to which our results depend on the array performance observed at NORESS, we assume that the frequency-dependent signal and noise characteristics in the Soviet Union are identical to those at NORESS, but we vary assumptions about beam gain. The 90% M_L threshold for detecting 3 P_n phases for a network of NORESS-type arrays with \sqrt{N} beam gain at all frequencies (*i.e.*, detection of high frequencies better than that currently observed at NORESS) is between 2.3-2.7. Since the enhanced SNR gain at high frequencies is relevant only for distances less than about 500 km, the M_L threshold for events near the periphery of the internal network is insensitive to the high-frequency beam gain.
- The M_L threshold for a network of single stations is between 0.4 and 0.5 higher than that for the network of NORESS-type arrays with \sqrt{N} beam gain at all frequencies. It is 0.3 to 0.5 higher than for a network of arrays with observed NORESS capabilities.
- If Q_{P_n} is 50% higher in the Soviet Union than our estimate for Scandinavia, the 90% M_L threshold for detecting 3 P_n phases for a network of NORESS-type arrays is between 2.3 and 2.6. The 90% M_L threshold is between 2.7 and 2.9 if Q_{P_n} is 50% lower than our estimate for Scandinavia. Very few studies of frequency-dependent P_n attenuation have been conducted, so it is difficult to bound the expected regional variability of Q_{P_n} . The $\pm 50\%$ range was based on comparing our Q_{L_g} to values estimated for the eastern and western United States. While there is no guarantee that this range is representative of the variability of P_n attenuation, the spectral shapes are quite dissimilar and result in very different conclusions about high-frequency detection capability.

The accuracy of these simulations of the detection capability of hypothetical networks depends on the accuracy of our estimates of attenuation and noise in the Soviet Union. Extrapolation of observations from other regions (such as the region around NORESS used in this study) have large uncertainty. To be more confident, we need to study data from stations throughout the Soviet Union to estimate the actual attenuation and noise conditions to be encountered.

ACKNOWLEDGEMENTS

We are grateful to Dale Breeding of the SCARS Project at Sandia National Laboratories for providing us with the NORESS data used in this report. We also thank Thomas Bache, the project manager, for his review of this manuscript, and for his technical contribution throughout the research conducted under this contract. This research was supported through Defense Advanced Research Projects Agency Contract F19628-86-C-0051 (monitored by Air Force Geophysics Laboratory).

REFERENCES

- Aki, K., and P. Richards, *Quantitative Seismology: Theory and Methods*, W. H. Freeman, San Francisco, Calif., 1980.
- Abramowitz, M., and I. Segun, *Handbook of Mathematical Functions*, U.S. National Bureau of Standards, Washington, D. C., 1964.
- Bache, T., P. Marshall, and L. Bache, Q for teleseismic P waves from central Asia, *J. Geophys. Res.*, 90, 3575-3587, 1985.
- Baumgardt, D., and K. Ziegler, Spectral evidence for source multiplicity in explosions, ENSCO, Inc. *Semi-Annual Technical Report SAS-TR-87-01*, AFGL-TR-87-0045, ADA187363, January 1987.
- Bennett, T., J. Murphy, H. Shah, and B. Barker, Theoretical analysis of regional phase behavior, *Tech. Rep. SSS-R-87-8113*, Sys., Sci. and Software, La Jolla, Calif., 1987.
- Berger, J., H. Eissler, F. Vernon, I. Nersesov, M. Gokhberg, O. Stolyrov, and N. Tarasov, Studies of high-frequency seismic noise in Eastern Kazakhstan, *Bull. Seism. Soc. Am.*, [submitted], 1988.
- Bratt, S., T. Sereno, and T. Bache, Seismic monitoring of a low threshold Test Ban Treaty in the USSR, *EOS*, 68, 1364, 1987.
- Bungum, H., S. Vaage, and E. Husebye, The Meløy earthquake sequence, northern Norway; Source parameters and their moment scaling relations, *Bull. Seismol. Soc. Am.*, 72, 197-206, 1982.
- Campillo, M., J. Plantet, and M. Bouchon, Frequency-dependent attenuation in the crust beneath central France from L_g waves: Data analysis and numerical modeling, *Bull. Seismol. Soc. Am.*, 75, 1395-1411, 1985.
- Chavez, D., and K. Priestley, Measurement of frequency dependent L_g attenuation in the Great Basin, *Geophys. Res. Lett.*, 13, 551-554, 1986.
- Chun, K.-Y., G. West, R. Kokoski and C. Samson, A novel technique for measuring L_g attenuation—Results from eastern Canada between 1 to 10 Hz, *Bull. Seismol. Soc. Am.*, 77, 398-419, 1987.

- Ciervo, A., S. Sanemitsu, D. Snead, R. Suey, and A. Watson, User's manual for SNAP/D: seismic network assessment program for detection, *Pacific-Sierra Research Corporation, Report 1027B*, 1985.
- Evernden, J., C. Archambeau, and E. Cranswick, An evaluation of seismic decoupling and underground nuclear test monitoring using high-frequency seismic data, *Rev. Geophys.*, 24, 143-215, 1986.
- Fyen, J., NORESS noise spectral studies - beam suppression, *Sci. Rep. 1-86/87*, NTNF/NORSAR, Kjeller, Norway, 1986.
- Goncz, J., W. Dean, Z. Der, A. Lees, K. McLaughlin, T. McElfresh, and M. Marshall, Propagation and excitation of Lg , Sn , and $P-Pn$ waves from eastern United States earthquakes by regression analysis of RSTN data, *Final Tech. Rep. TGAL-86-7*, Teledyne Geotech Alexandria Lab., Alexandria, Va., Contract: MDA903-85-C-0086, 1987.
- Gupta, I., and K. McLaughlin, Attenuation of ground motion in the eastern United States, *Bull. Seismol. Soc. Am.*, 77, 366-383, 1987.
- Hasegawa, H., Attenuation of Lg waves in the Canadian Shield, *Bull. Seismol. Soc. Am.*, 75, 1569-1582, 1985.
- Herrmann, R., and A. Kijko, Modeling some empirical vertical component Lg relations, *Bull. Seismol. Soc. Am.*, 73, 157-171, 1983.
- Kvaerna, T., and S. Mykkeltveit, Optimum beam deployment for NORESS P-wave detection, *Sci. Rep. 1-86/87*, NTNF/NORSAR, Kjeller, Norway, 1986.
- Kvaerna, T., S. Kibsgaard, F. Ringdal, False alarm statistics and threshold determination for regional event detection, *Sci. Rep. 1-87/88*, NTNF/NORSAR, Kjeller, Norway, 1987a.
- Kvaerna, T., S. Kibsgaard, S. Mykkeltveit, F. Ringdal, Towards an optimum beam deployment for NORESS; experiments with a North Sea / western Norway data base, *Sci. Rep. 1-87/88*, NTNF/NORSAR, Kjeller, Norway, 1987b.
- Langston, C., Aspects of Pn and Pg propagation at regional distances, *Bull. Seismol. Soc. Am.*, 72, 457-471, 1982.
- Mueller, C., and E. Cranswick, Source parameters from locally recorded aftershocks of the 9 January 1982 Miramichi, New Brunswick, earthquake, *Bull. Seismol. Soc. Am.*, 75, 337-360, 1985.

- Mueller, R., and J. Murphy, Seismic characteristics of underground nuclear detonations, *Bull. Seismol. Soc. Am.*, 61, 1675-1692, 1971.
- Mykkeltveit, S., A new regional array in Norway: Design work, *Sci. Rep. 2-82/83*, NTN/NORSAR, Kjeller, Norway, 1983.
- Mykkeltveit, S., and H. Bungum, Processing of regional seismic events using data from small-aperture arrays, *Bull. Seismol. Soc. Am.*, 74, 2313-2333, 1984.
- Mykkeltveit, S., D. Harris, and T. Kvaerna, Preliminary evaluation of the event detection and location capability of the small-aperture NORESS array, *Sci. Rep. 2-84/85*, NTN/NORSAR, Kjeller, Norway, 1985.
- Nuttli, O., On the attenuation of *Lg* waves in western and central Asia and their use as a discriminant between earthquakes and explosions, *Bull. Seismol. Soc. Am.*, 71, 249-261, 1981.
- Nuttli, O., Yield estimates of Nevada test site explosions obtained from seismic *Lg* waves, *J. Geophys. Res.*, 91, 2137-2151, 1986.
- Pomeroy, P., Aspects of seismic wave propagation in eastern North America—A preliminary report, Rondout Associates, Inc., Stone Ridge, N. Y., 1977.
- Pomeroy, P., W. Best, and T. McEvelly, Test ban treaty verification with regional data—A review, *Bull. Seismol. Soc. Am.*, 72, S89-S129, 1982.
- Ringdal, F., Real time event detection using the small-aperture NORESS array, *Sci. Rep. 2-84/85*, NTN/NORSAR, Kjeller, Norway, 1985a.
- Ringdal, F., Initial results from NORESS detection processing, *Sci. Rep. 1-85/86*, NTN/NORSAR, Kjeller, Norway, 1985b.
- Ringdal, F., Regional event detection using the NORESS array, *Sci. Rep. 2-85/86*, NTN/NORSAR, Kjeller, Norway, 1986.
- Ringdal, F., B. Hokland, and T. Kvaerna, Initial results from the NORESS high frequency seismic element (HFSE), *Sci. Rep. 2-85/86*, NTN/NORSAR, Kjeller, Norway, 1986.
- Sereno, T., and S. Bratt, Attenuation and detection capability of regional phases recorded at NORESS, *Semi-Annu. Tech. Rep. SAIC 88/1598*, Sci. Appl. Int. Corp., San Diego, Calif., AFGL-TR-88-0095, 1988. ADA196568

- Sereno, T., S. Bratt, and T. Bache, Regional wave attenuation and seismic moment from the inversion of NORESS spectra, *Semi-Annu. Tech. Rep. SAIC 87/1736*, Sci. Appl. Int. Corp., San Diego, Calif., AFGL-TR-87-0237, ADA187399, 1987.
- Sereno, T., S. Bratt, and T. Bache, Simultaneous inversion of regional wave spectra for attenuation and seismic moment in Scandinavia, *J. Geophys. Res.*, *93*, 2019-2035, 1988.
- Singh, S., and R. Herrmann, Regionalization of crustal coda Q in the continental United States, *J. Geophys. Res.*, *88*, 527-538, 1983.
- Stevens, J., and S. Day, The physical basis of m_b - M_s and variable frequency magnitude methods for earthquake/explosion discrimination, *J. Geophys. Res.*, *90*, 3009-3020, 1985.
- Street, R., R. Herrmann, and O. Nuttli, Spectral characteristics of the L_g wave generated by central United States earthquakes, *Geophys. J. R. Astron. Soc.*, *41*, 51-63, 1975.
- Suteau-Henson, A., and T. Bache, Spectral characteristics of regional phases recorded at NORESS, *Bull. Seismol. Soc. Am.*, *78*, 708-725, 1988.
- Veith, K., and G. Clawson, Magnitude from short-period P wave data, *Bull. Seismol. Soc. Am.*, *62*, 435-452, 1972.
- Willis, D., Comparison of seismic waves generated by different types of sources, *Bull. Seismol. Soc. Am.*, *53*, 965-978, 1963.

CONTRACTORS (United States)

Professor Keiiti Aki
Center for Earth Sciences
University of Southern California
University Park
Los Angeles, CA 90089-0741

Professor Charles B. Archambeau
Cooperative Institute for Resch
in Environmental Sciences
University of Colorado
Boulder, CO 80309

Dr. Thomas C. Bache Jr.
Science Applications Int'l Corp.
10210 Campus Point Drive
San Diego, CA 92121 (2 copies)

Dr. Douglas R. Baumgardt
Signal Analysis & Systems Div.
ENSCO, Inc.
5400 Port Royal Road
Springfield, VA 22151-2388

Dr. S. Bratt
Science Applications Int'l Corp.
10210 Campus Point Drive
San Diego, CA 92121

Dr. Lawrence J. Burdick
Woodward-Clyde Consultants
P.O. Box 93245
Pasadena, CA 91109-3245 (2 copies)

Professor Robert W. Clayton
Seismological Laboratory/Div. of
Geological & Planetary Sciences
California Institute of Technology
Pasadena, CA 91125

Dr Karl Coyner
N. E. Research
P.O. Box 857
Norwich, VT 05055

Dr. Vernon F. Cormier
Department of Geology & Geophysics
U-45, Room 207
The University of Connecticut
Storrs, Connecticut 06268

Dr. Zoltan A. Der
ENSCO, Inc.
5400 Port Royal Road
Springfield, VA 22151-2388

Professor John Ferguson
Center for Lithospheric Studies
The University of Texas at Dallas
P.O. Box 830688
Richardson, TX 75083-0688

Professor Stanley Flatte'
Applied Sciences Building
University of California, Santa Cruz
Santa Cruz, CA 95064

Professor Steven Grand
Department of Geology
245 Natural History Building
1301 West Green Street
Urbana, IL 61801

Professor Roy Greenfield
Geosciences Department
403 Deike Building
The Pennsylvania State University
University Park, PA 16802

Professor David G. Harkrider
Seismological Laboratory
Div of Geological & Planetary Sciences
California Institute of Technology
Pasadena, CA 91125

Professor Donald V. Helmberger
Seismological Laboratory
Div of Geological & Planetary Sciences
California Institute of Technology
Pasadena, CA 91125

Professor Eugene Herrin
Institute for the Study of Earth
& Man/Geophysical Laboratory
Southern Methodist University
Dallas, TX 75275

Professor Robert B. Herrmann
Department of Earth & Atmospheric
Sciences
Saint Louis University
Saint Louis, MO 63156

Professor Lane R. Johnson
Seismographic Station
University of California
Berkeley, CA 94720

Professor Thomas H. Jordan
Department of Earth, Atmospheric
and Planetary Sciences

Mass Institute of Technology
Cambridge, MA 02139

Dr Alan Kafka
Department of Geology &
Geophysics
Boston College
Chestnut Hill, MA 02167

Professor Leon Knopoff
University of California
Institute of Geophysics
& Planetary Physics
Los Angeles, CA 90024

Professor Charles A. Langston
Geosciences Department
403 Deike Building
The Pennsylvania State University
University Park, PA 16802

Professor Thorne Lay
Department of Geological Sciences
1006 C.C. Little Building
University of Michigan
Ann Harbor, MI 48109-1063

Dr. Randolph Martin III
New England Research, Inc.
P.O. Box 857
Norwich, VT 05055

Dr. Gary McCartor
Mission Research Corp.
735 State Street
P.O. Drawer 719
Santa Barbara, CA 93102 (2 copies)

Professor Thomas V. McEvelly
Seismographic Station
University of California
Berkeley, CA 94720

Dr. Keith L. McLaughlin
S-CUBED,
A Division of Maxwell Laboratory
P.O. Box 1620
La Jolla, CA 92038-1620

Professor William Menke
Lamont-Doherty Geological Observatory
of Columbia University
Palisades, NY 10964

Professor Brian J. Mitchell
Department of Earth & Atmospheric
Sciences
Saint Louis University
Saint Louis, MO 63156

Mr. Jack Murphy
S-CUBED
A Division of Maxwell Laboratory
11800 Sunrise Valley Drive
Suite 1212
Reston, VA 22091 (2 copies)

Professor J. A. Orcutt
Institute of Geophysics and Planetary
Physics, A-205
Scripps Institute of Oceanography
Univ. of California, San Diego
La Jolla, CA 92093

Professor Keith Priestley
University of Nevada
Mackay School of Mines
Reno, NV 89557

Wilmer Rivers
Teledyne Geotech
314 Montgomery Street
Alexandria, VA 22314

Professor Charles G. Sammis
Center for Earth Sciences
University of Southern California
University Park
Los Angeles, CA 90089-0741

Dr. Jeffrey L. Stevens
S-CUBED,
A Division of Maxwell Laboratory
P.O. Box 1620
La Jolla, CA 92038-1620

Professor Brian Stump
Institute for the Study of Earth & Man
Geophysical Laboratory
Southern Methodist University
Dallas, TX 75275

Professor Ta-liang Teng
Center for Earth Sciences
University of Southern California
University Park
Los Angeles, CA 90089-0741

Professor M. Nafi Toksoz
Earth Resources Lab
Dept of Earth, Atmospheric and
Planetary Sciences
Massachusetts Institute of Technology
42 Carleton Street
Cambridge, MA 02142

Professor Terry C. Wallace
Department of Geosciences
Building #11
University of Arizona
Tucson, AZ 85721

Weidlinger Associates
ATTN: Dr. Gregory Wojcik
4410 El Camino Real, Suite 110
Los Altos, CA 94022

Professor Francis T. Wu
Department of Geological Sciences
State University of New York
At Binghamton
Vestal, NY 13901

GOVERNMENT

Dr. Ralph Alewine III
DARPA/NMRO
1400 Wilson Boulevard
Arlington, VA 22209-2308

Dr. Robert Blandford
DARPA/NMRO
1400 Wilson Boulevard
Arlington, VA 22209-2308

Sandia National Laboratory
ATTN: Dr. H. B. Durham
Albuquerque, NM 87185

Dr. Jack Evernden
USGS-Earthquake Studies
345 Middlefield Road
Menlo Park, CA 94025

U.S. Geological Survey
ATTN: Dr. T. Hanks
Nat'l Earthquake Resch Center
345 Middlefield Road
Menlo Park, CA 94025

Dr. James Hannon
Lawrence Livermore Nat'l Lab.
P.O. Box 808
Livermore, CA 94550

U.S. Arms Control & Disarm. Agency
ATTN: Dick Morrow
Washington, D.C. 20451

Paul Johnson
ESS-4, Mail Stop J979
Los Alamos National Laboratory
Los Alamos, NM 87545

Ms. Ann Kerr
DARPA/NMRO
1400 Wilson Boulevard
Arlington, VA 22209-2308

Dr. Max Koontz
US Dept of Energy/DP 5
Forrestal Building
1000 Independence Ave.
Washington, D.C. 20585

Dr. W. H. K. Lee
USGS
Office of Earthquakes, Volcanoes,
& Engineering
Branch of Seismology
345 Middlefield Rd
Menlo Park, CA 94025

Dr. William Leith
USGS
Mail Stop 928
Reston, VA 22092

Dr. Richard Lewis
Dir. Earthquake Engineering and
Geophysics
U.S. Army Corps of Engineers
Box 631
Vicksburg, MS 39180

Dr. Robert Masse'
Box 25046, Mail Stop 967
Denver Federal Center
Denver, Colorado 80225

R. Morrow
ACDA/VI
Room 5741
320 21st Street N.W.
Washington, D.C. 20451

Dr. Keith K. Nakanishi
Lawrence Livermore National Laboratory
P.O. Box 808, L-205
Livermore, CA 94550 (2 copies)

Dr. Carl Newton
Los Alamos National Lab.
P.O. Box 1663
Mail Stop C335, Group E553
Los Alamos, NM 87545

Dr. Kenneth H. Olsen
Los Alamos Scientific Lab.
Post Office Box 1663
Los Alamos, NM 87545

Howard J. Patton
Lawrence Livermore National Laboratory
P.O. Box 808, L-205
Livermore, CA 94550

Mr. Chris Paine
Office of Senator Kennedy
SR 315
United States Senate
Washington, D.C. 20510

AFOSR/NP
ATTN: Colonel Jerry J. Perrizo
Bldg 410
Bolling AFB, Wash D.C. 20332-6448

HQ AFTAC/TT
Attn: Dr. Frank F. Pilotte
Patrick AFB, Florida 32925-6001

Mr. Jack Rachlin
USGS - Geology, Rm 3 C136
Mail Stop 928 National Center
Reston, VA 22092

Robert Reinke
AFWL/NTEG
Kirtland AFB, NM 87117-6008

HQ AFTAC/TGR
Attn: Dr. George H. Rothe
Patrick AFB, Florida 32925-6001

Donald L. Springer
Lawrence Livermore National Laboratory
P.O. Box 808, L-205
Livermore, CA 94550

Dr. Lawrence Turnbull
OSWR/NED
Central Intelligence Agency
CIA, Room 5G48
Washington, D.C. 20505

Dr. Thomas Weaver
Los Alamos Scientific Laboratory
Los Alamos, NM 97544

AFGL/SULL
Research Library
Hanscom AFB, MA 01731-5000 (2 copies)

Secretary of the Air Force (SAFRD)
Washington, DC 20330
Office of the Secretary Defense
DDR & E
Washington, DC 20330

HQ DNA
ATTN: Technical Library
Washington, DC 20305

Director, Technical Information
DARPA
1400 Wilson Blvd.
Arlington, VA 22209

AFGL/XO
Hanscom AFB, MA 01731-5000

AFGL/LW
Hanscom AFB, MA 01731-5000

DARPA/PM
1400 Wilson Boulevard
Arlington, VA 22209

Defense Technical
Information Center
Cameron Station
Alexandria, VA 22314
(5 copies)

Defense Intelligence Agency
Directorate for Scientific &
Technical Intelligence
Washington, D.C. 20301

Defense Nuclear Agency/SPSS
ATTN: Dr. Michael Shore
6801 Telegraph Road
Alexandria, VA 22310

AFTAC/CA (STINFO)
Patrick AFB, FL 32925-6001

Dr. Gregory van der Vink
Congress of the United States
Office of Technology Assessment
Washington, D.C. 20510

Mr. Alfred Lieberman
ACDA/VI-OA' State Department Building
Room 5726
320 - 21st Street, NW
Washington, D.C. 20451